III-2

Materials Sciences

BL5U

Detwinned Electronic Structure of $Ba_{0.82}K_{0.18}Fe_2As_2$ Observed by ARPES

S. Ideta[1,2], M. Nakajima[3] and K. Tanaka[1,2]

[1]*National Institutes of Natural Science, Institute for Molecular Science, Okazaki, 444-8585, Japan*
[2]*The Graduate University for Advanced Studies (SOKENDAI), Okazaki, 444-8585, Japan*
[3]*Department of Physics, Graduate School of Science, Osaka University, Toyonaka 560-0043, Japan*

Iron-based superconductors have an interesting phase diagram with the antiferromagnetic (AFM) transition and the structural phase transition. Recently, nematicity, defined as broken rotational symmetry [a trigonal(C_4)-to-orthorhombic (C_2) structural transition], has shed light on the understanding of the mechanism on the iron-based superconductivity [1-4]. In hole-doped $BaFe_2As_2$ (Ba122) system, $Ba_{1-x}Na_xFe_2As_2$ and $Ba_{1-x}K_xFe_2As_2$ (K-Ba122) have shown the magnetic order without C_4 symmetry breaking [5, 6] and the moment's direction would be swapped from in-plane to out-of-plane [7]. Besides, the superconductivity is suppressed between the superconductivity and the C_4-magnetic phase. The electronic structure at the C_4 magnetic phase has been unclear yet, and it would give us a great interest to elucidate the mechanism of the hole-doped Ba122.

Here, in order to compare with results obtained from the previous study [8], we have demonstrated a temperature dependent angle-resolved photoemission spectroscopy (ARPES) experiment to elucidate the electronic structure of detwinned underdoped K-Ba122 (x = 0.18) with the orthorhombic (C_2) phase transition below the structural and AFM transition temperatures ($T_{N,S}$ ~ 100 K). In hole-doped Fe-SCs, it has been known that the anisotropic resistivity disappears in contrast with the electron-doped Fe-SCs [9]. However, we have clearly observed the orbital anisotropy corresponding to the two-fold symmetry at the C_2 phase in the hole-doped Fe-SC.

High-quality single crystals of $Ba_{0.82}K_{0.18}Fe_2As_2$ (T_c ~ 10 K) were grown by self-flux technique. ARPES experiments were carried out at BL5U of UVSOR-III Synchrotron using the linearly *s* polarized light of $h\nu$ = 60 eV. Temperature was set at T = 6 K-150 K and clean sample surfaces were obtained for the ARPES measurements by cleaving single crystals *in-situ* in an ultrahigh vacuum better than 1×10^{-8} Pa.

Figures 1(a) and 1(b) show the second-derivative ARPES intensity plots along the Z-X and Z-Y directions, respectively, corresponding to the Z points. In Figs. 1(a) and 1(b), the direction of the uniaxial pressure is perpendicular or parallel to the *s* polarization vector respectively [4] as shown by photos, and both band dispersions are considered to be the electronic structure from the strain free single domain. In Fig.1(c), we also measured twinned single crystals and found that two dispersions simultaneously corresponding to the d_{xz} and d_{yz} orbitals shown in Figs. 1(a) and 1(b), respectively. In future work, we focus on the d_{yz} and d_{xz} orbitals as shown in Figs. 1(a) and 1(b) and will analyze the temperature dependent ARPES spectra and compare with the previous ARPES study [8]. In the electronic structure of the Z-X and Z-Y directions, we expect that the occupation of the d_{yz} and d_{xz} orbitals might be the same above $T_{s,N}$.

In summary, we have performed an ARPES study of detwinned K-Ba122 (x = 0.18) and measured the electronic structure in the Z-X, Z-Y, and Z-X/Y directions. We found that the electronic structure in the Z-X and Z-Y directions shows different band dispersions, reflecting the electronic structure from the single domain due to the uniaxial pressure. We will analyze the detailed temperature dependence of the ARPES spectrum of d_{yz} and d_{xz}.

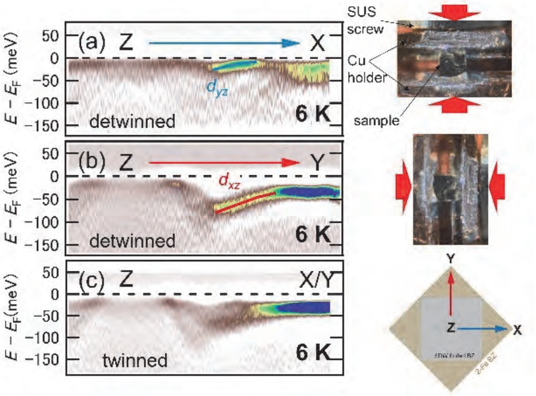

Fig. 1. Electronic structure of underdoped K-doped Ba122. (a), (b), (c) Second-derivative ARPES intensity plots for detwinned (Z-X and Z-Y directions) and twinned $Ba_{0.82}K_{0.18}Fe_2As_2$ taken at $h\nu$ = 60 eV. The d_{yz} and d_{xz} bands are clearly observed differently. Photos of the sample setup and schematic Brillouin Zone are shown on the right side. Red arrows indicate the direction of uniaxial pressure.

[1] R. M. Fernandes *et al.*, Nat. Phys. **10** (2014) 97.
[2] R. M. Fernandes *et al.*, Phys. Rev. Lett. **111** (2013) 127001.
[3] T. Shimojima *et al.*, Phys. Rev. B **90** (2014) 12111(R).
[4] Y. Ming *et al.*, PNAS **108** (2011) 6878.
[5] L. Wang *et al.*, Phys. Rev. B **93** (2016) 014514.
[6] A. E. Böhmer *et al.*, Nat. Commun. **6** (2015) 7911.
[7] D. D. Khalyavin *et al.*, Phys. Rev. B **90** (2014) 174511.
[8] S. Ideta *et al.*, Activity Report **45** (2017) 77.
[9] E.C. Blomberg *et al.*, Nat. Commun. **4** (2014) 1914.

BL1U

Photon Induced Positron Annihilation Lifetime Spectra of Ce:GAGG Crystals Measured Using Ultrashort Laser-Compton-Scattered Gamma Ray Pulses

K. Fujimori[1], M. Kitaura[1], Y. Taira[2], M. Fujimoto[3], Y. Okano[4], H. Zen[5], M. Katoh[3,8],
M. Hosaka[6], J. Yamazaki[3], K. Kamada[7] and A. Ohnishi[1]
[1]*Faculty of Science, Yamagata University, Yamagata 990-8560, Japan*
[2]*National Institute of Advanced Industrial Science and Technology, Tsukuba 305-8568, Japan*
[3]*UVSOR Synchrotron Facility, Institute for Molecular Science, Okazaki 444-8585, Japan*
[4]*Center for Mesoscopic Sciences, Institute for Molecular Science, Okazaki 444-8585, Japan*
[5]*Institute of Advanced Energy, Kyoto University, Uji 611-0011, Japan*
[6]*Synchrotron radiation Research Center, Nagoya University, Nagoya 464-8603, Japan*
[7]*New Industry Creation Hatchery Center, Tohoku University, Sendai 980-8579, Japan*
[8]*Hiroshima Synchrotron Radiation Center, Hiroshima University, Higashi-hiroshima, 739-0046, Japan*

Ce^{3+}-doped $Gd_3Al_2Ga_3O_{12}$ (Ce:GAGG) is known as an inorganic scintillator with high light yield and good energy resolution. It has been demonstrated that, in this material, antisite Gd^{2+} ions adjacent to oxygen vacancies are responsible for shallow electron traps [1]. Such electron traps cause the occurrence of phosphorescence with long lifetime and the lowering of light yield, and thus they have to be suppressed in the process of crystal growth. It was pointed out that the antisite Gd^{3+} ions and oxygen vacancies are introduced in Al/Ga defficient compositions. In order to improve scintillation properties of Ce:GAGG crystals, it is important to find out the best way to suppress Al/Ga deficiency.

The existence of cation vacancies has been investigated by positron annihilation lifetime spectroscopy, because positrons are attractive for negative charged cation vacancies. The position annihilation lifetime spectroscopy (PALS) generally requires radioisotope such as ^{22}Na as a positron source. In this case, positrons are injected from the outside of a crystal, so that pair annihilation gamma rays generate not only from the inside of the crystal but also from the outside. The latter has to be removed to analyze the positron annihilation lifetime at the cation vacancy site, because it is responsible for the uncertainty of the lifetime. This problem is to be solved to perform the lifetime analysis more accurately.

Photon induced PALS (PIPALS) is the only solution that can solve the above-mentioned problem [2]. This method utilizes ultrafast laser Compton-scattered (LCS) gamma ray pulses generated by the normal collision of electron beam and ultrashort laser pulses. The advantage is that positrons can be created inside the crystal through the pair creation process. PIPALS allows us to clarify the existence of cation vacancies in Ce:GAGG crystals. For this purpose, we performed PIPALS experiment using ultrashort LCS gamma ray pulses at the BL1U beamline of UVSOR synchrotron facility.

The size of the Ce:GAGG crystal used in our experiment was 10×10×10 mm^3. The details of PIPALS experiment have been reported elsewhere. The photon energy, pulse width, and repetition rate of the LCS gamma ray pulses were 6.6 MeV, 2 ps, and 1 kHz, respectively. The pair annihilation gamma ray from the Ce:GAGG crystal was detected with two photomultiplier tubes attached BaF_2 crystals, which were faced each other. The waveforms were stored in the memory of a digital storage oscilloscope, when the output signals from two photomultiplier tubes coincided with each other. The PIPALS spectrum of a Ce:GAGG crystal was obtained from the distribution of the time half the maximum intensity.

The PIPALS spectrum of a Ce:GAGG crystal is shown in Fig. 1. Solid circles indicate experimental data. Apparently, the PIPALS spectrum is of a single decay component. A solid line indicates the result of curve fitting analysis, and it reproduces the experimental data. From the fit, the lifetime is determined 178 ± 14 ps. This value is almost agreement with the lifetime of the pair annihilation of a positron with an electron in the bulk. A longer lifetime component is slightly observed in the tailof the main component. The higher statistical accuracy for experimental data is needed for detail lifetime analysis.

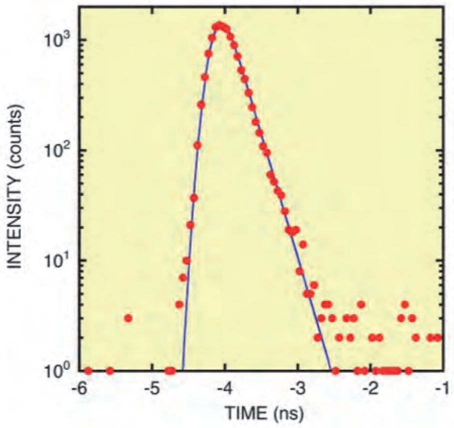

Fig. 1. PIPALS spectrum of a Ce:GAGG crystal measured at room temperature.

[1] M. Kitaura *et al.*, Appl. Phys. Lett. **113** (2018) 041906.

[2] Y. Taira *et al.*, Rev. Sci. Instrum. **84** (2013) 053305.

BL1B

Polarized Terahertz Reflectivity Spectra of $Ca_3TaGa_3Si_2O_{14}$ Piezoelectric Crystals with Ordered Langasite Structure

M. Kitaura[1], K, Kamada[2], Y. Yokota[2], Y. Ohashi[2], S. Watanabe[3] and A. Ohnishi[1]
[1]*Faculty of Science, Yamagata University, Yamagata 990-8560, Japan*
[2]*New Industry Creation Hatchery Center, Tohoku University, Sendai 444-8585, Japan*
[3]*Graduate School of Engineering, Nagoya University, Nagoya 464-8603, Japan*

Langasites are expressed by the chemical formula of $A_3BC_3D_2O_{14}$, and are composed of four cations A-D. These materials belong to the trigonal system of the space group P321, and are known piezoelectric materials with high electromechanical coupling factors. They are classified into two categories: order-type and disorder-type. In order-type langasites, each cation site is occupied by different element. In disorder-type, one element occupies multi cation sites. Order-type langasites are preferred, because they present better thermal stability of piezoelectric properties. $Ca_3TaGa_3Si_2O_{14}$ (CTGS) is one of such order-type langasites. CTGS exhibits a higher electrical resistivity which is advantage to high-temperature use of sensor applications [1]. Despite such an industrial key material, the fundamental optical functions such as dielectric constant and refractive index in the terahertz region have not yet been studied so far. In order to determine terahertz optical functions of CTGS, we have measured polarized terahertz reflectivity spectra of CTGS crystals at 9 K.

A typical result is shown in Fig. 1 by using dotted curves. One can see remarkable dichroism between the spectra for *E*⊥*c* and E//c configurations, which reflects the crystal structure of CTGS. According to the consideration based on group theory [2], the E and A_2 modes are IR-active for *E*⊥*c* and E//c configurations, respectively. Thus, it is likely that the two bands are assigned to E and A_2 modes for *E*⊥*c* and E//c configurations, respectively.

We determined the complex dielectric function from the fit of Eq. (1) with experiment data.

$$\hat{\epsilon} = \epsilon_\infty \frac{\omega_{\rm LO}^2 - \omega^2 - i\omega\gamma_{\rm LO}}{\omega_{\rm TO}^2 - \omega^2 - i\omega\gamma_{\rm TO}}, \qquad (1)$$

where ε_∞ is the high-frequency dielectric constant, ω is the frequency of terahertz wave, and ω_{TO}(ω_{LO}) and γ_{TO}(γ_{LO}) are frequencies and damping factors of TO (LO) phonons, respectively. The parameters determined from the fit of Eq. (1) are listed in Table 1. The reflectivity spectra calculated using the complex dielectric function are indicated by broken curves. In Fig. 1, the calculated reflectivity spectra reproduce the experimental ones. The lowest frequency bands exhibit the high-reflectivity plateau in the high frequency side of ω_{TO} and the dip at the position of ω_{LO}. These features imply that phonon polaritons are formed in CTGS. The phonon polariton dispersion curves obtained are drawn in Fig. 2.

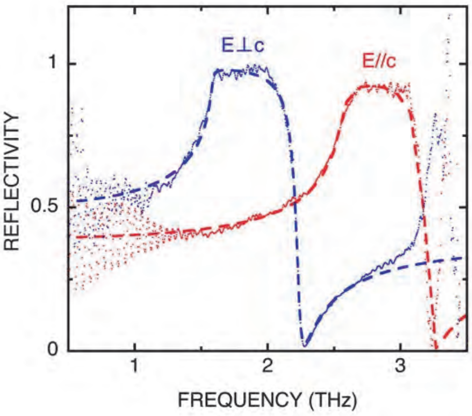

Fig. 1. Polarized terahertz reflectivity spectra of CTGS for *E*⊥*c* and *E*//*c* configurations, measured at 9K. Dotted and broken curves indicate experimental and calculated results, respectively.

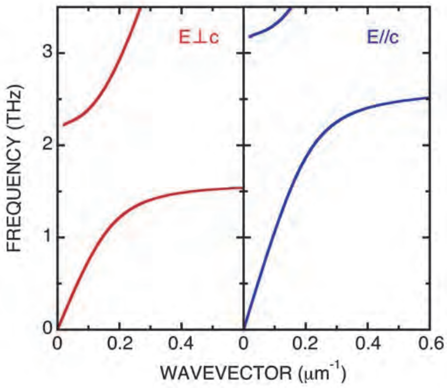

Fig. 2. Phonon polariton dispersion curves of CTGS for *E*⊥*c* and *E*//*c* configurations, calculated on the basis of Fig. 1.

Table1: Parameters obtained from the fit of Eq. (1) with experimental data.

	ε_∞	ω_{TO} (THz)	γ_{TO} (MHz)	ω_{LO} (THz)	γ_{LO} (MHz)
E⊥*c*	16.3	1.58	15.5	2.32	53.9
E//*c*	9.6	2.57	68.6	3.34	26.9

[1] X. Fu *et al*., J. Ceram. Soc. Jpn. **124** (2016) 523.
[2] J. Lan *et al*., Phys. Stat. Sol. **242** (2005) 1996.

BL1B, BL7B

Extremely Sharp Structure of the Vibration Modes Derived from Hydrogen Bonds of Single-crystalline L-alanine

Z. Mita[1], H. Watanabe[1,2] and S. Kimura[1,2]
[1]Graduate School of Frontier Biosciences, Osaka University, Suita 565-0871, Japan
[2]Department of Physics, Graduate School of Science, Osaka University, Toyonaka 560-0043, Japan

Amino acids are the most basic molecules, which compose proteins in vivo. Since almost all amino acids have chiral molecule structure, the crystal structures as well as the optical properties are expected to be anisotropic. One of amino acids with optical isomers, alanine [$CH_3CH(COOH)NH_2$] has orthorhombic molecular structure [1]. Many spectroscopic measurements have been performed for alanine so far [2,3,4]. To clarify the thermal effect of molecular vibrations of different origins, we have measured polarization and temperature dependences of optical conductivity spectra using single crystalline alanine.

We have grown the single crystalline L-alanine by using the solvent evaporation method and confirmed to be orthorhombic structure by taking X-ray Laue diffraction pattern. Anisotropic optical reflectivity spectra from the terahertz (THz) to vacuum-ultraviolet (VUV) regions have been measured by using BL1B and BL7B of UVSOR-III and laboratorial equipments. The obtained spectra were converted to optical conductivity [$\sigma(\omega)$] spectra by the Kramers-Kronig analysis. Temperature dependence of anisotropic $\sigma(\omega)$ spectrum in the THz region is shown in Fig. 1. To reveal its temperature dependence, each peak was fitted with the function of the Lorentz model [5]. As shown in Fig. 1, there are 18 peaks originating from molecular vibrations. The spectra are strong anisotropy and all peaks have very large temperature dependence. Specifically, the peak positions shift to the high energy side and the widths become narrow significantly with decreasing temperature. However, the peak areas of all peaks were approximately constant. In comparison of the obtained peak energy with a previous investigation [2], peaks of number 1 to 12 originate from the vibration of hydrogen bond. Figure 2 shows the peak widths of all peaks as a function of peak energy at 10 K. Red (blue) bars indicate the vibration with (without) the contribution of hydrogen bond. The peaks originating from hydrogen bond have extremely sharp structure, so hydrogen bond is a vibration where thermal fluctuation effects mainly appear. Therefore, to compare the peak width with one another at a very low temperature may become one of useful methods to identify the origin of the peaks, hydrogen bonds or not. In addition, at 10 K, the peak widths originating from hydrogen bonds become almost constant near the resolution limit of the spectrometer, suggesting the possibility of the quantum fluctuations.

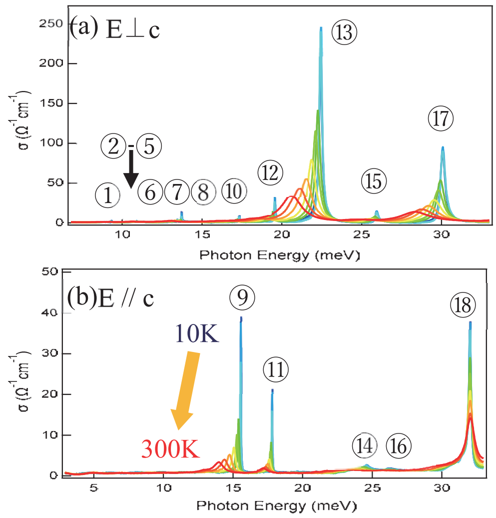

Fig. 1. Anisotropic optical conductivity [$\sigma(\omega)$] spectra at temperatures from 10 to 300 K in the THz region perpendicular to the c-axis (a) and parallel to the c-axis (b).

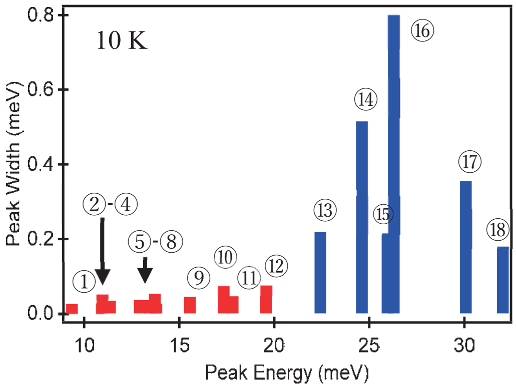

Fig. 2. Peak widths of all peaks in Fig. 1 at 10 K in THz region. Red (blue) bars show the vibrations with (without) the contribution of hydrogen bonds.

[1] M. Fleck and A. M. Petrosyan, Salts of Amino Acids-Crystallization Structure and Properties (Springer, 2014) p.26.
[2] J. Bandekar *et al.,* Spectrochimica Acta Part A: Molecular Spectroscopy **39** (1983) 357.
[3] M. Yamaguchi *et al.,* Appl. Phys. Lett. **86** (2005) 053903.
[4] V. S. Minkov *et al.,* J. Struct. Chem. **51** (2010) 1052.
[5] F. Wooten, Optical Properties of Solids **82** (Academic Press, 1972) 42.

BL1B

Ground State of Ultrashallow Thermal Donors in Silicon

A. Hara and T. Awano
Faculty of Engineering, Tohoku Gakuin University, Tagajo 985-8537, Japan

We discovered ultrashallow thermal donors (USTDs) in carbon- and hydrogen-doped Czochralski silicon (CZ Si) crystals [1, 2]. To the best of our knowledge, these are the shallowest energy levels among those of currently reported donors in Si crystals. In addition, the ground (1S) state of USTDs was found to be split into two states [3, 4]. This is direct evidence that the ground state of USTDs consists of a linear combination of the wave functions of the conduction band minimum. However, electron spin resonance measurements have shown nearly isotropic spectra with slight anisotropy, thus indicating T_d symmetry. If T_d symmetry is correct, the ground state must split into three levels [5, 6]. To evaluate another ground state, we measured the optical absorption spectra at a region of low wavenumbers using BL1B.

Carbon-doped CZ Si samples were doped with hydrogen by annealing in wet oxygen at 1300 °C for 60 min. The samples were then cooled to room temperature by rapid exposure to air. For carbon doping, the Si melt used to prepare the ingot was doped with carbon powder during CZ Si crystal growth. Transmittance spectra were obtained using a BL1B beamline with a flowing cryostat.

Figure 1 shows Trans. (40 K)/Trans. (8 K), where Trans. (T K) represents the transmittance at T K [3, 4]. According to our previous research using BL6B [3, 4], the two broad dips observed at approximately 100 and 150 cm^{-1} at 40 K originate in the transition from the upper ground state to the $2P_0$ and $2P_{+-}$ states. The upper ground states are occupied by thermal excitation of electrons from the ground state.

Figure 2 shows Trans. (40 K)/Trans. (5 K) at a region of 20–100 cm^{-1}. No clear difference was observed between the two transmittance spectra.

These indicate that the ground state of USTDs were split into two levels but not three. Thus, symmetry of USTDs was concluded not to be T_d.

In summary, the ground-state splitting of USTDs was evaluated at a low-wavenumber region. However, new peaks were not observed at 20–100 cm^{-1}. This indicates possibility that the ground state of USTDs are split into two and that symmetry of USTDs is not T_d.

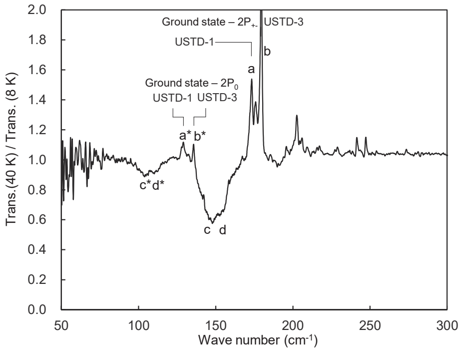

Fig. 1. Trans. (40 K)/Trans. (8 K) of USTDs [4].

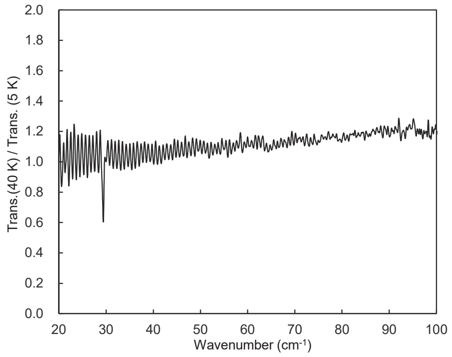

Fig. 2. Trans. (40 K)/Trans. (5 K) of USTDs.

[1] A. Hara, T. Awano, Y. Ohno and I. Yonenaga, Jpn. J. Appl. Phys. **49** (2010) 050203.
[2] A. Hara and T. Awano, Jpn. J. Appl. Phys. **54** (2015) 101302.
[3] A. Hara and T. Awano, Jpn. J. Appl. Phys. **56** (2017) 068001.
[4] A. Hara and T. Awano, Jpn. J. Appl. Phys. **57** (2018) 101301.
[5] W. Kohn, in Solid State Physics, ed. F. Seitz and D. Turnbull (Academic Press, New York, 1957) Vol. **5**, p. 257.
[6] R. L. Aggarwal and A. K. Ramdas, Phys. Rev. **140** (1965) A1246.

BL2A

XAFS Measurement for Alloying Element in Tempered Nitrogen Martensite

M. Sato and T. Murata
Institute for Materials Reseach, Tohoku University, Sendai 980-8522, Japan

It is well known that the martensite phase obtained by rapid quenching is hard but brittle. Therefore the balance between hardness and toughness is adjusted by the subsequent tempering treatment. At that time, cementite is precipitated in case carbon steel, and $Fe_{16}N_2$ or Fe_4N is precipitated in case of nitrogen steel [1, 2].

From the experimental results, the $Fe_{16}N_2$ precipitates in the temperature range between 100 °C and 250 °C, and transition to Fe_4N occurs at tempering temperature around 300 °C. In addition, it has been found that precipitation of alloy nitride also occurs because the substitutional element can be diffused [3].

Although the alloying elements are known to partially dissolve as solid solutions in these precipitates, there is no data of Si and Mo in iron nitrides. The solid solution of alloying elements into iron nitrides greatly affect the stability of iron nitrides and also affect the subsequent precipitation of alloy nitride. Therefore, in order to understand the hardness change associated with tempering, it is important to clarify the solid solution state of such substitutional elements.

In this study, changes in the chemical state of the substitutional elements such as Si and Mo in the precipitates formed during tempering were investigated by XAFS measurement.

Fe-1mass%Si and Fe-1mass%Mo alloys were used as starting materials. They were homogenized at 1523 K for 24h and furnace-cooled until room temperature. The Fe-1Si-0.3N and Fe-1Mo-0.3N alloys were prepared by nitriding and quenching (N-Q) process using NH_3/H_2 mixed gas at 1273 K for 1 h. Then obtained these alloys were tempered at 773 K, and precipitated Fe_4N generated during tempering were extracted using Iodine-alcohol procedure. The Si K-edge and Mo L3-edge XANES spectra were corrected by fluorescence method using InSb double crystal monochrometer and silicon drift detector (SDD) at BL2A in UVSOR, respectively. Obtained data were analyzed using Athena software.

Figure 1 shows Si K-edge XANES spectra of extracted Fe_4N powders. As shown in this figure, pure Si, SiO_2 and Si_3N_4 were used as references.

The obtained XANES spectra are different for each samples, and the extracted residue from the tempered sample at 200 °C had a peak around 1847 eV, while the that obtained from the sample tempered at 500 °C showed double peaks around 1844 eV and 1847 eV, respectively. From the comparison with the reference sample, the peak at 1847 eV is presumed to be due to the oxidation that occurred during extraction or storage. On the other hand, it can be seen that the peak around 1844 eV shows similar shape to Si_3N_4. From the TEM observation, since the precipitation of the Si-nitrides has not been observed in this sample, it is considered that the Si makes a solid solution into Fe_4N and the local structure of Si in Fe_4N has similar to that of Si_3N_4.

Similar results were obtained in the case of Fe-1Mo-0.3N alloy. In the future, detailed examination of solid solution state of alloying element in iron nitrides should be carried out by combination of N K-edge and O K-edge measurement of these samples at BL4B and prediction of XANES spectra from calculation.

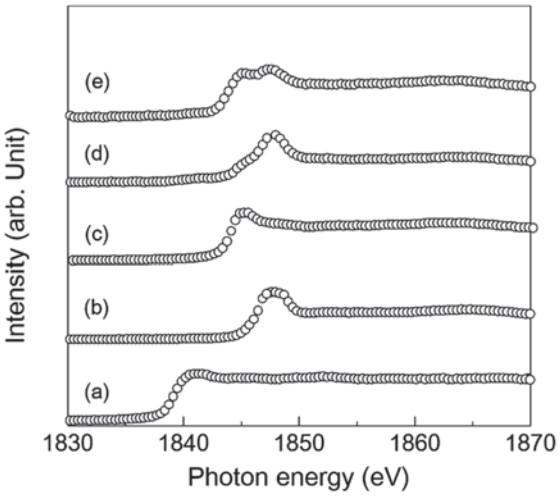

Fig. 1. Si K-edge XANES spectra of references and extracted precipitates. (a) Pure Si, (b) SiO_2, (c) Si_3N_4, (d) extracted residue from tempered sample at 200 °C for 1 h, and (e) extracted residue from tempered sample at 500 °C for 1h.

[1] L. Cheng and E. J. Mittemeijer, Met. Trans. A **21A** (1990) 13.
[2] L. Cheng, A. Bottger and E. J. Mittemeijer, Met. Trans. A **23A** (1992) 1129.

BL2A

Mo L_3-edge XANES Study of Active and Durable Mo-Carbide Species on H-MFI for Methane Dehydroaromatization Catalysts

H. Aritani[1], K. Kuramochi[2], R. Yamazaki[2], H. Miyanaga[1], S. Sato[1] and A. Nakahira[3]
[1]*Graduate School of Engineering, Saitama Institute of Technology, Fukaya 369-0293 Japan*
[2]*Advanced Science Research Laboratory, Saitama Institute of Technology, Fukaya 369-0293 Japan*
[3]*Graduate School of Engineering, Osaka Prefecture University, Sakai 599-8531 Japan*

As an innovative GTL (Gas-To-Liquid) process, methane dehydroaromatization (methane-to-benzene reaction; MTB) has been studied for its potential in the direct conversion of methane into liquid fuels. It has been investigated intensively that Mo-modified H-MFI (Mo/H-MFI) zeolite catalysts show high activity for methane dehydroaromatization. Since the MTB reaction is revolutionary for direct conversion of natural gas, deactivation due to coking over the catalyst cannot be avoided during the methane conversion. It is a serious problem for development of MTB reaction, and thus, clarification of the deactivation process over the catalysts is one of the important point for develop of highly active and durable MTB catalysts. Not only carbon deposition on acid sites of H-MFI but also excess carbonization of active Mo species causes the deactivation of MTB. It is widely accepted that addition of hydrogen to methane reactant is effective for inhibiting the deactivation. In the present study, Mo L_3-edge XANES study is introduced to characterize the active Mo-carbide species on H-MFI after the MTB reaction.

Mo/H-MFI and Mo-V/H-MFI catalysts were prepared by impregnation of H-MFI (Si/Al_2=30-50) support with $MoO_2(acac)_2$–$CHCl_3$ or $MoO_2(acac)_2$–$VO(acac)_2$–$CHCl_3$ solution (5.0wt% as MoO_3; Mo/V=10), and followed by drying overnight and calcination at 773 K. H-MFI supports were synthesized hydrothermally at 413 K for a week, and followed by ion-exchanging with NH_4Cl and calcination at 873 K. The catalytic activity of MTB was evaluated by means of fixed bed flow reaction, as described in a separate paper.[1] The reactant gas is CH_4(20%)+H_2 (0-3%)+He(base) at the flow rate of 30 mL/min, and the reactivity was evaluated at 1023 K by using the 0.25 g of each Mo/H-MFI catalyst. Mo L_{III}-edge XANES spectra were obtained in BL2A of UVSOR-IMS in a total-electron yield mode using InSb double-crystal monochromator. Photon energy was calibrated by using Mo metal-foil at Mo L_{III}-edge, and normalized XANES spectra are presented by using REX-2000 (Rigaku) software.

Figure 1 shows the Mo L_3-edge XANES spectra of Mo/H-MFI and Mo-V/H-MFI catalysts (Si/Al_2=30 and 40) after MTB reaction at 1023 K. For Mo/H-MFI in Si/Al_2=40, partially carbonized Mo species (MoC_xO_y) were possibly formed. By H_2 co-feed, reduction of Mo species advanced. In case of Mo-V/H-MFI (Si/Al_2=40), the Mo species were deeply carbonized and formed MoC_x (x>0.5) species . Since the catalyst showed high MTB reactivity, it is suggested that the deeply carbonized species relate to the highly active one. For Mo/H-MFI (Si/Al_2=30), the Mo species are different from those of Mo/H-MFI in Si/Al_2=40 even in H_2 co-feed and/or V co-modification. Deeply reduced Mo species on H-MFI (Si/Al_2=30) support have been invisible, and α-Mo_2C like species were formed in any cases. Because the Mo/H-MFI (Si/Al_2=30) catalysts showed durable reactivity for MTB, the correlation between the reactivity and the active Mo-carbide species is still unclear. It is now in progress.

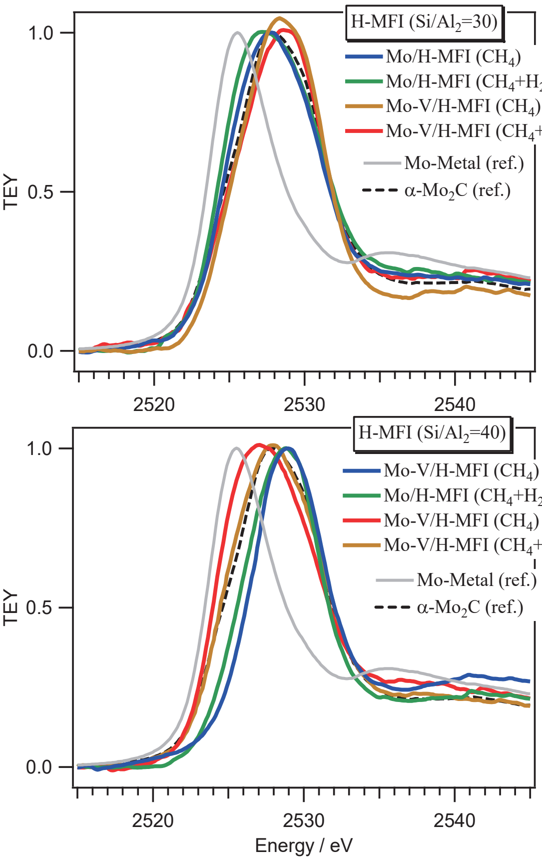

Fig. 1. Mo L_3-edge XANES of Mo/H-MFI and Mo-V/H-MFI catalysts (Si/Al_2=30 and 40) after MTB reaction at 1023 K.

[1] H. Aritani *et al.*, J. Environm. Sci. **21** (2009) 736.
[2] H. Aritani *et al.*, UVSOR Activity Report 2016 **44** (2017) 52.
[3] H. Aritani *et al.*, UVSOR Activity Report 2017 **45** (2018) 44.

BL2A

Local Environment Analysis of Sr Ions in Octacalcium Phosphate

K. Arakawa [1] and T. Yamamoto[1,2,3]
[1]*Faculty of Science and Engineering, Waseda University, Tokyo 169-8555, Japan*
[2]*Insitute of Condensed-Matter Science, Waseda University, Tokyo 169-8555, Japan*
[3]*Kagami Memorial Research Institute for Materials Science and Technology, Waseda University, Tokyo 169-0051, Japan*

Calcium phosphate basis bioceramics have been widely studied because of their efficient medical applications. Among these bioceramics, octacalcium phosphate (OCP) has a great attention, since it is a precursor of the hydroxyapatite (HAp), which can change into the natural bone in human body. It was reported that the existence of the trace elements such as Zn and Mg can enhance the speed of bone reconstruction [1]. However, the mechanism of such enhancement has not yet been understood. To understand the mechanism, it is essential to know the local environment of doped ions. For such purpose, we have studied wide variety of the functional materials by using the X-ray absorption near edge structure (XANES) and the first-principles calculations within a density functional theory (DFT), which could successfully determine the local environment of the trace elements in β-tricalcium phosphate [2-6]. In the current study, local environment of Sr ions in OCP has been investigated by the above strategy, i.e., combined use of XANES measurements and DFT calculations.

Sr-doped OCPs were synthesized with precipitation method changing the concentration of doped Sr ions. Crystal structures of these Sr-doped OCPs were examined by the powder X-ray diffraction, which showed all the samples are single phased and no secondary phase could be observed. Elemental analysis was also carried out with Energy Dispersive X-ray (EDX) analyzer equipped with the scanning electron microscope (SEM) to confirm the concentration of Sr ions in OCP. For the local environment analysis of Sr ions in OCP, Sr-L_3 XANES spectra were observed at BL2A, UVSOR, in a total electron mode. Sample powders were settled on the carbon adhesive tape, which was put on the first dinode of the electron multiplier. The synchrotron radiations from the storage ring was monochromatized with the InSb(111) double-crystal monochrometer. Observed Sr-L_3 XANES spectra are shown in Fig. 1. Although it can be determined that Sr is divalent from this comparison, we cannot get any further information on local environment of Sr ions in OCP only from these experiments. To get more information, theoretical XANES spectra for the models of Sr-doped OCP were constructed by the all-electron linearized augmented wave plus local orbital package, WIEN2k [7], with core-hole effect. Furthermore solution energy for these models were also calculated with same package. Considering the above experimental and theoretical XANES and theoretical solution energy the local environment of Sr ions in OCP could be determined.

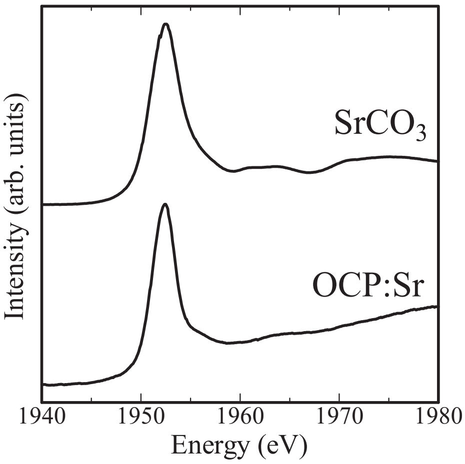

Fig. 1. Observed Sr-L_3 XANES spectra of $SrCO_3$ and Sr-doped OCP.

[1] H. Kawamura, A. Ito, S. Miyakawa, P. Layrolle, L. Ojima, H. Naito, N. Ichinose and T. Tateishi, J. Biomed. Mater. Res. **50** (2000) 184.
[2] K. Kawabata, H. Sato and T. Yamamoto, J. Ceram. Soc. Jpn. **116** (2008) 108.
[3] K. Kawabata, T. Yamamoto and A. Kitada, Physica **B406** (2011) 890.
[4] K. Kawabata, T. Yamamoto and A. Kitada, Mater. Trans. **56** (2015) 1457.
[5] K. Kawabata, H. Sato and T. Yamamoto, UVSOR Activity Report 2007 **35** (2008) 108.
[6] K. Kawabata and T. Yamamoto, UVSOR Activity Report 2010 **38** (2011) 110.
[7]P. Blaha, K. Schwarz, G.K.H. Madse, D. Lvasnicka, J. Luiz, WIEN2k (Wien, Austria, Univ. Vienna, 2001).

BL2A

P-*K* XANES Study for Hydration Reaction of α-Tricalcium Phosphate in Aqueous Solutions with Various Ions

H. Murata, R. Hashii and A. Nakahira
Department of Materials Science, Osaka Prefecture University, Sakai 599-8531, Japan

A number of biomaterials which are used in human bodies have been developed in order to improve quality of life (QOL) for a long time. Calcium phosphates are promising biomaterials which is used as alternative materials of human bones and teeth. α-tricalcium phosphate ($Ca_3(PO_4)_2$, α-TCP) is one of main components of bone cements which are hydrated and hardened in human bodies.[1] Hydration of α-TCP usually forms hydroxyapatite ($Ca_5(PO_4)_3OH$, HAp) of which human bones and teeth are composed. It is known that coexistent ions and molecules in aqueous solutions affects hydration reaction of α-TCP. Since it is considered that hydration reaction starts on surface of α-TCP, it is essential to investigate surface and bulk states of α-TCP hydrated with various kinds of environments.

X-ray absorption near edge structure (XANES) is a powerful tool to investigate local structures. In soft X-ray region, XANES analyses can reveal both of surface and bulk states using methods with different attenuation length, electron yield and fluorescent yield.[2] In detail, electron yield method collects information around several nano-meters below the surface while fluorescent yield done around several micro-meters below it. In this study, we investigated surface and bulk structures of hydrated α-TCP in aqueous solutions which contains various kinds of ions with P-*K* XANES.

α-TCP powders were purchased from Taihei Chemical Industrial Co., Ltd. They were soaked in aqueous solutions with various kinds of ions. P-*K* XANES spectra were collected at BL2A in UVSOR by a total electron yield (TEY) mode with a drain current method and a partial fluorescent yield (PFY) mode with a silicon drift detector (SDD). Samples were mounted using carbon tapes on Cu plates. X-ray beam was monochromated using InSb double crystals.

Figure 1 shows typical P-*K* XANES spectra of α-TCP samples hydrated in 0.1 mol/L NH_3 aqueous solution at different temperature for 24 h and reference materials. P-*K* XANES of α-TCP has different features from those of HAp and we can distinguish from each other. P-*K* XANES of samples shows that α-TCP hydrated at 70 °C and 80 °C were transformed to HAp while α-TCP hydrated at 37 °C still remained.

Co-existent ions, such as Zn^{2+}, disturb hydration reaction of α-TCP. We investigated α-TCP samples hydrated in aqueous solutions which contains Zn^{2+}. Both of TEY and PFY results indicated that samples soaked in the solution for 12 h remained while samples were transformed to HAp in the aqueous solution without Zn^{2+}. Powder X-ray diffraction analyses gave the same tendencies to that of P-*K* XANES. These results means that hydration of α-TCP to HAp does not occur even on the surface. Therefore, It is implied that hydration reaction of α-TCP to HAp do not simply occur on the surface but relate solution-reprecipitation process.

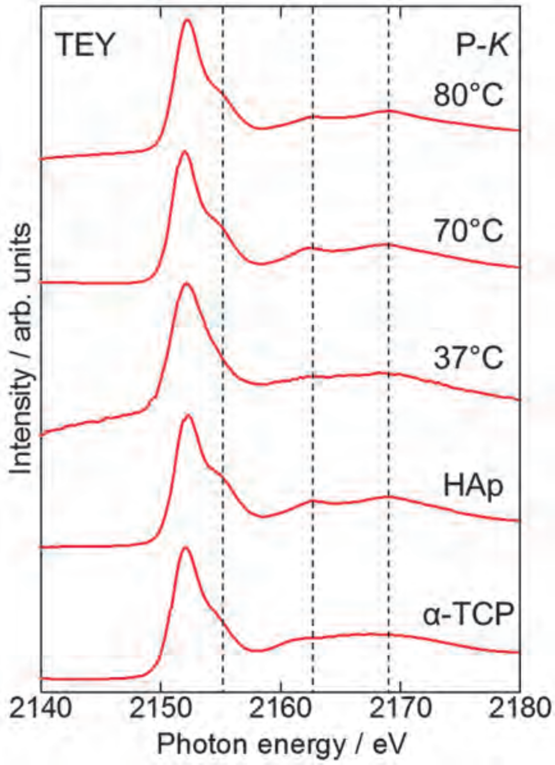

Fig. 1. Typical P-*K* XANES spectra of α-TCP hydrated in different temperature for 24 h and references materials.

[1] R.G. Carrodeguas and S. De Aza, Acta Biomater. **7** (2011) 3536.
[2] M. Kasrai *et al.*, Appl. Surf. Sci. **99** (1996) 303.

BL2A

Ga L_3-edge XAFS Analysis of Ga_2O_3 Loaded Al_2O_3 Photocatalysts

T. Yoshida[1], R. Ito[2], M. Akatsuka[2], Y. Kato[2], A. Ozawa[2], M. Yamamoto[1] and T. Tanabe[1]
[1]Advanced Research Institute for Natural Science, Osaka City University, Osaka 558-8585, Japan
[2]Graduate School of Engineering, Osaka City University, Osaka 558-8585, Japan

Recently Ga_2O_3 has attracted a lot of interests as a photocatalyst for water splitting and CO_2 reduction with water, and various efforts have been paid to improve its photocatalytic activity. Yamamoto et al. have reported improvement of photocatalytic activity for CO_2 reduction with water under UV irradiation using Ag as a co-catalyst. In the present study, we have focused to geometrical or morphological effects of Ga_2O_3 particles supported on Al_2O_3 (referred as Ga_2O_3/Al_2O_3, hereafter) for water splitting and CO_2 reduction under UV light irradiation without using the Ag cocatalyst. The reasons of utilization of Al_2O_3 as the support are twofold, (1) to increase surface area of Ga_2O_3, as evidenced by the observation that Ga_2O_3/Al_2O_3 was used for the removal of NOx, and (2) that Al_2O_3 hardly show the photocatalytic activity for both water splitting and CO_2 reduction.

Ga_2O_3/Al_2O_3 photocatalyst samples were prepared by an impregnation method. $Ga(NO_3)_3\cdot 8H_2O$ (Kishida Chemical Co. Ltd. purity 99.0%) and 1.0 g γ-Al_2O_3 (Sumitomo Chemical Co. Ltd. purity 99.99%) were added to 200 mL of distilled water and stirred with a magnetic stirrer in air and dried up, followed by calcination at 823 K for 4h, resulting the Ga_2O_3/Al_2O_3 samples. The loaded amounts of Ga_2O_3 were 5, 10, 20, 40 and 60 wt%. Pure Al_2O_3 and unsupported Ga_2O_3 samples (referred as 0 and 100 wt%, respectively) were also prepared in the similar procedure. Ga L_3-edge XANES were measured with the beam line of BL5S1 at Aichi Synchrotron Radiation Center and BL2A at UVSOR, Institute for Molecular Science in Japan, respectively.

Photocatalytic CO_2 reduction with H_2O under UV light irradiation was tested for 0.1 g of one of the samples set in a fixed-bed flow reactor cell under CO_2 gas flow. The UV light intensity was 35 mW/cm^2 in the range of 254 ± 10 nm. Before the test, the sample was irradiated with a 300 W Xe lamp for 1h under CO_2 gas flow with the flow rate of 20.0 mL/min. Then the reduction test was started introducing a $NaHCO_3$ aqueous solution (1.0M) of 10.0 mL and CO_2 gas with a flow rate at 3.0 mL/min under the UV light irradiation. The reaction products (CO, H_2 and O_2) were analyzed by a gas chromatograph equipped with a thermal conductivity detector (GC-TCD).

All prepared Ga_2O_3/Al_2O_3 samples have shown significantly higher photocatalytic activity compared to that of pure Ga_2O_3 (non-supported Ga_2O_3). The cause of the improvement is discussed considering detailed characterizations by Ga L_3-edge XAFS measurements.

Figure 1 shows Ga L_3-edge XANES spectra. A peak appeared near 1123 eV is caused by a Ga-O-Al bond. [1-3] For lower Ga_2O_3 loaded samples, this peak was relatively high compared to other peaks. This indicates that some interaction between Ga_2O_3 and Al_2O_3 occurred in lower loaded samples. For higher Ga_2O_3 loaded samples, the peak intensity at 1123 eV became less and the spectrum transformed to that of Ga_2O_3 indicating loaded Ga_2O_3 well crystallized. The result of XANES analysis was quite consistent with that of our separate EXAFS and XPS analyses.

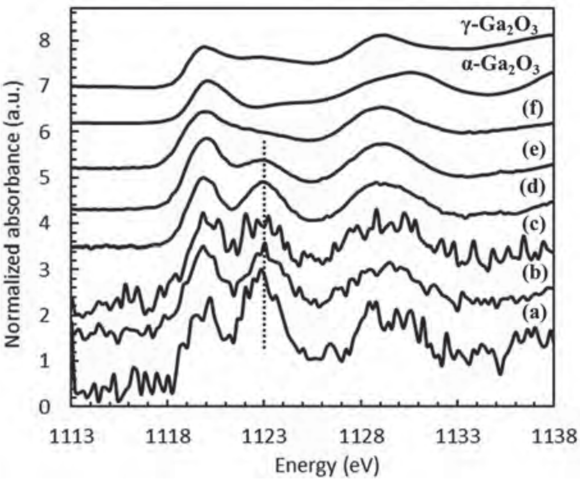

Fig. 1. Ga L_3-edge XANES spectra of all prepared samples. The spectrum of β-Ga_2O_3 is also given for comparison. (a) 0.15 vol% Ga_2O_3/Al_2O_3 (b) 0.32 vol% Ga_2O_3/Al_2O_3 (c) 0.73 vol% Ga_2O_3/Al_2O_3 (d) 2.6 vol% Ga_2O_3/Al_2O_3 (e) 4.2 vol% Ga_2O_3/Al_2O_3 (f) 100 vol% Ga_2O_3/Al_2O_3.Peaks appeared at 1123 eV is assigned to be caused by Ga-O-Al bond formation.

[1] K. Shimizu, M. Takamatsu, K. Nishi, H. Yoshida, A. Satsuma, T. Tanaka, S. Yoshida and T. Hattori, J. Phys. Chem. B **103** (1999) 1542.
[2] X. T. Zhou, F. Heigl, J. Y. P. Ko, M. W. Murphy, J. G. Zhou, T. Regier, R. I. R. Blyth and T. K. Sham, Phys. Rev. B **75** (2007) 125303.
[3] N. H. Tran, R. N. Lamb, L. J. Lai and Y. W. Yang, J. Phys. Chem. B **109** (2005) 18348.

BL2A

Removal of Elastic Scattering for Partial Fluorescence Yield XANES Measurements

H. Murata

Department of Materials Science, Osaka Prefecture University, Sakai 599-8531, Japan

X-ray absorption near edge structure (XANES) is a powerful tool for materials science since its targets are widely varied. For example, ultra-dilute dopants (~ ppm), thin films, amorphous materials can be analyzed. In soft X-ray region, it is difficult to use transmission mode due to low transparency. Instead, electron yield and fluorescent yield method were often adapted for XANES measurements. Although there are some problems such as "self-absorption effect", a number of beamlines for soft X-ray absorption introduced fluorescence yield method. In the case of UVSOR, a silicon drift detector (SDD) for partial fluorescent yield (PFY) method are available at BL2A and BL4B. [1, 2] Using SDD, elastic scattering of incident X-ray was sometimes observed. Since energy of incident X-ray scans from low to high, usual "region of interest" (ROI) sampling cannot remove elastic scattering. In this study, energy variable fitting method was developed to removal elastic scattering for PFY XANES measurements.

PFY XANES measurements were performed at BL2A in UVSOR. X-ray beam was monochromated by beryl, KTP and InSb double crystals. Conversion of SDD channel to X-ray energy were estimated using linear function. Its factors were determined using several energy of incident X-ray. It was noted that rather strong elastic scattering was observed in several cases. Amorphous materials and samples containing nano-particles gave strong elastic scattering due to their broad X-ray diffraction pattern, halo pattern. In addition to this, ultra-dilute dopants also done since SDD are moved close to samples to improve detection efficiency of fluorescent X-ray. Therefore SiO_2 was diluted by TiO_2 nanopowder for model samples.

Figure 1 shows typical X-ray fluorescence spectra of SiO_2 diluted by TiO_2 nano-powders. Elastic scattering of incident X-ray was also detected. As energy of incident X-ray increase, peaks of elastic scattering were shifted. Figure 2 shows XANES spectra estimated by Si-K_α and elastic scattering of incident X-ray. It was note that the elastic scattering have intensities below Si-K absorption edge. Elastic scattering have small peak at the white line of SiO_2 due to overlapping of Si-K_α and the elastic scattering. Therefore it behave as background. We also measured more diluted samples, the background caused by the elastic scattering were well reduced using this method. Therefore, this method were useful for samples of which fluorescent X-ray was overlapped.

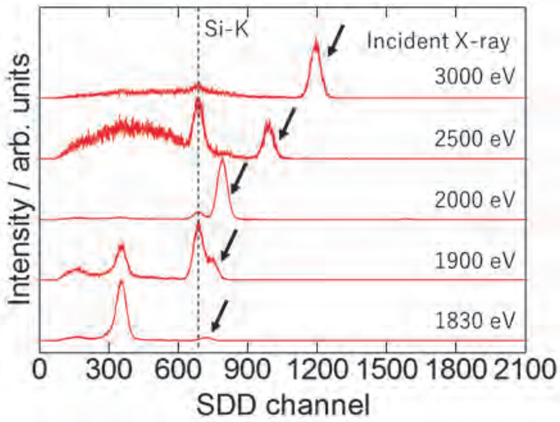

Fig. 1. Typical fluorescent X-ray spectra of SiO_2 diluted by TiO_2 nano-powders with different inciden X-ray energy. Arrows indicates elastic scattering of incident X-ray.

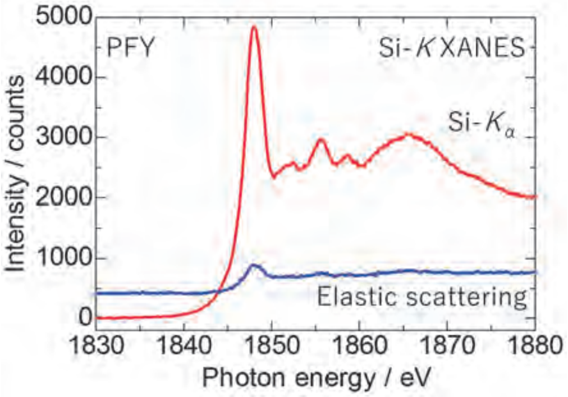

Fig. 2. Si-K XANES of SiO_2 diluted by TiO_2 nano-powders. Red and blue lines indicates spectra measured by Si-K_α X-ray and elastic scattering of incident X-ray.

[1] H. Murata *et al.*, UVSOR Activity Reports 2013 **41** (2014) 52.
[2] H. Murata *et al.*, UVSOR Activity Reports 2013 **41** (2014) 56.

BL2A

Local Environment of Multivalent Cations in Ion-Exchanged Layered Titanate and Titanate Nanotubes

A. Fujimoto, H. Murata and A. Nakahira
Department of Materials Science, Osaka Prefecture University, Sakai 599-8531, Japan

Titanate nanotubes have attracted many researchers due to their unique structures.[1] They consists of TiO_6 octahedra linked by sharing edges, which is considered to be based on structures of layered titanate. Titanate nanotubes and layered titanates have cation-exchange ability. Since they have variable-length interlayers, various kinds of cations can be incorporated. Generally, univalent cations, M^+, are easily ion-exchanged into them. On the other hand, multivalent cations are slightly difficult to introduce into them. In this study, we tried to synthesize ion-exchanged titanate nanotubes and layered titanates with multivalent cations, and investigated their local environments by X-ray absorption near edge structure (XANES).

Layered titanate samples were prepared with a solid-state reaction method. Na_2CO_3 and TiO_2 were used as starting materials. They were mixed and ground in an agate mortar. Then, they were calcined at 1000°C for 8 h. Titanate nanotubes samples were synthesized by the hydrothermal method based on Kasuga *et al.* [2]. Anatase-type TiO_2 nano-powders and 10 mol/L of NaOH aqueous solution were sealed into Teflon-lined autoclave and they were heated at 150°C for 24 h. Obtained samples were ion-exchanged in aqueous solutions of HCl, $MgCl_2$ or $AlCl_3$.

XANES spectra were measured at BL2A in UVSOR. Partial fluorescent yield method with a silicon drift detector (SDD) were adapted. X-ray beam was monochromated using beryl double crystals for Na-*K* and Mg-*K* edge, and KTP double crystals for Al-*K* edge. Samples were mounted by a carbon tape on Ti plates. It was noted that X-ray fluorescence from ion-exchanged titanate nanotubes gave rather week signals. For example, only 10 cps for Al-*K* were observed at the peak top that the incident photon energy was 1570 eV. Therefore, we set maximum 15 second/points for dwell time.

As an example of results, fig.1 shows typical Al-*K* XANES spectra of Al^{3+}-exchanged samples and references. Al^{3+}-exchanged titanate nanotubes and $Na_2Ti_3O_7$ have similar spectra to each other. This means local environments of Al^{3+} in them were also similar. When titanate nanotubes and $Na_2Ti_3O_7$ are soaked in aqueous solutions, pH usually increase because of H^+ incorporation into them, which often forms hydroxides. But our samples have different spectra from those of hydroxide and starting materials. These results implied that Al^{3+} were incorporated into titanate nanotubes and layered titanates. Detail analyses of local environments for Al^{3+} in titanate nanotubes and layered titanates have been in progress using XANES simulation by first-principles manner.

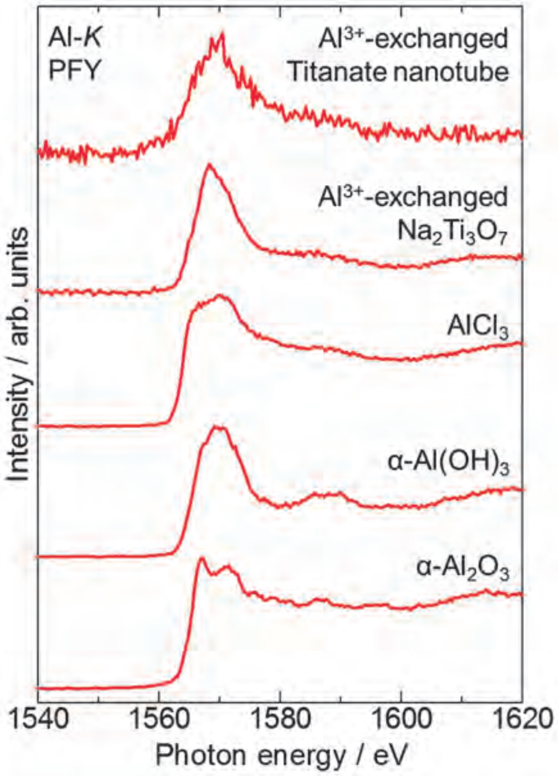

Fig. 1. Typical Al-*K* XANES spectra of titanate nanotubes and layered titanate which were ion-exchanged in $AlCl_3$ aqueous solutions. Spectra of reference samples were also shown.

[1] D. V. Bavykin *et al.*, Adv. Mater. **18** (2006) 2807.
[2] T. Kasuga *et al.*, Langmuir **14** (1998) 3160.

BL2A

Local Structure Investigations of $Y_3Al_5O_{12}$ Induced by Swift Heavy Ions Irradiations

S. Yoshioka[1], K. Yasuda[1], S. Matsumura[1], N. Ishikawa[2], K. Kobayashi[3] and K. Okudaira[4]
[1]Department of Applied Quantum Physics and Nuclear Engineering, Kyushu University, Fukuoka 819-0395, Japan
Nuclear Science and Research Center, Japan Atomic Energy Agency (JAEA), Tokai 319-1184, Japan
[3]Kyushu Synchrotron Light Research Center (SAGA-LS), Tosu 841-0005, Japan
[4]Graduate School of Advanced Integration Science, Chiba University, Chiba, 263-8522, Japan

Yttrium aluminum garnet ($Y_3Al_5O_{12}$ or YAG) is considered as an important material for laser optical application. Ion irradiations are currently used to tailor materials properties. In particular, for garnet structure materials, swift heavy ion irradiations, produce amorphous tracks that can change the microstructure and the magnetic or magneto-optical properties[1]. In the present study, we made a combined study of NEXAFS measurements and first principles calculations on $Y_3Al_5O_{12}$ with special interests on the local environment of Y and Al after irradiated with swift heavy ions (SHI).

Synthetic single crystals of $Y_3Al_5O_{12}$ were used in this study. The crystals were cut into sheets with a (111) plane surface and were polished to a mirror finish. The specimens were irradiated with 340 MeV Au ions to fluences of 3×10^{11} and 1×10^{12} cm^{-2} at the H1 beamline of the tandem ion accelerator facility at the Japan Atomic Energy Agency (JAEA) in Tokai. Al *K*-edge and Y L_3-edge XANES measurements were performed at the BL2A beamline of UVSOR Okazaki, Japan, using the total electron yield method (TEY). A Beryl and an InSb double crystal monochromators defined Al *K* and Y L_3 absorption edges, respectively. The samples were set with their surface perpendicular to the incident X-ray beam. All measurements of XANES spectra were carried out in vacuum of 1×10^{-5} Pa at room temperature. To interpret the local structure from the experimental spectra, we used theoretical spectra by the full-potential linearized augmented plane wave (APW) plus local orbitals technique as implemented in WIEN2k code.

Figure 1 shows the XANES spectra with the Al *K*-edge acquired from the $Y_3Al_5O_{12}$ samples before and after irradiation with 340 MeV Au ions with fluences of 3×10^{11} and 1×10^{12}. The Al *K*-edge spectrum features of the irradiated sample show significant change with increasing SHI irradiation fluences. On the other hand, the Y L_3-edge spectrum features of the irradiated samples are very similar to that the pristine sample, as shown in Fig. 2. These results suggest that the SHI irradiations to the $Y_3Al_5O_{12}$ sample preferentially induced the local structure changes of Al, compared to Y.

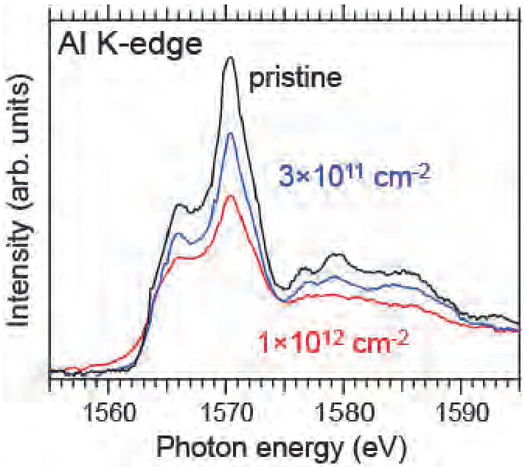

Fig. 1. Al *K*-edge XANES spectra of pristine and irradiated $Y_3Al_5O_{12}$ with 340 MeV Au ions to fluences of 3×10^{11} and 1×10^{12} cm^{-2}.

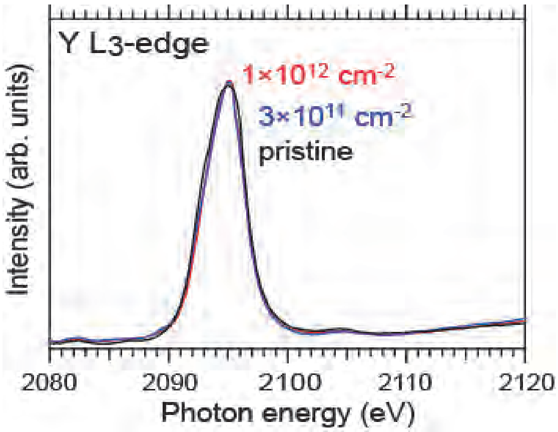

Fig. 2. Y L_3-edge XANES spectra of pristine and irradiated $Y_3Al_5O_{12}$ with 340 MeV Au ions to fluences of 3×10^{11} and 1×10^{12} cm^{-2}.

[1] J. M. Costantini, S. Miro, F. Beuneu and M. Toulmonde, J. Phys.: Condens. Matter **27** (2015) 496001.

BL2B

Excitation Energy Dependent UPS of Solution-processed Perovskite Film

A. Mirzehmet[1] and H. Yoshida[2,3]
[1]*Graduate School of Advanced Integration Science, Chiba University, Chiba 263-8522, Japan*
[2]*Graduate School of Engineering, Chiba University, Chiba 263-8522, Japan*
[3]*Molecular Chirality Research Center, Chiba University, Chiba 263-8522, Japan*

In the perovskite solar cell, the interfaces play crucial roles in the charge extraction, transfer and recombination. The general chemical formula for the perovskite is ABX_3. The most commonly used working layer is the solution-processed film of methylammonium lead iodide ($MAPbI_3$) where A, B, and X are methylammonium (MA), lead (Pb) and iodine (I), respectively. The electronic properties of the interface involving the perovskite ABX_3 should be strongly affected by the elements of the surface termination layer being either A, B, or X_3.

Previously, we have examined the uppermost surface elements of the solution-processed $MAPbI_3$ perovskite film by comparing the valence band spectra measured with different probing depths using ultraviolet photoelectron (UPS) and metastable-atom electron (MAES) spectroscopies [1]. In this work, we have measured the excitation energy dependent UPS in the range between 24.3 eV and 110 eV to confirm our peak assignment.

Figure 1 shows the energy dependent UPS. Based on the reported DFT calculations [2, 3], we tentatively assigned the peak at 3.3~3.6 eV to the I 5p derived-states, and the peak at 4.7 eV to the Pb 6s and 6p derived-states. The features at 8.8 and 10.8 eV are dominated by MA molecular states, with additional Pb 6s states at 8.8 eV.

The intensities of the peaks vary with the excitation energy as shown in Fig. 1. The features of I 5p shows strong intensity on the low energy and decreased as the increases of the photon energy. Pb 6p and 6s, however, always shows lower intensity compared with I 5p. The features of MA (N 2p and C 2p) show strong intensity and decreased on the high energy.

The observations are fully consistent with the photoionization cross-section [4] (Fig. 2) confirming our peak assignment.

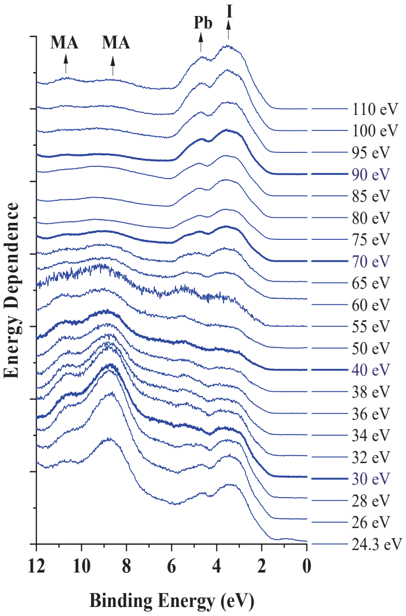

Fig. 1. Energy dependent UPS spectra of $MAPbI_3$ film.

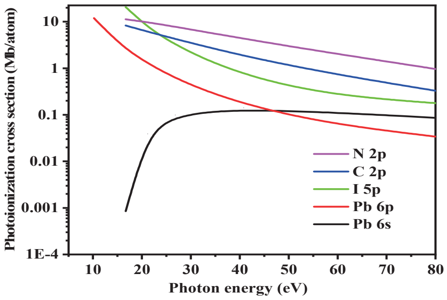

Fig. 2. Photoionization cross-section of $MAPbI_3$ elements.

[1] M. Abduheber, *et al.*, The 79th JSAP Autumn Meeting (2018).
[2] W-J. Yin *et al.,* Appl. Phys. Lett. **104** (2014) 063903.
[3] J. Endres *et al.,* J. Phys. Chem. Lett. **14** (2016) 2722.
[4] J-J. Yeh, Atomic calculation of photoionization cross-sections and asymmetry parameters (Gordon and Breach Science, Publishers, 1993).

BL3B

Correlation between Intrinsic Luminescence Intensity and Structure in $(Ca_{1-x}Sr_x)_2Al_2SiO_7$ and $(Ca_{1-x}Sr_x)_2MgSi_2O_7$ Melilite Crystals

N. Kodama, H. Kubota, T. Uematsu and T. Takahashi
Graduate School of Engineering Science, Akita University, Akita 010-8502, Japan

Crystals with a layered structure are expected to exhibit strong luminescence from peculiar two-dimensional excitons resulting from their large binding energy. $(Ca_{1-x}Sr_x)_2Al_2SiO_7$ and $(Ca_{1-x}Sr_x)_2MgSi_2O_7$ melilite crystals have a tetragonal sheet structure, which consists of five-membered rings of TO_4 (T = Al, Si, Mg) AlO_4^{5-}, SiO_4^{4-}, or MgO_4^{6-} oxoanions, resulting in self-trapped excitons (STEs) under band-to-band (interband) excitation or molecular transitions in the VUV region. The formation energy and the luminescence properties of excitons are considered to depend on the nature of the oxoanion-linked structure, such as the dimensionality (intra-layer distance) or two-dimensional modulation. To date, very little research has focused on the formation of self-trapped excitons in the dimensionality and modulation of the structure. We examined the correlation between the intrinsic luminescence intensity and the two-dimensionality and structure modulation (superstructure) in $(Ca_{1-x}Sr_x)_2Al_2SiO_7$ and $(Ca_{1-x}Sr_x)_2MgSi_2O_7$ (x = 0, 0.25, 0.5) melilite crystals. We report intrinsic luminescence from self-trapped excitons (STEs). In addition, we discuss the structural correlation of the intrinsic luminescence intensity from STEs.

Luminescence and excitation spectra of STEs in $(Ca_{1-x}Sr_x)_2Al_2SiO_7$ and $(Ca_{1-x}Sr_x)_2MgSi_2O_7$ (x = 0, 0.25, 0.5) crystals were measured in the temperature range of 14-293 K using the undulator beamline BL3B at the UVSOR facility. Under VUV excitation at 160 and 70 nm, intrinsic luminescence from self-trapped exitons (STE) was observed in these crystals.

The dependence of the intrinsic luminescence intensity on the Sr fraction x was examined for these crystals. In $(Ca_{1-x}Sr_x)_2Al_2SiO_7$, one luminescence band with a peak at 271-300 nm associated with STE appears at temperatures of 14-293 K. The luminescence spectra of $(Ca_{1-x}Sr_x)_2MgSi_2O_7$ with x = 0.0, 0.25, and 0.5 consisted of two broad bands with peaks at 238-246 nm and 340-350 nm associated with STEs in the range of 14-293 K.

Figures 1(a) and 1(b) show the luminescence spectra for $(Ca_{1-x}Sr_x)_2Al_2SiO_7$ and $(Ca_{1-x}Sr_x)_2MgSi_2O_7$ (x = 0.0, 0.25, 0.5) excited at 160 nm at 14 K.

In $(Ca_{1-x}Sr_x)_2Al_2SiO_7$, the crystal with x = 0.5 exhibited one intense STE luminescence band, and the STE luminescence intensity decreases rapidly at x = 0.25. No significant luminescence was observed at x = 0.0. On the other hand, in $(Ca_{1-x}Sr_x)_2MgSi_2O_7$, the intensity of STEs passes through a maximum at intermediate fraction x = 0.25, as x increases. For the dependence of luminescence intensity on the Sr fraction, x, two possibilities are plausible: one is a two-dimensional effect and the other is a structural modulation effect (superstructure).

First, the intra-layer distance increases with increasing x, because of the larger ionic radius involved in substituting Sr^{2+}. One possible explanation for such an intense luminescence at x = 0.5 in $(Ca_{1-x}Sr_x)_2Al_2SiO_7$ and $(Ca_{1-x}Sr_x)_2MgSi_2O_7$ (x = 0.0, 0.25, 0.5) is that a larger two-dimensional effect, i.e., the intra-layer distance increases with increasing Sr fraction x, which leads to larger two-dimensionality. However, the enlargement of intra-layer distance is not very large even at x = 0.5 (a few percent). The second possible explanation is that a modulation effect of commensurate or incommensurate structure leads to an increase in local sites with larger distortion potentials. The formation of STEs and the luminescence intensity may be strongly affected by whether the crystals form a modulated structure (commensurate or incommensurate phase) and by the amplitude of modulation. We found that a $(Ca_{1-x}Sr_x)_2Al_2SiO_7$ crystal with 0.5, which shows the most intense luminescence among the three x fractions (0.0, 0.25, and 0.5), exhibited commensurate modulation with two-fold periodicity along the *c*-axis by X-ray diffraction. Moreover, incommensurately and two-dimensionally modulated structures with Sr fractions, x, ranging from 0.04 to 0.32 have been observed in $(Ca_{1-x}Sr_x)_2MgSi_2O_7$ [1]. Based on these structural changes with Sr composition, the intense luminescence at x = 0.5 is considered to be due mainly to a structural modulation effect.

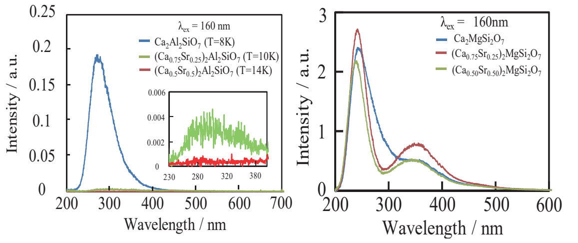

(a) (b)

Fig. 1. Dependence of intrinsic luminescence on Sr fraction x in (a) $(Ca_{1-x}Sr_x)_2Al_2SiO_7$ and (b) $(Ca_{1-x}Sr_x)_2MgSi_2O_7$ (x = 0.0, 0.25, 0.5) at 14 K under excitation at 160 nm. The inset shows the enlarged luminescence spectra in the range from 230 to 390 nm.

[1] J. C. Jiand, M. Schosnig, A. K. Schapaer, K. Ganster, H. Ragaer and L. Toth, Phys. Chem. Minerals **26** (1998) 128.

BL3B

Evaluation of Fluorescence Lifetimes of Scintillation Fibers

H. Oikawa, M. Kitaura, A. Ohnishi, Y. Tajima and H. Y. Yoshida
Yamagata University, yamagata 990-8560, Japan

In high-energy physics experiments, particle detectors with fast time response are absolutely imperative. Especially, plastic scintillators are the first choice for radiation converter, because they have fluorescence with short decay time of nanosecond range. This feature is necessary for successive detection of particles at high count rates. In order to develop plastic scintillators, it is indispensable to evaluate fluorescence lifetimes with the use of a short pulse light source in the wide range from visible to vacuum ultraviolet. In the present study, we have measured fluorescence spectra and decay curves for some polystyrene-based plastic scintillators.

Samples used in our experiment can be available commercially, and they are labelled as Y-8, Y-11, B-3, O-2, R-3, and SCSF-78. As an example, the fluorescence spectrum of SCSF-78 is shown in Fig. 1. This spectrum was obtained under excitation at 200 nm. Two bands peaking at 335 nm and 435 nm appear in Fig. 1. Fluorescence decay curves were measured under single bunch operation by adopting time-correlated single photon counting method. The decay curve for the 335 nm band is shown in Fig. 2. The blue line indicates experimental data.

Lifetimes were analyzed by using the data analysis framework named "ROOT" [1]. For the lifetime analysis, we adopted the equation

$$\mathrm{I}(t) = \int_{-\infty}^{\infty} \mathrm{P}(t')\,\mathrm{G}(t-t')\,\theta(t'-T_0)\mathrm{d}t', \qquad (1)$$

where

$$\mathrm{P}(t) = \sum_i \exp(-t/\tau_i), \qquad (2)$$

and

$$\mathrm{G}(t-t') = A\exp\left(-\frac{(t-t'-\mu_1)^2}{2\sigma_1^2}\right) + B\exp\left(-\frac{(t-t'-\mu_2)^2}{2\sigma_2^2}\right). \quad (3)$$

$\mathrm{I}(t)$ represents the fluorescence decay curve observed. $\mathrm{P}(t)$ represents the superposition of fluorescence decay curve functions. $\mathrm{G}(t-t')$ represents the resolution of the experimental system, the time structure of the beam, and so on. A sum of two Gaussians (3) successfully describes the measurement of the $\mathrm{G}(t-t')$ in this analysis. $\theta(t'-T_0)$ is assumed a step function to reproduce the origin of time T_0. Table 1 shows fluorescence lifetimes of samples determined in the present study, together with the excitation and emission wavelengths. Decay curves for the 355 nm and 435 nm bands of SCSF-78 are reproduced by two or three exponential decay functions. Such complicated decay curves suggest the existence of plural relaxation pathway under excitation in the fundamental absorption region of host polystyrene.

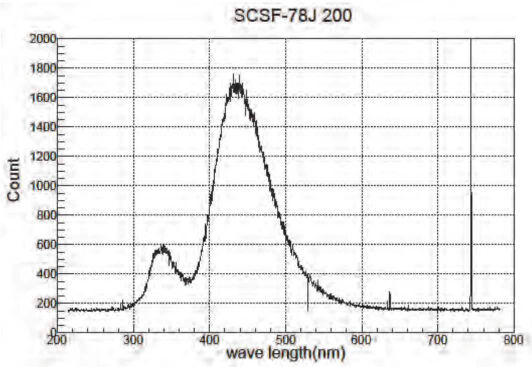

Fig. 1. Emission spectrum of SCSF-78, measured at room temperature under excitation at 200 nm.

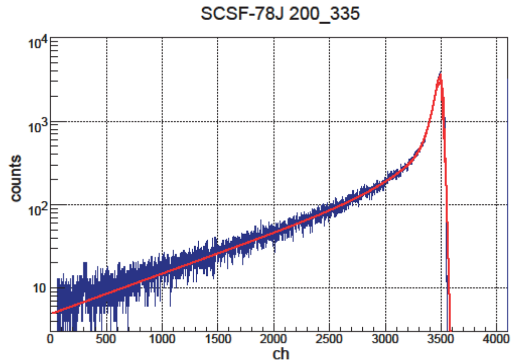

Fig. 2. Fluorescence decay curve for the 335 nm band of SCSF-78, measured at room temperature under excitation at 200 nm.

Table. 1. Fluorescence peak-wavelengths and lifetimes determined in the present study.

sample	λEX (nm)	λEM (nm)	τ1 (ns)	τ2 (ns)	τ3 (ns)
SCSF78	200	335	0.934	4.68	17.4
	200	435	3.33	14.7	
	277	335	0.694		
	277	435	2.10		
	351	435	2.01		
Y11	430	495	6.92		
Y8	455	526	7.24		
B3	351	442	2.04		
O2	535	577	5.32		
R3	550	606	6.70		

[1] R. Brun and F. Rademakers, Nucl. Instrum. Methods Phys. Res. A **389** (1997) 81.

BL3B, BL7B

Effect of Ce and Mg Concentration Ratio on the Properties of $Gd_3Al_2Ga_3O_{12}$ Single Crystal Scintillators

K. Bartosiewicz[1], A. Yoshikawa[1,2,3], S. Kurosawa[2,4], A. Yamaji[1] and M. Nikl[5]
[1]*Institute for Material Research, Tohoku University, Sendai 980-8577, Japan*
[2]*New Industry Creation Hatchery Center, Tohoku University, Sendai 980-8579, Japan*
[3]*C&A corporation, T-Biz, Sendai 980-8579, Japan*
[4]*Facility of Science, Yamagata University, Yamagata 990-8560, Japan*
[5]*Institute of Physics, Academy of Sciences of the Czech Republic, Na Slovance 1999/2, Prague 8, 18221, Czech Republic*

In gadolinium gallium aluminum garnets ($Gd_3Al_2Ga_3O_{12}$, GAGG), efficient luminescence is dependent on dopants to create a radiative transition within the forbidden band [1]. In medical imaging, Ce^{3+} is commonly used due to fast and bright 5d→4f transition with the emission wavelength that is suitable also for semiconductor photodetectors [2]. The Ce^{3+} activated GAGG is considered as a promising candidate for the next generation Positron Emission Tomography material due to its high light yield value (~58,000 ph/MeV), fast scintillation response (~100 ns), and high density (~6.2 g/cm^3). However, this material suffers from the contribution of the undesired slow component in the scintillation response and long rise time [3]. Recently, the divalent (Me^{2+}) codoping strategy has been used in order to mitigate the degraded scintillation properties that result from charge carrier traps and have been shown to improve light yield and decay times in some scintillators [4].

The Mg^{2+} codoping in GAGG:Ce single crystal significantly accelerates the scintillation decay time, but at the same time the light yield become strongly reduced [4]. To deeper understand the effect of Mg^{2+} codoping content on the scintillation characteristics of GAGG:Ce, we recorded thermally stimulated luminescence (TSL), see Fig.1. The results show that increasing Mg^{2+} concentration creates new peaks within the whole recorded temperature range. This means that Mg^{2+} codoping increases the number of metastable levels, which act as electron traps. Due to the transformation of Ce^{3+} to Ce^{4+} crystal lattice become perturbed. Consequently, many defects arise, which can significantly diminish scintillation performances. Moreover, a rich pattern of TSL peaks over RT is due to the presence of the deep electron traps, which are associated with oxygen vacancies. To conclude, TSL measurements revealed that Mg^{2+} codoping reduces the quality of the crystal lattice due to the creation of many defects acting as electron traps.

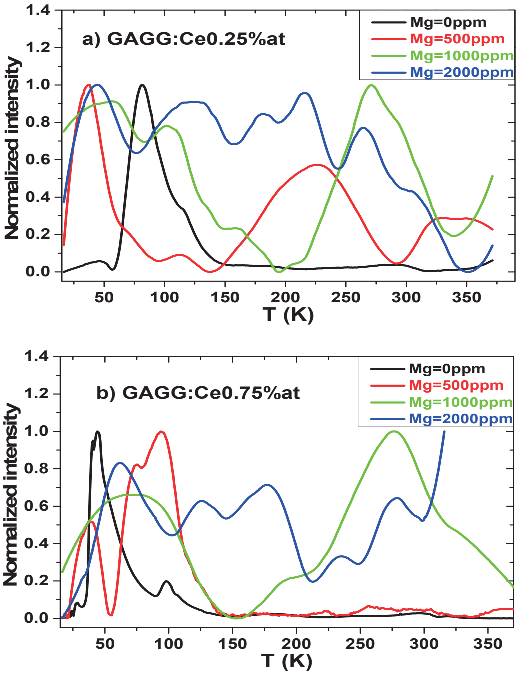

Fig. 1. Normalized TSL glow curves (measured in the 10-3800 K temperature range for the for Mg^{2+} free and Mg^{2+} codoped GAGG:Ce single crystals. Nominal content of Ce^{3+} was (b) 0.25% and (b) 0.75% at, irradiated at 10 K by UV radiation (12.4 eV)

[1] M. Nikl and A. Yoshikawa, Adv. Optical Mater. **3** (2015) 463.

[2] C. Ronda, J. Solid State Sci. Technol. **5** (2016) R3121.

[3] M. Lucchini *et al.,* Instr. Meth. Phys, Research A **852** (2017) 1.

[4] C. Foster *et al.*, J. Cryst. Growth, in press (10.1016/j.jcrysgro.2018.01.028).

BL3B

Estimation of Optical Properties of RE$_2$Si$_2$O$_7$ Sintered Compacts Using the UVSOR Synchrotron Facility

T. Horiai[1], S. Kurosawa[2], A. Yamaji[1], S. Kodama[1], S. Yamato[1], Y. Shoji[1,4], M. Yoshino[1],
H. Sato[2], Y. Ohashi[2], K. Kamada[2,3], Y. Yokota[2] and A. Yoshikawa[1,2,3]
[1]Institute for Materials Research, Tohoku University, Sendai 980-8577, Japan
[2]New Industry Creation Hatchery Center (NICHe), Tohoku University, Sendai 980-8579, Japan
[3]C&A Corporation, Aramaki, Sendai 980-8579, Japan

Scintillation crystals convert energy of ionizing radiation such as gamma-ray and X-ray into multiple photons of energy 2~8 eV, and are used in many fields, as radiation detectors [1-3]. The Ce-doped RE$_2$Si$_2$O$_7$ (RE= rare-earth ions) scintillators have been reported to have a high light yield, short decay time and good thermal stability. Here, the crystal system of RE$_2$Si$_2$O$_7$ are changed by rare-earth ions [4]. In addition, the emission and excitation spectra of Ce^{3+} 5d-4f transition are strongly depend on the host crystal structure of RE$_2$Si$_2$O$_7$ due to the involved Ce^{3+} 5d orbital are not shielded by outer electrons. Therefore, it is important to estimate the influence of crystal structure of RE$_2$Si$_2$O$_7$ and the ionic radii of rare-earth ions on optical properties of Ce-doped RE$_2$Si$_2$O$_7$. In addition, the bandgap energy of RE$_2$Si$_2$O$_7$ is also affected when the rare-earth ion changes. In this study, we estimated the bandgap energy of RE$_2$Si$_2$O$_7$ (RE=La, Gd, Y and Lu) to investigate the change in bandgap energy due to the ionic radii of rare-earth ions.

We prepared (Ce$_{0.01}$ RE$_{0.99}$)$_2$Si$_2$O$_7$ (RE=La, Gd, Y and Lu) sintered compacts.; As starting materials, we used La$_2$O$_3$, CeO$_2$, Gd$_2$O$_3$, Y$_2$O$_3$, Lu$_2$O$_3$ and SiO$_2$ powders the purities of which were at least 99.99%. After weighing, the powders were well wet-blended, and they were molded into pellets using a hydraulic press, and the pellets were pre-sintered at 1550 ºC for 12 hours under air. Finally, we sintered the pellets at 1600 ºC for over 24 hours under air. The emission spectra of these sintered compacts were measured with a spectrometer (spectoropro-300i, Acton research), and the excitation spectra were measured with a photo diode (IRD, AXUV 100) at BL3B of UVSOR.

Figure 1 shows the emission spectra of Ce-doped RE$_2$Si$_2$O$_7$ (RE=La, Gd, Y, Lu). From this figure, the emission peak due to Ce^{3+} 5d$_1$-^{2}f$_{5/2}$ was changed with changes in the ion radii of rare-earth ions. The excitation spectra of Ce-doped RE$_2$Si$_2$O$_7$ (RE=La, Gd, Y, Lu) is shown in Fig. 2. The result of estimating the host excitation band peak showed that the bandgap energies of La$_2$Si$_2$O$_7$, Gd$_2$Si$_2$O$_7$, Y$_2$Si$_2$O$_7$ and Lu$_2$Si$_2$O$_7$ were approximately 7.0, 6.9, 7.2 and 6.9 eV, respectively. All samples were found to have high bandgap energy of over 7.0 eV.

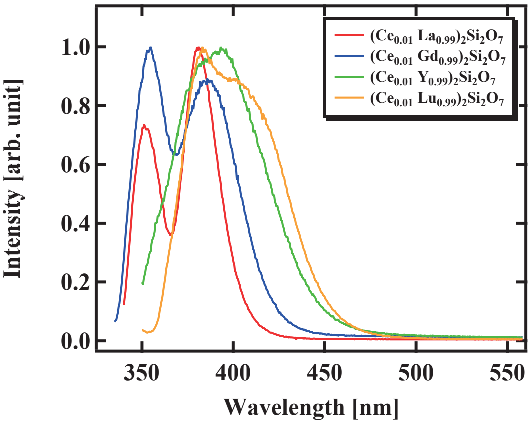

Fig. 1. Emission spectra of Ce-doped RE$_2$Si$_2$O$_7$ (RE=La, Gd, Y and Lu) at 6 K

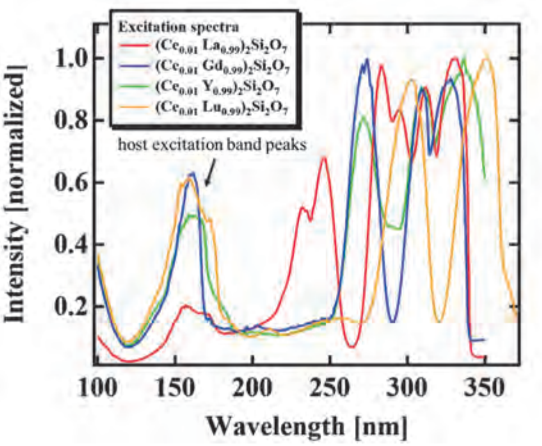

Fig. 2. Excitation spectra of Ce-doped RE$_2$Si$_2$O$_7$ (RE=La, Gd, Y and Lu) at 6 K

[1] C. Rozsa, R. Dayton, P. Raby, M. Kusner and R. Schreiner, IEEE Trans. Nucl. Sci. **37** (1996) 966.
[2] A. Baberdin, A. Dutova, A. Fedorov, M. Korzhik, V. Ligoun, O. Missevitch, V. Kazak, A. Vinokurov and S. Zagumenov, IEEE Trans. Nucl. Sci. **55** (2008) 1170.
[3] C.L. Melcher, J.S. Schweitzer, R.A. Manente and C.A. Peterson, J. Crystal Growth **109** (1991) 37.
[4] J. Felsche, Journal of the Less Common Metals **21** (1970) 1.

BL3B

Temperature Dependence of PL Spectra of p-terphenyl and 1,4-bis(2-methylstyryl)benzene (bis-MSB) at 6-300 K

S. Yamato[1], S. Kurosawa[2,3], A. Yamaji[1], T. Horiai[1], S. Kodama[1], M. Abe[3], M. Yoshino[1],
Y. Ohashi[2], K. Kamada[2,4], Y. Yokota[2] and A. Yoshikawa [1,2,4]
[1]*Institute for Materials Research (IMR), Tohoku University, Sendai 980-8577, Japan*
[2]*New Industry Creation Hatchery Center (NICHe), Tohoku University, Sendai 980-8579, Japan*
[3]*Fuculty of science, Yamagata University, Yamagata 990-8560, Japan*
[4]*C&A Corporation, Sendai 980-8577, Japan.*

Neutron detectors can be used in several fields such as neutron diffraction for crystal structure analysis, social infrastructure maintenance and nuclear fusion physics [1-3]. Here, nuclear fusion technology is expected as next effective energy generation technology. In fusion reactors, neutrons are emitted from nuclear fusion reactions, and the monitoring these particles is a important technology to control fusion reactors and generate energy effectively.

Among several nuclei, the neutron cross section of hydrogen nucleus is the largest in higher energy range. ^{1}H has relatively higher cross section for the fast neutron than other materials. We focused on organic scintillators which contains many ^{1}H and have low detection efficiency for gamma rays as background noise.

Although the neutron detectors in fusion reactors can be exposed on high temperature of about from 400 to 600 K, conventional organic scintillators cannot be used at high temperature. Plastic scintillators melt at around 230 K. Liquids evaporate at high temperature and are difficult to handle. Even crystals, only low-melting-point materials were developed. As a first step, we aimed to develop the organic scintillators which can be used at over 270 K s. Also, I considered high-melting-point crystal have a potential to meet this demand.

We grew pure p-terphenyl crystal and pure 1,4-bis(2-methylstyryl)benzene (bis-MSB) crystal by the self-seeding vertical Bridgman method using an enclosed chamber [4]. Pulling down rate for growth was ~1 mm/h. The melting point of p-terphenyl and bis-MSB are 485 and 352 K, respectively.

We measured the photoluminescence (PL) emission spectra of the samples at 6-300 K with the beamline BL3B at UVSOR facility. The spectra of p-terphenyl excited by 245 nm photons and bis-MSB excited by 260 nm photons were shown in Fig. 1 and Fig. 2, respectively.

At 300 K the emission peaks of 375 and 390 nm were observed for p-terphenyl. As temperature decreased, the ratio of peak of 375 nm for 390 nm became smaller and new peak of 350 nm appeared. For bis-MSB, the emission peak of 484 nm became weaker and several peaks were appeared in shorter wavelength range as temperature decreased.

Since the molecular vibration was suppressed at lower temperature, emission peaks were split clearly. As future works, we study on the relationship between these results and temperature dependence of photo-luminesce decay time.

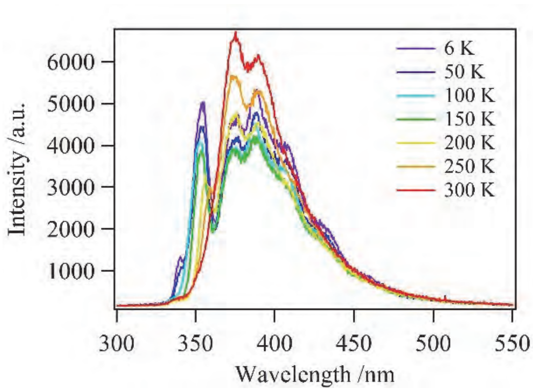

Fig. 1. Emission spectra of p-terphenyl crystal excited by 245 nm photons at 6-300 K.

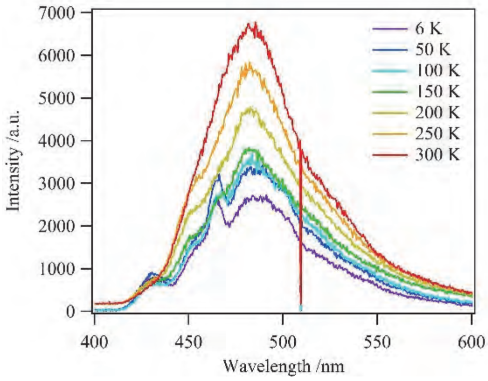

Fig. 2. Emission spectra of bis-MSB crystal excited by 260 nm photons at 6-300 K.

[1] P. Zhang *et al*, Cement and Concrete Research **108** (2018) 152.
[2] H. K. Lee *et al.*, J. Supercond. Novel Magn. **31** (2018) 1677.
[3] Y. K. Kim *et al.*, J. Instrum. **7** (2012) C06013.
[4] A. Arulchakkaravarthi *et al.*, J. Crystal Growth **234** (2002) 159.

BL3B

Low-temperature Photoluminescence Spectra of Cs_2HfI_6

S. Kodama[1], S. Kurosawa[2,3], M. Ohno[1], A. Yamaji[1], M. Yoshino[1], H. Sato[2],
Y. Ohashi[1], K. Kamada[2,4], Y. Yokota[2] and A. Yoshikawa[1,2,4]
[1]*Institute for Materials Research (IMR), Tohoku University,Sendai 980-8577, Japan*
[2]*New Industry Creation Hatchery Center (NICHe), Tohoku University, Sendai 980-8579, Japan*
[3]*Faculty of Science, Yamagata University, Yamagata 990-8560, Japan*
[4]*C&A Corporation, Sendai 980-8577, Japan.*

A_2HfX_6 (A: monovalent cation, X: halogen ion) compounds are host-emitting materials originated from self-trapped exciton (STE) [1]. Since the crystal lattice of A_2HfX_6 compounds can be a well-ordered and high symmetry cubic structure (space group: *Fm-3m*), producing a transparent single crystal is easy. Actually, Our research group has developed a Cs_2HfI_6 (CHI) single crystal as a noble red-emitting (around 650 nm) scintillator with a high light output of ~64,000 photons/MeV [2,3]. As mentioned above, the luminescence mechanism of CHI could be STE around $[HfI_6]^{2-}$, however, the detail of emission mechanism was still unclear. In this year, we evaluated the temperature dependence of CHI photoluminescence properties to study the luminescent origin.

A single-crystalline CHI specimen was synthesized from 99%-pure HfI_4 and 99.999%-pure CsI using the vertical Bridgman growth method in our laboratory. We measured photoluminescence emission spectra of CHI at from 10 K to 300 K cooled by liquid Helium in a cryostat chamber of UVSOR BL3B. The light source was a synchrotron light.

Figure 1 indicate the photoluminescence emission spectra of CHI. When the sample was excited by 400 nm at 300 K in Fig. 1 (a), the typical broad emission spectrum around 650 nm was observed. At 150 K one additional peak appeared at 550 nm, and as temperature decrease, the 550-nm-peak became very intense, while the intensity of 650-nm-peak decreased. The 550-nm-peak intensity leached the maximum at 10 K. CHI room temperature (300 K) emission excited 460 nm showed the different temperature dependence. To 8 K, the peak intensity increased, and wavelength shifted towards 700 nm.

Based on above temperature dependence, CHI was considered to have several excitation-emission bands. Moreover, the major band could change as temperature changes. Since the typical STE emission intensity increases at low temperature, the low temperature emission peak at 550 nm could be one STE band which thermally quenches above 150 K. Further study should be needed to understand the energy transfer between room temperature emission band and low temperature band. For the direct evaluation of STE center, electron paramagnetic resonance technique would be available.

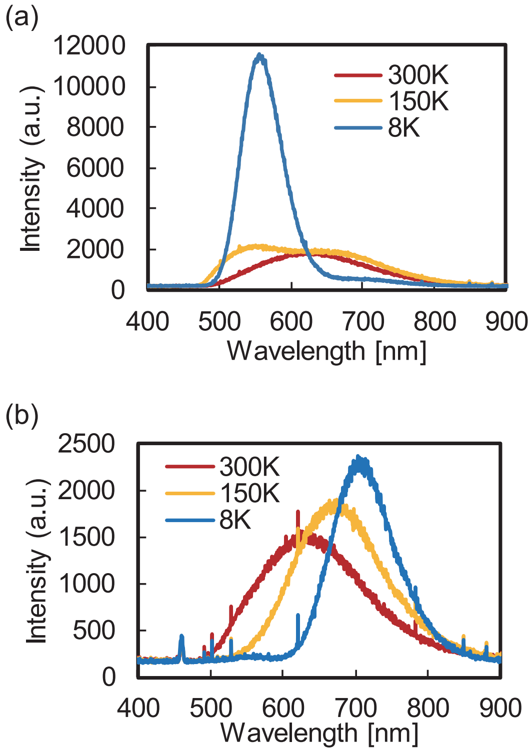

Fig. 1. Photoluminescence emission spectra of CHI crystal. (a) and (b) are spectra excited by 400 nm and 460 nm, respectively.

[1] B. Kang and K. Biswas, J. Phys. Chem. C. **120** (2016) 12187. doi:10.1021/acs.jpcc.6b02496.
[2] S. Kodama, S. Kurosawa, M. Ohno, A. Yamaji, M. Yoshino, J. Pejchal, R. Král, Y. Ohashi, K. Kamada, Y. Yokota, M. Nikl and A. Yoshikawa, Radiat. Meas. in print (2019).
[3] S. Kodama, S. Kurosawa, A. Yamaji, J. Pejchal, R. Král, Y. Ohashi, K. Kamada, Y. Yokota, M. Nikl and A. Yoshikawa, J. Cryst. Growth. **492** (2018) 1.

BL3B

Photoluminescence upon Vacuum Ultraviolet Excitation in Pr^{3+} Ion Doped Alkaline–Earth Phosphates

Y. Inaguma[1], R. Horiguchi[1], S. Sasaki[1], M. Yaname[1], D. Mori[1], K. Ueda[1] and T. Katsumata[2]
[1]*Department of Chemistry, Facility of Science, Gakushuin University, Tokyo 171-8588, Japan*
[2]*Department of Chemistry, School of Science, Tokai University, Hiratsuka 259-1292, Japan*

Pr^{3+} ion doped inorganic materials have been extensively investigated in connection with various applications [1]: laser materials utilizing visible emission corresponding to $^3P_0 \rightarrow {}^3H_4$ and $^1D_2 \rightarrow {}^3H_4$ transitions(blue-green and red emission, respectively), or infrared emission from the $^1G_4$ state of Pr^{3+}, field emission display (FED) devices utilizing red $^1D_2$ emission, scintillators or tunable ultraviolet (UV) lasers utilizing UV emission from the 4f5d state. Since the emission color or energy in Pr^{3+} ion doped phosphors is closely related to the electronic structure of host materials, the choice of host materials is a matter of vital importance to control the emission color/energy [2].

Recently phosphor materials emitting UV light upon vacuum ultra violet (VUV) excitation are desired as the substitutes of mercury lamp due to the toxicity of mercury. Pr^{3+} ion doped compounds are candidates of the UV phosphors because the UV emission from the 4f5d state in Pr^{3+} can be expected. The UV emission from the 4f5d state would be observed if the band gap energy of the host material corresponds to the VUV region. We then chose Pr^{3+} ion doped alkaline-earth phosphates with the band gap energy in the VUV region and investigated their luminescence properties. In our previous report[3], we presented the results of UV photoluminescence upon VUV excitation of $Ca_3(PO_4)_2$:Pr. Herein, we report on the UV photoluminescence of Pr-doped alkaline–earth phosphates $A_3(PO_4)_2$:Pr(A = Sr, Ba) in addition to $Ca_3(PO_4)_2$:Pr.

The polycrystalline samples were synthesized by a solid state reaction. The mixture of starting materials: alkaline-earth carbonate ACO_3(A = Ca, Sr, Ba), $(NH_4)H_2PO_4$ and Pr nitrate solution were calcined at 1000 °C in air. The calcined powder was pressed into pellets and sintered at 1000-1200 °C in air. The phase identification for the samples was carried out by the laboratory powder X-ray diffraction (XRD) using a Rigaku RINT 2100 diffractometer or a PANalytical X'Pert3 Powder diffractometer with a Bragg Brentano geometry (CuKα radiation). The emission and excitation spectra were recorded in the beamlines BL3B and BL7B at the UVSOR facility.

Figure 1 displays the emission(right side) and excitation(left side) spectra for $A_3(PO_4)_2$:Pr5%(A = Ca, Sr, Ba) at room temperature. As seen in Fig.1, the UV emission peaks corresponding to the transitions from the 4f5d state to the $4f^2$ (^3H_J, ^3F_J) states of Pr^{3+} were observed. In the excitation spectra, the peaks in the range of 150-220 nm were observed. The shorter and longer wavelength regions correspond to the host absorption band, *i.e.* the intra charge transfer of PO_4^{3-} [4] and the transition from the ground state of $4f^2(^3H_4)$ to the 4f5d state of Pr^{3+}, respectively. The emission and excitation peaks for $A_3(PO_4)_2$:Pr(A = Sr, Ba) appears at the shorter wavelength than those for $Ca_3(PO_4)_2$:Pr, which is attributable to the difference in covalency of Pr-O bonding.

Consequently, we found that $A_3(PO_4)_2$:Pr(A = Sr, Ba) as well as $Ca_3(PO_4)_2$:Pr exhibits the UV emission corresponding to the transition from the 4f5d state of Pr^{3+} upon the VUV excitation and the Pr^{3+} ion doped alkaline–earth phosphates are candidates of UV phosphors.

The authors thank Mr. M. Hasumoto, Mr. T. Yano for their experimental supports.

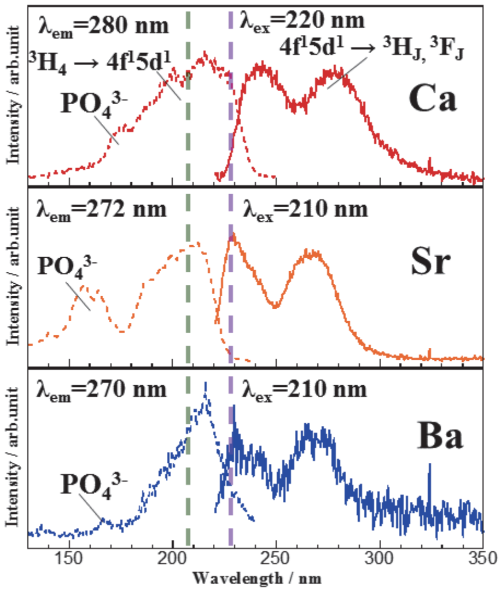

Fig. 1. Emission spectra (right side) and excitation spectra emission (left side) for $A_3(PO_4)_2$:Pr5% (A = Ca, Sr, Ba) at room temperature.

[1] E. Van der Kolk *et al.*, Phys. Rev. B. **64** (2001) 195129.
[2] Y. Inaguma *et al.*, Inorg. Chem. **50** (2011) 5389.
[3] Y. Inaguma *et al.*, UVSOR activity report 2011 **39** (2012) 129.
[4] H. Liang *et al.*, J. Solid State Chem. **177** (2004) 901.

BL3B

Emission Spectra of Pr-doped $BaZrO_3$

M. Yoshino, J. Sugiyama, T. Kuyama and S. Watanabe
Graduate School of Engineering, Nagoya University, Nagoya 464-8603, Japan

In this study, the excitation spectra and emission spectra of Pr^{3+} in $BaZrO_3$ crystal have been measured and changes in the spectra with doping of Yttrium and hydration are examined. The samples are synthesized by solid state reactions followed by annealing in N_2-H_2 atmosphere in order to reduce Pr^{4+} to Pr^{3+}. The oxygen vacancies are created in Y-doped $BaZrO_3$ and protons are incorporated by hydration of the vacancies. The concentration of Pr is 0.5 mol% and that of Y are 5 mol% and 15 mol%. The Y-doped samples are hydrated at 523 K in humidified N_2.

The emission spectra of $BaZrO_3$:Pr and $BaZrO_3$ host at 265 nm excitation are shown in Fig. 1. The sharp peaks of $BaZrO_3$:Pr around 500 nm and 600-650 nm originate from 4*f*-4*f* transitions of Pr^{3+}. Since the broad emission peaks around 350-550 nm appear in both $BaZrO_3$:Pr and $BaZrO_3$ samples, these originate from electron transitions in host rather than from 4*f*-5*d* transitions of Pr^{3+}. The emission spectra of $BaZrO_3$:Pr and Y-doped $BaZrO_3$:Pr shown in Fig. 2. The intensities of Pr^{3+} emissions increase with 5 mol% doping of Y, but they do not increase monotonically and become smaller in 15 mol%. It is supposed that Y substituted for Zr and oxygen vacancy promote the radiative transition in Pr^{3+} by decreasing the site symmetry of the Pr^{3+}, but oxygen vacancy prevent the transition with creation of defect level in the bandgap in high doping concentration. The excitation spectrum of Y15mol%-doped samples monitored at 490 nm and 616 nm are shown in Fig. 3 and Fig. 4. It is found that the changes in the emission intensity with hydration around 265 nm excitation is larger in 490 nm than in 616 nm as is the case in the change with increasing Y concentration in Fig. 2. The intensities around 220-250 nm decrease in both 490 nm and 616 nm. These two characteristic changes may be due to the defect levels of oxygen vacancy and hydrogen, respectively.

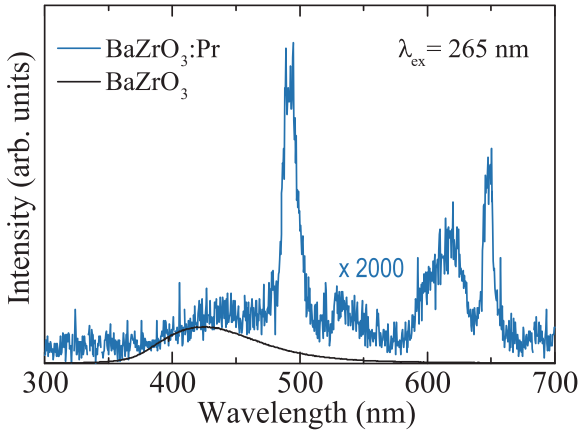

Fig. 1. Emission spectra of $BaZrO_3$:Pr and $BaZrO_3$. (λ_{ex}= 265 nm).

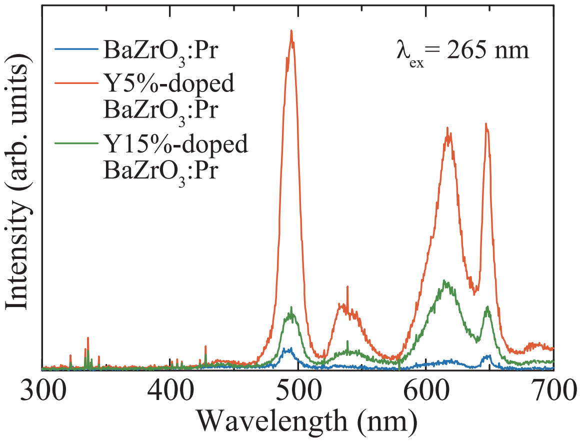

Fig. 2. Emission spectra of $BaZrO_3$:Pr and Y-doped $BaZrO_3$:Pr. (λ_{ex}= 265 nm).

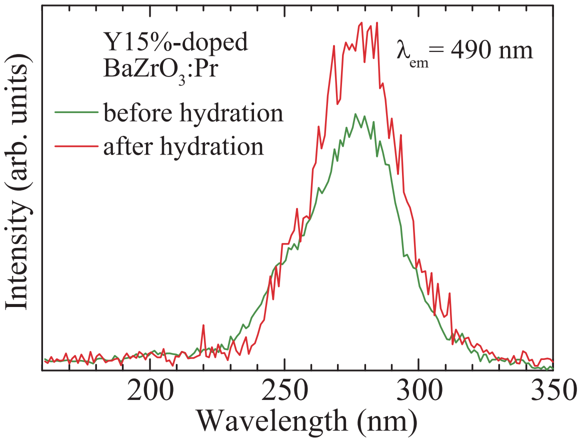

Fig. 3. Change in excitation spectra of Y-doped $BaZrO_3$:Pr with hydration. (λ_{em}= 490 nm).

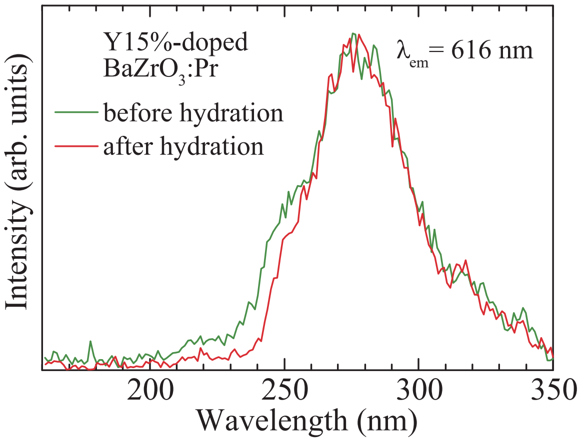

Fig. 4. Change in excitation spectra of Y-doped $BaZrO_3$:Pr with hydration. (λ_{em}= 616 nm).

BL3B

Temperature Dependence of Dielectric Function in Widegap Oxide Epilayer

T. Makino, T. Takeuchi and T. Asai
Deepartment of Electrical and Electronics Engineering, University of Fukui, Fukui 910-8585, Japan

Oxide-based strongly electron correlated materials are important from both fundamental and applied perspectives, due to their potential in the optoelectronic and electronic devices.

A detailed understanding of the bulk and surface optical properties of these materials is essential in order to make the best selection. However, in spite of its significance, very little work has been done on the optical properties of oxide-based strongly electron correlated materials, especially in the case of rare-earth compounds [1].

ε-Ga_2O_3 has various advantages as a wide band-gap semiconductor, and it is expected to be applied to power devices such as high frequency devices by taking advantage of this. In this way, it is essential for the detailed understanding of the bulk and surface optical properties of this material for the best choice. In recent years, its crystal symmetry has been identified; therefore little has been reported on the optical properties of ε-Ga_2O_3 at present. In this research, we aim to elucidate the interaction between electrons and phonons in ε-Ga_2O_3 and report on the temperature dependence of its dielectric function.

Figure 1 shows temperature dependence of the dielectric functions taken for Ga_2O_3 thin film. Only the real part is shown. The situation in the case of double layer (thin films grown on substrates) becomes very complicated. In case of bulk crystals free from their substrates, the conversion is rather simple. Although both the transmissivity and reflectivity can be analytically represented by using Fresnel's effective coefficient method with dielectric functions and thickness of the thin film, the dielectric functions cannot be represented with transmissivity and reflectivity. In our case, some model dielectric functions were adopted for this purpose.

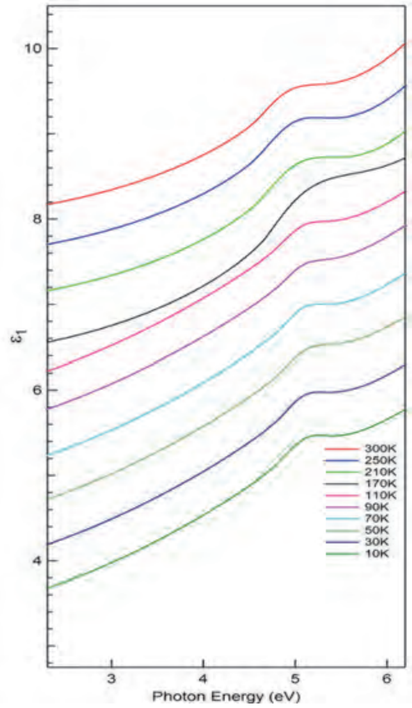

Fig. 1. Temperature dependence of real parts of dielectric function for ε-Ga_2O_3 thin film.

[1] R. Roy, V. G. Hill, E. F. Osborn, J. Am. Chem. Soc. **74** (1952) 719.
[2] H. Playford *et al.*, Chem. Eur. J. **19** (2013) 2803.
[3] F. Mezzadri *et al.*, Inorgan. Chem. **55** (2016) 12079.
[4] H. Nishinaka *et al.*, Jpn. J. Appl. Phys. **55** (2016) 1202BC.
[5] T. Uchida *et al.*, Appl. Phys. Express **7** (2014) 021303.
[6] J. C. Lu *et al.*, J. Cryst. Growth **299** (2007) 1.
[7] Y. P. Varshni, Physica (Utrecht) **34** (1967) 149.
[8] H. Qi *et al.*, J. Quant. Spectros. Rad. Transfer **112** (2011) 2507.
[9] M. A. Ordal *et al.*, Appl. Opt. **22** (1983) 1099.

BL3B

Appearance of the Luminescence Band due to Ag$^-$ Centers by VUV Irradiation at Room Temperature in Co-doped NaCl:I$^-$,Ag$^+$ Crystals

T. Kawai and O. Yagi
Graduate School of Science, Osaka Prefecture University, Sakai 599-8531, Japan

Since silver (Ag) atoms are normally present as cation impurities in ionic crystals, Ag$^-$ centers are not naturally existed in alkali halide crystals. The Ag$^-$ centers in alkali halides are created by the electrolytic coloration, additive coloration, and/or X- and γ-ray irradiation [1, 2]. In general, the Ag$^-$ centers are not created by irradiation of light in the vacuum ultra violet (VUV) region. We found that the irradiation of a VUV light on co-doped NaCl:I$^-$,Ag$^+$ crystals leads to the appearance of the A' luminescence due to the Ag$^-$ centers through the experiment with the BL3B beam line.

Figure 1 shows the typical luminescence and absorption spectra of NaCl:Ag$^-$ and NaCl:I$^-$,Ag$^+$ crystals at room temperature (RT). The A' luminescence and the C absorption bands due to the Ag$^-$ center in NaCl:Ag$^-$ are observed at 2.81 and 4.46 eV, respectively. In co-doped NaCl:I$^-$,Ag$^+$ crystals, the absorption and luminescence bands are observed at 6.78 and 5.02 eV, respectively. The absorption and luminescence bands due to the I$^-$ center are located at the same energy positions as those due to the Ag$^+$ center [2, 3]. Thus, the absorption and luminescence bands observed in the co-doped NaCl:I$^-$,Ag$^+$ crystals consist of the sum of both bands due to respective impurity centers.

Figure 2 shows the appearance and enhancement of the A' luminescence band obtained under excitation at 4.5 eV by prolonged irradiation of 6.74 eV light at RT. The 6.74 eV light corresponds to the absorption bands due to the I$^-$ and Ag$^+$ centers. The enhancement of the A' luminescence intensity is plotted as a function of irradiation time of VUV light at 6.74 eV in the insert of Fig. 2.

The appearance and enhancement of the A' luminescence imply that the Ag$^-$ centers are created by the irradiation of VUV light at 6.74 eV; that is to say, the conversion from the Ag$^+$ to Ag$^-$ ions occurs in NaCl host lattice at RT. When the VUV light corresponding to the absorption band due to the Ag$^+$ centers is irradiated to single-doped NaCl:Ag$^+$ crystals, the A' luminescence does not appear. Thus, the appearance of the A' luminescence in the co-doped NaCl:I$^-$,Ag$^+$ crystals would be related with the existence of the I$^-$ center band.

In our recent study [4], the photoexcitation on the I$^-$ center band at RT induces the creation of the electrons and the V$_K$ centers in NaCl host crystals. The electrons and the V$_K$ centers migrate through the host lattice at RT and are trapped at impurity centers. Though the detailed mechanism is unknown, the electrons and the V$_K$ centers created under photo-excitation at the I$^-$ center would play an important role on the conversion from the Ag$^+$ to Ag$^-$ ions. Such valence change processes might lead to the potential for producing the uncommon anions such as Au$^-$ and Pt^{2-}.

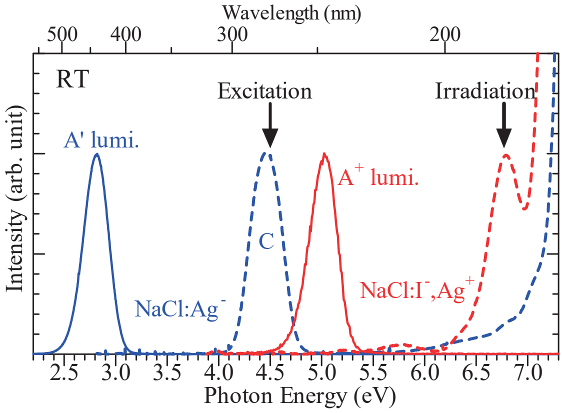

Fig. 1. Typical luminescence (solid curves) and absorption (broken curves) spectra of NaCl:Ag$^-$ (blue) and NaCl:I$^-$,Ag$^+$ (red) crystals at RT.

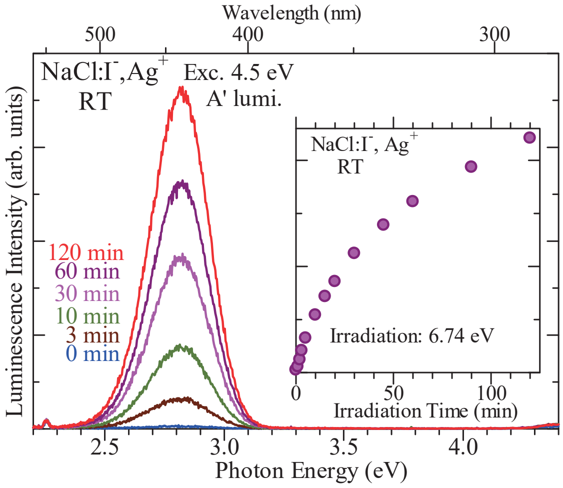

Fig. 2. Appearance and enhancement of the A' luminescence in NaCl:I$^-$,Ag$^+$ by prolonged irradiation of 6.74 eV light at RT.

[1] K. Kojima *et al.*, J. Phys. Soc. Jpn. **28** (1970) 1227.
[2] T. Kawai *et al.*, Opt. Mater. **77** (2018) 30.
[3] I. Akimoto *et al.*, Phys. Status Solidi C **6** (2009) 342.
[4] T. Kawai and A. Iguchi, J. Lumin. **207** (2019) 58.

BL3B

Optical Properties of Tl^+-doped $CsCaCl_3$ Single Crystals

K. Kubota and T. Kawai

Graduate School of Science, Osaka Prefecture University, Sakai 599-8531, Japan

Though optical properties of alkali halide crystals doped with metal ions of ns^2 electron configuration such as Tl^+, In^+, and Ag^- have been studied for a long time, there have been few reports on the ns^2 centers in other crystals [1]. In this study, we focused on Tl^+ centers in ternary compound $CsCaCl_3$. The $CsCaCl_3$ crystals attract attention as a host crystal for scintillator materials and the optical properties of the $CsCaCl_3$ crystals doped with various kind of impurity ions have been investigated [2]. However, the optical properties of the $CsCaCl_3$ crystal doped with ns^2 ions are considerably less studied. Thus, we have investigated the optical properties of the $CsCaCl_3$ crystals doped with the Tl^+ ions.

$CsCaCl_3$:Tl^+ crystals were grown by the Bridgman method from CsCl, $CaCl_2$ and TlCl powders. The optical measurements were performed at various temperatures from 8 K to 300 K at the BL3B line of UVSOR.

The absorption spectrum of a $CsCaCl_3$:Tl^+ crystal at 8 K is shown in Fig. 1. The A, B, and C absorption bands due to the Tl^+ ion were observed around 5.6, 6.7, and 7.1 eV, respectively. These absorption bands are attributed to the intra-ionic transitions from the ground $^1S_0$ state to the excited $^3P_1$, $^3P_2$, and $^1P_1$ states in the Tl^+ ion. The intensity ratio among the A, B, and C absorption bands in $CsCaCl_3$:Tl^+ is similar to that of the Tl^+ centers in alkali halide crystals, while these energy positions are located at the higher energy region than that of the Tl^+ centers in alkali chloride crystals. The difference of the energy positions might come from that of the lattice arrangement around the Tl^+ ion between $CsCaCl_3$ and alkali halide crystals.

Figure 2 shows the temperature change of the A absorption band between 8 K and 300 K. As the temperature rises, the bandshape of the A absorption band broadens and the peak position shifts to the higher energy side up to around 150 K. On the other hand, above 150 K, the peak position shifts to the low energy side. The change of the shift of the peak energy would come from a slight change of the lattice arrangement related with the tetragonal to cubic phase transition in $CsCaCl_3$.

Figure 3 shows the temperature dependence of the half-width of the A absorption band. The temperature dependence of the half-width can be fitted by the following theoretical formula considering the electron lattice interaction,

$$H(T) = H(0)\sqrt{\coth\left(h\nu/_{2k_BT}\right)},$$

where $H(0)$ and $h\nu$ are the half-width at 0 K and the effective phonon energy, respectively. From the fitting result, the values of 0.17 eV and 29.7 meV were obtained as $H(0)$ and $h\nu$, respectively.

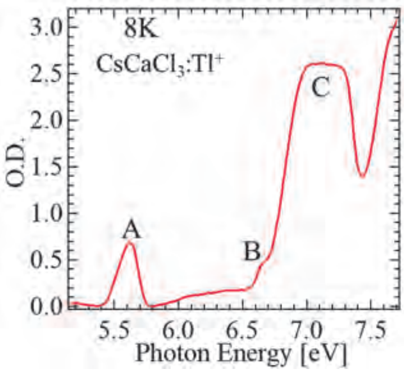

Fig. 1. Absorption spectrum of $CsCaCl_3$:Tl^+ at 8 K.

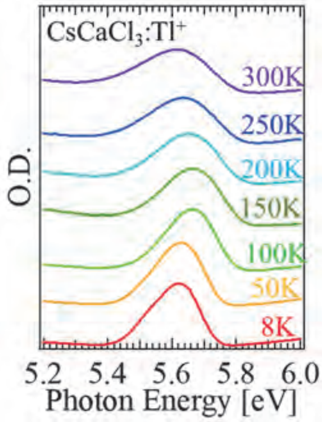

Fig. 2. Temperature change of the A absorption band in the $CsCaCl_3$ crystal at 8 K-300 K.

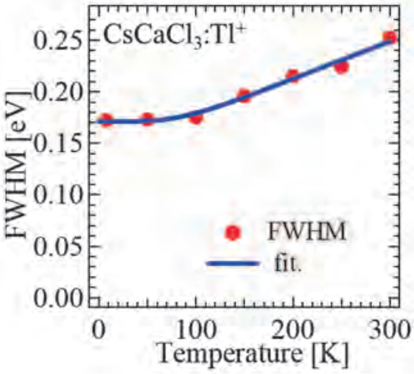

Fig. 3. Temperature dependence of the half-width of the A absorption band in the $CsCaCl_3$ crystal.

[1] A. Ranfagni *et al*., Advance in Physics **32** (1983) 823.

[2] M. Tyagi *et al*., J. Appl. Phys. **113** (2013) 203504.

BL3B

UV-visible Spectroscopy of γ-Si_3N_4

L. Museur[1], E. Feldbach[2], A. Zerr[3], M. Kitaura[4] and A. Kanaev[3]
[1]Laboratoire de Physique des Lasers, CNRS, Université Paris 13, 93430 Villetaneuse, France
[2]Institute of Physics, University of Tartu, 1 W. Ostwald str., 50411, Tartu, Estonia
[3]Laboratoire des Sciences des Procédés et des Matériaux, CNRS, Université Paris 13, 93430 Villetaneuse, France
[4]Faculty of Science, Yamagata University, Yamagata 990-8560, Japan

Compounds having spinel structure have been predicted to exhibit a very high tolerance to irradiation with fast neutrons resulting in low swelling even at high doses [1]. In this connection, the understanding of their electronic band structure and defects induced by ionized radiation is of paramount importance for the development of novel optical materials stable in the environments of a fusion reactor. We performed the study of a polycrystalline γ-Si_3N_4 with spinel structure by means of photoluminescence (PL) spectroscopy.

The sample of γ-Si_3N_4 was synthesized according to the earlier reported procedure [2]. The starting powder of α-Si_3N_4 with oxygen content <2 wt.%, compacted into a Pt capsule, was compressed to 14 GPa and heated to 1700 ºC for ~30 minutes. The sample irradiation with He-ions of total dose 10^{17} cm^{-2} was performed in the Ion Beam Lab of Helsinki University. The PL experiments were carried out at the BL3B beamline of UVSOR facility with synchrotron-radiation (SR) excitation in the UV-visible spectral range. The samples were mounted on a LHe flow-type cryostat, which permitted stabilizing the sample temperature in the range between 300 and 8K. The vacuum in the samples chamber was $\sim 3\cdot 10^{-7}$ Pa. The measured spectra were corrected for the detector sensitivity and optical line transmission.

The PL and PL-excitation (PLE) spectra of the pristine and irradiated γ-Si_3N_4 are respectively shown in Fig. 1 and Fig. 2. According to Museur et al. [3], the dominant PL band in Fig. 1a excited with photons of energy above band gap E_g=5.05 eV belongs (in Kröger-Vink notation) to $X^*Si^X_{Si}$ exciton bound to neutral defects. No significant PL of excited metastable paramagnetic nitrogen anion radical at 450 nm was observed. The absence of the self-trapped exciton emission at 312 nm (4.0 eV) may be explained by a structural quenching. After He^+ irradiation and excitation with photons of energy $h\nu \geq E_g$, The PL strongly weakened and exhibited red shift indicating structural modifications; simultaneously, a new near-IR PL band appeared at ~700 nm. In contrast, no modification was observed for the PL spectra excited with $h\nu < E_g$. The PLE spectra of the bound exciton (Fig. 2) evidenced red shift after the He^+ irradiation. Moreover, interband transitions above 5.05 eV (λ<250 nm) did not appreciably contribute to PL and a new band with the maximum at 530 nm was intensified with the lower-energy excitation. Apparently, the related radiation-induced structural defects have different origins. The excitonic origin may be proposed for the near-IR PL, which has no allowed sub-band gap transitions. The shifted visible PL band apparently belongs to modified structural defects Si^X_{Si}.

This work has been carried out within the framework of the EUROfusion Consortium and French Research Federation for Fusion Studies and has received funding from the Euratom research and training programme 2014–2018 under grant agreement No. 633053. The views and opinions expressed herein do not necessarily reflect those of the European Commission.

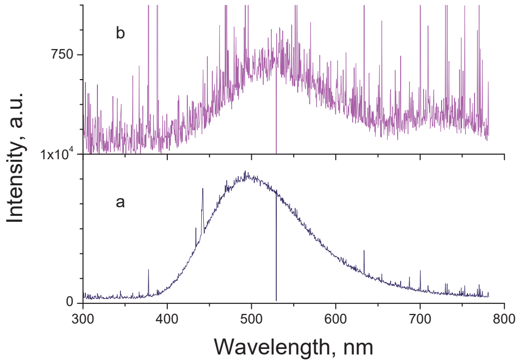

Fig. 1. PL spectra of fresh (a) and irradiated (b) γ-Si_3N_4 excited at 230 nm.

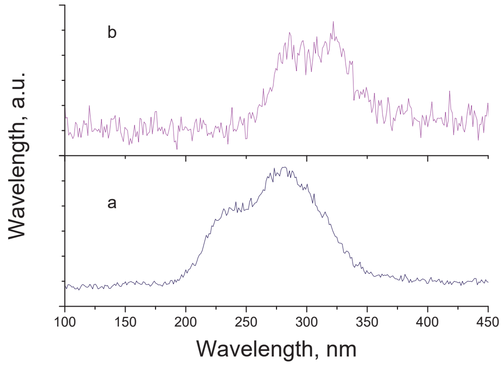

Fig. 2. Excitation spectra of PL at 500 nm of fresh (a) and irradiated (b) γ-Si_3N_4.

[1] K. E. Sickafus *et al.*, Science **289** (2000) 748.
[2] N. Nishiyama *et al.*, Sci. Rep. **7** (2017) 44755.
[3] L. Museur *et al.*, Sci. Rep. **6** (2016) 18523.

BL3B

UV-visible Spectroscopy of $MgAl_2O_4$ Spinel Single Crystal

L. Museur[1], E. Feldbach[2], M. Kitaura[3] and A. Kanaev[4]
[1]*Laboratoire de Physique des Lasers, CNRS, Université Paris 13, 93430 Villetaneuse, France*
[2]*Institute of Physics, University of Tartu, 1 W. Ostwald str., 50411, Tartu, Estonia*
[3]*Faculty of Science, Yamagata University, Yamagata 990-8560, Japan*
[4]*Laboratoire des Sciences des Procédés et des Matériaux, CNRS, Université Paris 13, 93430 Villetaneuse, France*

Spinel or $MgAl_2O_4$ is well known material, which electronic band and defect structures are not yet understood. In the same time, this material has a strong practical interest because of the predicted high tolerance to ionized radiation [1]. The knowledge of its electronic and optical properties in connection with radiation-induced defects will help to develop novel optical materials for extreme environments. In this study, we performed the spectroscopic analysis of $MgAl_2O_4$ single crystals by means of energy resolved photoluminescence (PL) spectroscopy.

The experiments were carried out at the BL3B beamline [2] of UVSOR facility with synchrotron radiation (SR) excitation in the UV-visible spectral range. The samples were mounted on the cold finger of a LHe flow type cryostat, which permitted stabilizing the sample temperature in the range between 300 and 8K. The vacuum in the samples chamber was ~$3\cdot10^{-7}$ Pa. In the complement to PL and PL-excitation (PLE) spectra, transmission and reflection spectra were recorded. The measured spectra were corrected on the detector sensitivity and optical line transmission. The single crystal (S1) from Alineason was (100) oriented and both sides polished of size 5x5x0.5 mm^3. Another crystal (S2) with (100) oriented surface, was available from the Tartu group. The irradiation of the spinels with He^+ ions of total dose 10^{17} cm^{-2} was performed in the Accelerator Lab of Helsinki University.

The PL spectra of the pristine crystals S1 and S2 are quite similar. The most long-wavelength structured near-IR emission at ~700 nm (1.8 eV) belongs to the well-known R-lines of Cr^{3+} impurity. According to previous interpretations, the strongest PL band at 5.4 eV belongs to the recombination of conduction-band electrons with holes captured at the nearby oxygen ions (e/h), and bands at 3.8 eV and 3.0 eV were respectively assigned to F (two electrons trapped at an oxide-ion vacancy) and F^+ (one electron trapped at an oxide-ion vacancy) centers (see in [3]). The PLE spectra of different PL bands for pristine samples are shown in Fig. 1. All PL bands (except for that of Cr^{3+} impurity) show up upon the band gap excitation, which energy $E_g \approx 8.3$ eV can be suggested. The He^+ irradiation weakened PL and strongly modified PLE spectra of all bands, except for that of Cr^{3+} impurity (Fig. 2). In particular, the interband transitions do not significantly contribute to these spectra and the intraband transitions shift to longer wavelengths. The common excitation band of e/h, F and F^+ emissions at 7.2 eV may be connected to antisite defects. The work is in progress to interpret radiation-induced damage of the spinel structure.

This work has been carried out within the framework of the EUROfusion Consortium and French Research Federation for Fusion Studies and has received funding from the Euratom research and training programme 2014–2018 under grant agreement No. 633053. The views and opinions expressed herein do not necessarily reflect those of the European Commission.

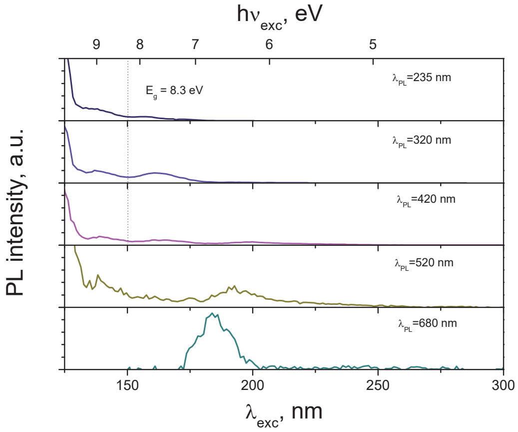

Fig. 1. PLE spectra of S1 crystal (T=8 K).

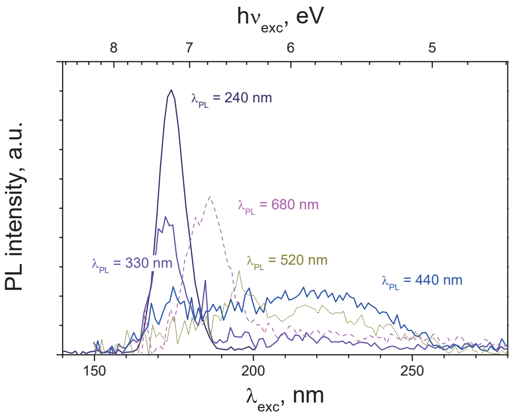

Fig. 2. PLE spectra of irradiated S2 crystal (T=8 K).

[1] K. E. Sickafus *et al.*, Science **289** (2000) 748.
[2] M. Kitaura *et al.*, J. Lum. **172** (2016) 243.
[3] A. Pille *et al.*, Ceram. Int. **45** (2019) 8305.

BL3B

Construction of Vacuum Referred Binding Energy Diagram of $YSiO_2N$ Doped with Lanthanoid Ions for Persistent Luminescence

Y. Kitagawa, J. Ueda and S. Tanabe
Graduate School of Human and Environment Studies, Kyoto University, Kyoto 606-8501, Japan

Lanthanoid ions doped in inorganic materials form localized energy levels in the host bandgap. The relative positions of these levels play a very important role for the carrier trapping process of persistent luminescence. From the view point of developing novel persistent phosphors, it is necessary to investigate the electronic structure of $Ln^{3+/2+}$-doped compounds. Dorenbos proposed the method to construct the vacuum referred binding energy (VRBE) diagram of $Ln^{3+/2+}$ in compounds based on spectroscopy [1,2]. In this work, the VRBE diagram of $YSiO_2N$, which has characteristic Y^{3+} sites coordinated by six oxide and two nitride ions [3], was constructed. Since Ce^{3+} ions in oxynitrides show 5*d*-4*f* luminescence with low energy because of the stronger nephelauxetic effect by N^{3-} than O^{2-} [4], oxynitrides activated with Ce^{3+} have the potential to be a characteristic persistent phosphor with longer luminescent wavelength. To obtain some parameters for construction of the VRBE diagram, photoluminescence excitation (PLE) spectra of Ce^{3+}- or Eu^{3+}-doped $YSiO_2N$ samples were measured at UVSOR BL3B.

Figure 1 shows the PLE spectra of Ce^{3+}- or Eu^{3+}-doped $YSiO_2N$ samples. In both spectra, a small band was observed at around 210 nm. This band is assigned to the host exciton creation band. Considering the binding energy between an electron and a hole, the optical bandgap of $YSiO_2N$ was estimated to be 6.34 eV, which is smaller than that of pure oxide materials with the same Y/Si ratio. This is because for oxynitride compounds, energy of the valence band top increases due to N 2*p* orbitals. For the $YSiO_2N:Ce^{3+}$ sample, several overlapped excitation bands, which are derived from the 4*f*-5*d* transition of Ce^{3+}, were observed at around 260 nm ($4f$-$5d_{4,5}$) and around 360 nm ($4f$-$5d_{1,2,3}$). In the case of the $YSiO_2N:Eu^{3+}$ sample, another broad excitation band was observed in the range of 250-350 nm. This band is attributed to the charge transfer (CT) transition from the coordinating anions to Eu^{3+} ions. Although for many Eu^{3+}-activated oxides the CT band is located at around 250 nm, the CT band of the Eu^{3+}-activated oxynitride sample has lower energy. Therefore, this band is due to the CT transition from not O^{2-} but N^{3-} to Eu^{3+}.

Based on the measured spectroscopic data, the VRBE diagram of $YSiO_2N$ was constructed and shown in Fig. 2. E_C and E_V mean the bottom of the conduction band and the top of the valence band, respectively. The red and blue zigzag curves indicate the ground level of divalent and trivalent lanthanoid ions, respectively. Lanthanoid ions with energy levels below E_C have the potential to be an electron trap. For $YSiO_2N:Ce^{3+}$, Sm^{3+} and Tm^{3+} is predicted to be the suitable co-dopant ions for persistent luminescence at room temperature because they have appropriate activation energy, the difference between E_C and levels of divalent lanthanoid ions.

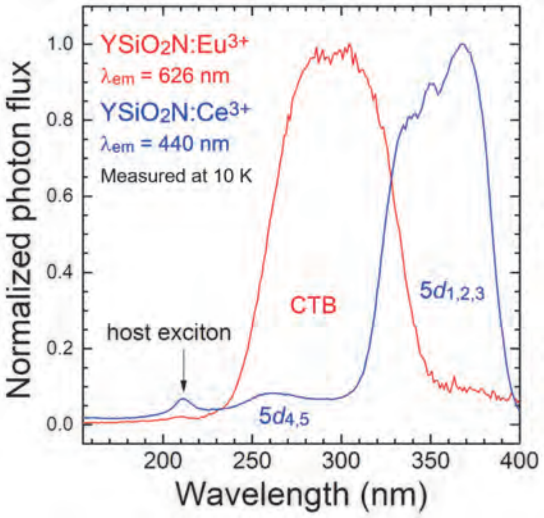

Fig. 1. PLE spectra of $YSiO_2N$ samples doped with Ln^{3+} (Ln = Ce or Eu). Both spectra were measured at 10 K.

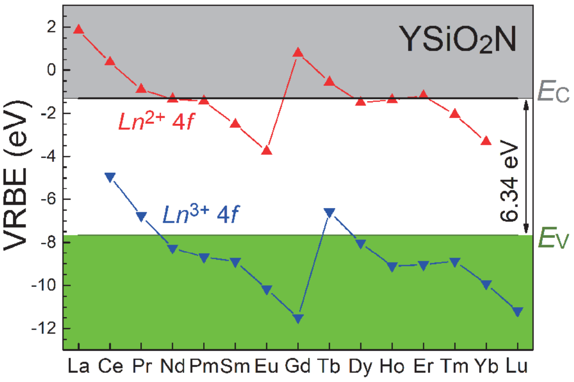

Fig. 2. The constructed VRBE diagram of $YSiO_2N$.

[1] P. Dorenbos, Phys. Rev. B **85** (2012) 1.
[2] P. Dorenbos, J. Solid State Sci. Technol. **2** (2012) R3001.
[3] L. Ouyang *et al.*, Phys. Rev. B **69** (2004) 094112.
[4] J. W. H. van Krevel *et al.*, J. Alloys Compd. **268** (1998) 272.

BL4U

STXM Study of Nanowire Cathode Materials for Li-Ion Batteries

D. Asakura[1, 2], K. Akada[3], Y. Harada[2,3,4], H. Yuzawa[5], T. Ohigashi[5] and E. Hosono[1,2]
[1] *Research Institute for Energy Conservation, National Institute of Advanced Industrial Science and Technology (AIST), Tsukuba 305-8568, Japan*
[2] *AIST-UTokyo Advanced Operando-Measurement Technology Open Innovation Laboratory (OPERANDO-OIL), AIST, Kashiwa 277-8565, Japan*
[3] *Institute for Solid State Physics, The University of Tokyo, Kashiwa 277-8581, Japan*
[4] *Synchrotron Radiation Research Organization, The University of Tokyo, Sayo 679-5148, Japan*
[5] *UVSOR Synchrotron Facility, Institute for Molecular Science, Okazaki 444-8585, Japan*

Li-ion battery (LIB) is a key energy-storage device to realize a low-carbon society. Particularly, for electric vehicles, LIBs with high energy density and high power density are necessary. To develop such high-performance LIBs, improving the performances of the cathodes and designing novel cathode materials are inevitable.

Nanowire materials are promising to enhance the rate performance because of the short Li-diffusion path, which should contribute to the power density of LIB. For nanowire cathode materials, it is important to investigate how the Li diffusion proceeds in the nanowire and to visualize the distribution of electronic structure upon the charge/discharge. Thus, X-ray microscopy should be powerful to clarify those issues. In this study, we demonstrate *ex situ* scanning transmission X-ray microscopy (STXM) for $LiMn_2O_4$ (LMO) nanowire.

The LMO nanowire made by our group [1] was mixed with carbon additive and a binder. The slurry was dropped on Au(5 nm)/Ti(5 nm)/Si_3N_4(150 nm) membrane window and dried. The thickness of the coated film was thin enough to transmit soft X-rays. This film as a working electrode was assembled as a three-electrode cell with Pt counter electrode, Ag/AgCl reference electrode and 1 M $LiNO_3/H_2O$ electrolyte solution. Cyclic voltammetry experiments with a scan speed of 0.5 mV/s were performed before the soft X-ray measurements. The voltage range was set to 0.01 V (vs. Ag/AgCl) and 1.0 V. *Ex situ* Mn $L_{2,3}$-edge X-ray absorption spectroscopy (XAS) and STXM were carried out for the initial and charged LMO samples at BL4U of UVSOR.

Figure 1(a) shows the Mn $L_{2,3}$-edge XAS for the total area of the charged LMO nanowire. The profile is almost attributed to a Mn^{4+} state according to a multiplet calculation. Figures 1(b-1) and 1(b-2) are the STXM images for the nanowire measured with the photon energies of A and B shown in Fig. 1(a). Figure 1(b-1) for which the Mn^{3+} character is enhanced are not uniform compared to Fig. 1(b-2). A difference between the optical density image of Fig. 1(b-1) and that of Fig. 1(b-2) is displayed in Fig. 1(c), showing inhomogeneous distribution of Mn^{3+} states remaining in the nanowire after partial and insufficient oxidation, which is hardly found by the XAS without imaging.

For the initial LMO, mixed Mn^{3+} and Mn^{4+} states were confirmed (not shown here). Thus, the utility of STXM to nanostructured electrode materials for LIBs is extremely high. In the near future, we will develop an *operando* STXM measurement system to monitor charge distribution dynamics during charge-discharge reaction of LIBs.

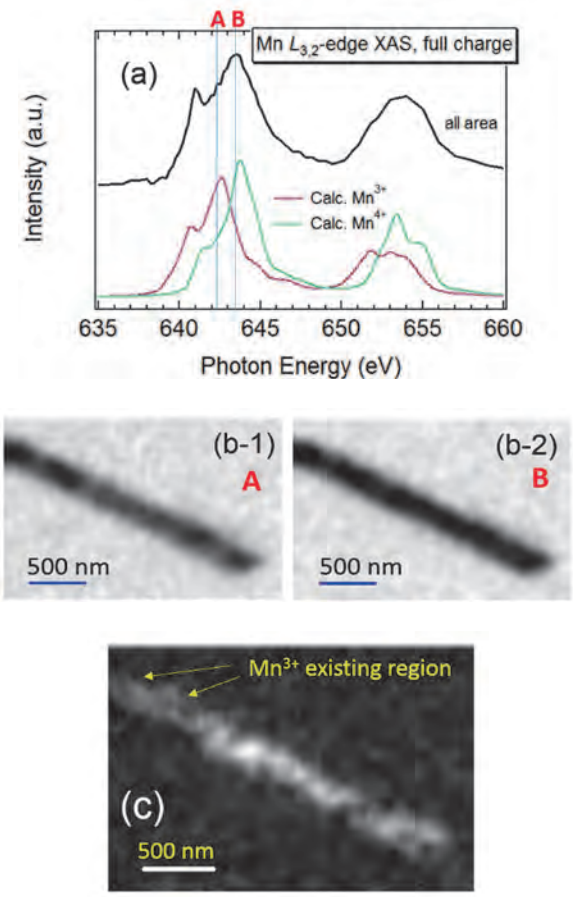

Fig. 1. (a) Mn $L_{2,3}$-edge transmission XAS for the whole are of a nanowire. Charge-transfer multiplet calculations for Mn^{3+} and Mn^{4+} are also shown [2]. (b-1) and (b-2) STXM images for the photon energies A and B in panel (a). (c) Difference between the optical density of (b-2) and that of (b-1).

[1] E. Hosono *et al.*, Nano Lett. **9** (2009) 1045.
[2] E. Stavitski and F. M. F. de Groot, Micron **41** (2010) 687.

BL4U

STXM Imaging of Water Surrounding Air Bubbles

Y. Harada[1,2], T. Ohdaira[1], K. Akada[1] and T. Ohigashi[3]
[1]*Institute for Solid State Physics, The University of Tokyo, Kashiwa 277-8581, Japan*
[2]*Synchrotron Radiation Research Organization, The University of Tokyo, Sayo 679-5148, Japan*
[3]*UVSOR Synchrotron Facility, Institute for Molecular Science, Okazaki 444-8585, Japan*

Hydrogen bond network of liquid water is spatiotemporally uniform on average, while the local and instantaneous coordination of individual water molecules is of course heterogeneous. Many discussions have been made on the nature of the microscopic heterogeneity. In the past 15 years we have studied liquid water using synchrotron soft X-rays aiming at an essential understanding of this heterogeneity and obtained a lot of experimental results which supported the existence of two characteristic moieties that constitute liquid water [1, 2].

When the subject is extended to solid-liquid, liquid-liquid and liquid-gas interfaces, we must consider a connection between the bulk water having heterogeneous hydrogen bond network and water at the solid-liquid, liquid-liquid and liquid-gas interfaces which we simply refer to as interfacial water [3]. In the case of micro/nano bubbles liquid-gas interface is formed, and the presence of interfacial water surrounding the micro/nano bubbles can be considered. However, the thickness and hydrogen bond network of the interfacial water has yet to be systematically explored. Moreover, the electrostatic charge around micro/nano bubbles and their stabilization mechanism are still under debate [4]. In this work, we performed chemical state imaging of water surrounding micro/nano bubbles using O K-edge X-ray absorption spectroscopy to elucidate the electronic state and network structure of water molecules forming the micro/nano bubbles by taking advantage of the experience cultivated in the analysis of bulk water.

Water sample filled up with plus charged nano bubbles with the maximum ζ-potential of +23 mV, the averaged diameter of 180 nm and the number density around 1 x 10^8 particles/ml were prepared, all estimated by using a ZetaView Particle Tracking Analyzer. A drop of the micro/nano bubble water was sandwiched in between two 150 nm-thick SiN membranes. During the limited beamtime we could find only micrometer sized bubbles due to better possibility to find them than 100 nm order nano bubbles. Prior to the O *K*-edge imaging we obtained N *K*-edge image to confirm that the particle is indeed an air bubble that has stronger N *K*-edge absorption inside than outside.

Figure 1 shows O *K*-edge STXM image of a micro bubble obtained at (a) 532.04 eV and (b) 536.44 eV excitations, respectively. At 532.04 eV, enhancement of the signal inside the micro bubble occurred by the resonance to the π* state of an O_2 gas (around 1 eV above the typical absorption peak). At 536.44 eV excitation which is close to the pre-edge resonance of liquid water (around 1.5 eV above the typical absorption peak), we found surrounding water has specific chemical state in a micrometer region from the bubble surface compared to the bulk region far from the bubble. The origin of the appearance of different chemical state of water is yet unknown. A possible explanation is that water in this region is under the electric dipole layer around the bubble and influenced by the interaction with the dipole moment of a water molecule, although the thickness of the dipole layer could be the micrometer size only in a ultrapure water, which is not expected in the present experimental protocol. An additional bright region was found in Fig. 1(b) indicated by the black arrow. This sphere was not observed in Fig. 1(a) and we believe this is due to radiation induced damage of the bubble interacting with both sides of the SiN membranes. In the near future we need to trace the cause of the occurrence of the additional structure and realize the imaging of real nanobubbles.

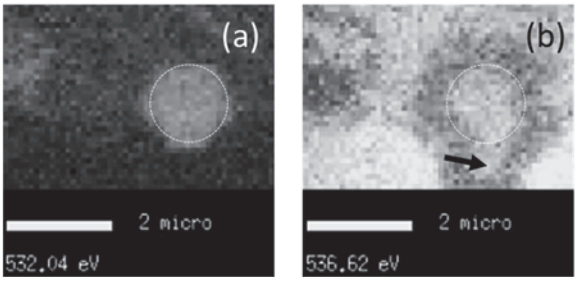

Fig. 1. O *K*-edge transmission XAS images of a microbubble obtained (a) at 532.04 eV excitation (around 1 eV above the π* state of typical O_2 gas) and (b) at 536.62 eV excitation (around 1.5 eV above the pre-edge resonance of typical liquid water) .

[1] T. Tokushima *et al.*, Chem. Phys. Lett. **460** (2008) 387.
[2] A. Nilsson and L. G. M. Pettersson, Nat. Commun. **6** (2015) 8998.
[3] K. Yamazoe *et al.*, Langmuir **33** (2017) 3954.
[4] M. Alheshibri, J. Qian, M. Jehannin, and V. S. J. Craig, Langmuir **32** (2016) 11086.

BL4U

STXM Studies on Vapor-assisted Quasi-2D Perovskite Solar Cells

H. W. Shiu[1], M. S. Li[2], L. C. Yu[1], Y. L. Lai[1], T. Ohigashi[3], N. Kosugi[3], P. Chen[2] and Y. J. Hsu[1]
[1]National Synchrotron Radiation Research Center, Hsinchu 300, Taiwan
2 Department of Photonics, National Cheng Kung University 701, Tainan, Taiwan
[3]Institute for Molecular Science, Okazaki 444-8585, Japan

Organic hybrid perovskite is one of the most attractive emerging photovoltaic devices due to its high optical absorption coefficient, long carrier diffusion lengths and low manufacturing costs. Although the power conversion efficiency (PCE) of 3D perovskite has been reported to reach a high record of 23 % for a small area device [1], how to improve the stability of organic hybrid perovskite in high humid condition is an important issue. Recent study indicated that a hybrid structured low dimensional perovskites formed by replacing the cation with large planar organic cation exhibits much more resistant to humidity than the 3D perovskite devices.

In order to investigate the device performance and electronic properties, we synthesized a bunch of dimensional tunable quasi-2D perovskite by mixing stoichiometric quantities of lead iodide (PbI_2) and PEAI ($C_8H_9NH_3$) to yield a series of compounds with different $PEAI/PbI_2$ ratio on mp-TiO_2/SiN substrate. With further treatment of vapor-assisted MAI (CH_3NH_3I), a series of compact crystalline layer of $(PEA)_2(MA)_{n-1}Pb_nI_{3n+1}$ were formed. As a results, a remarkable PCE of 19.1% has been successfully achieved with $PEAI/PbI_2$ = 0.05 (n = 40) which showed better performance than the pristine 3D perovskite of $MAPbI_3$ (PCE =17.31%) [2]. However, at high $PEAI/PbI_2$ ratio, for example $PEAI/PBI_2$ = 1 or 2, poor PCE of 5.85% and 0.02 % were observed. Besides, the SEM and KPFM results suggest that the grain size and surface potential of PEAI modified perovskite play an important role for the photovoltaic performance. In order to understand the qusai-2D materials in a microscopic point of view, we systematically studied the layer number dependent behavior of $(PEA)_2(MA)_{n-1}Pb_nI_{3n+1}$ perovskite by scanning transmission X-ray microscopy (STXM) and Near-edge X-ray absorption fine structure (NEXAFS).

Two different substrates with low and regular mp-TiO_2 concentration were prepared for study the interplay between PEAI modified-perovskite and mp-TiO_2. Herein, we mainly focus on the high $PEAI/PbI_2$ ratio perovskite on regular substrate to understand the correlation between PEAI and the $MAPbI_3$. Figure 1 shows the STXM carbon map of (a) $PEAI/PbI_2$ = 2 (n = 1) without MAI treatment and (b) $PEAI/PbI_2$ = 1 (n = 2) with MAI treatment. Only weak contrasts were observed in Fig. 1 (a), however there is no chemical difference between dark and bright regions after detail examined by NEXAFS (not show here). The results implied that for high $PEAI/PbI_2$ ratio, the hybrid perovskite performed morphologically and chemically uniform.

Figure 2 shows STXM carbon map and the corresponding micro-spectroscopy of $PEAI/PbI_2$ = 2 (n = 1) extracted from 3D images after MAI treatment. Compare with the result without MAI treatment (Fig.1 (a)), clear bubble like structures with nearly 5 µm size domain were observed. For pure $(PEA)_2PbI_4$ (n = 1), the characteristic carbon signal is C=C π* resonance at 285 eV, in contrast with pure $MAPbI_3$ (n = ∞), the characteristic signal is C-H and C-N σ* resonance at 288.5 and 290 eV. As shown in Fig. 2 (b), the shape of red and blue spectrum is similar, however the ratio of C=C π* to C-N σ*resonance exhibits opposite behavior between which indicated the phase separation behavior is presented in $PEAI/PbI_2$ mixtures. It is another evidence for the formation of multiphase qusi-2D perovskite with n = 1, 2 ,3 and else.

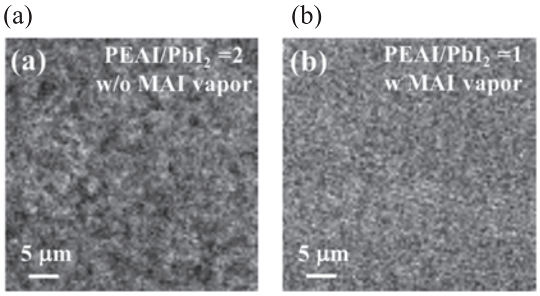

Fig. 1. STXM carbon map of (a) $PEAI/PbI_2$ = 2 without MAI vapor treatment and (b) $PEAI/PbI_2$ = 1 with MAI vapor treatment on mp-TiO_2/SiN substrate. The mapping are obtained by the imaging subtraction between 285 eV and the pre-edge.

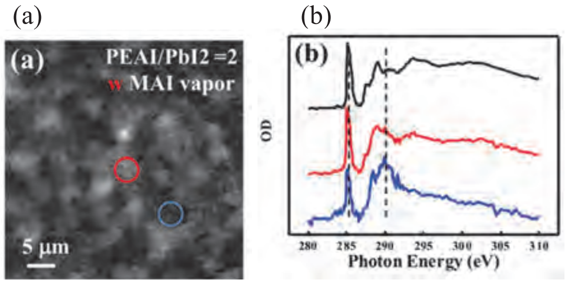

Fig. 2. (a) STXM carbon map of $PEAI/PbI_2$ = 2 with MAI vapor treatment and (b) the corresponding micro-spectrum before (dark line) and after (red and blue line) MAI treatment.

[1] Y. Rong, Y. Hu, A. Mei, H. Tan, M. I. Saidaminov, S. Seok, M. D. McGehee, E. H. Sargent and H. Han, Science **361** (2018) eaat8235.
[2] M.-H. Li, H.-H. Yeh, Y.-H. Chiang. U-S. Jeng, C.-J. Su, H.-W. Shiu, Y.-J. Hsu, N. Kosugi, T. Ohigashi, Y.-A. Chen, P.-S. Shen, P. Chen and T.-F. Guo, Adv. Mater. **30** (2018) 1801401.

BL4U

In Depth Qualitative Structural Analysis of Nanocellulose Hybrid Materials

M.Y. Ismail[1], M. Huttula[2], M. Patanen[2], H. Liimatainen[1], T. Ohigashi[3], H. Yuzawa[3] and N. Kosugi[3]
[1]*Fibre and Particle engineering unit, University of Oulu, P.O. Box 3000, 90014 University of Oulu, Finland*
[2]*Nano and Molecular Systems unit, University of Oulu, P.O. Box 3000, 90014 University of Oulu, Finland*
[3]*UVSOR Synchrotron Facility, Institute for Molecular Science, Okazaki 444-8585, Japan*

Hybrid materials are high strength and modulus materials that consist of an organic-inorganic blend. We have fabricated such kind of hybrid films using cellulose nanofibrils (CNF) and nanosilica (5 - 30% wt) embedded in a chitosan (Chi) biopolymer matrix using a slow evaporation method, and characterized various mechanical, chemical and structural aspects of these films [1]. The combination of these constituents can result in a sustainable packaging material with tailored characteristics such as microbial resistance with the help of chitosan, high strength and stiffness and biodegradability and with the aid of CNF and nanosilica. The inorganic filler plays a major role in the mechanical, thermal and UV absorption properties. The interaction between the constitutes is a key factor in affecting the hybrid's properties.

Microscale structural properties of hybrids are commonly investigated using field emission scanning electron microscopy (FESEM) and transmission electron microscopy. However, those techniques do not give the chemical distribution of the structure. Therefore, synchrotron radiation techniques are needed in order to complement the FESEM imaging. Scanning Transmission soft X-ray Microscopy (STXM) was used to investigate the spatial distribution of the chemical components of the studied hybrids, verifying the agglomerates of silica in the hybrid.

The STXM experiment was carried out at BL4U beamline at UVSOR. The imaging was performed at energies spanning over the C K-edge (280 and 320 eV) and Si $L_{2,3}$-edge (100 to 130 eV). The samples were "sandwiched" between resin blocks for ultramicrotome sectioning, a reference spectrum of resin was collected to ensure that the main material between the resin has not been affected by the embedding. The reference X-ray absorption spectra (XAS) at C K-edge of pure cellulose nanofibers and chitosan were recorded and matched with previous references [2].

Figure 1 shows examples of the obtained results for 10 wt% nanosilica hybrid film. Upper panels show examples how the spectral information of STXM can be used to differentiate the silica-rich regions from the CNF-chitosan film. The RGB images have been constructed using a "stack fit" procedure of aXis2000 software [3]. In short, the XAS (shown in Figs. 1 b & d) of indicated regions (shown with circles in Figs. 1 a & c) are extracted and they are fitted to each pixel of the image. The final color of a pixel depends on the weight of each RGB component spectra in that specific pixel. In Fig. 1 b, the red XAS is a resin spectrum, extracted from right lower corner of Fig. 1 a. The blue XAS resembles both cellulose and chitosan spectra. Green shows strong XAS with cellulose-type features. At Si $L_{2,3}$-edge (Figs. 1 c & d), the regions in red show a typical XAS for SiO_2 [4], whereas blue and green regions do not exhibit as strong resonance behavior. The optical density images are shown in the lower panels (Figs. 1 e and f) and corresponding average C K-edge XAS of the whole imaged region is shown in Fig. 1 g. Figures 1 e and f represent the sum stacks below the C K-edge (280-284 eV) and on the top of the C K-edge (288.2-300 eV). Figure 1 e shows strongly absorbing white band and spots, which effectively disappear on the top of the C K-edge resonance region (Fig. 1 f). Instead, thin (width <150 nm) lines are clearly highlighted. This indicates that the white regions below the C K-edge are SiO_2 agglomerates, whereas the thinner stripes showing up at the C K-edge are bundles of nanocellulose fibers aligned with the direction of cutting or wrinkles in the CNF-chitosan film.

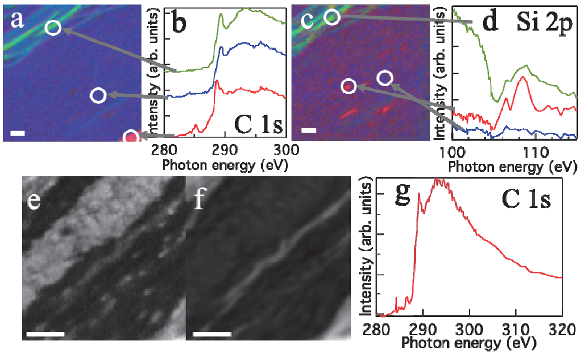

Fig. 1. Upper panels: RGB maps at a) C K-edge with b) corresponding XAS of indicated regions, and c) at Si $L_{2,3}$-edge with d) XAS of indicated regions. Lower panels: Optical density images e) below and f) on the top of the C K-edge, and g) the average XAS showing the energy regions used to construct images e and f (grey shadowed areas). Scale bar 1 µm.

[1] M. Y. Ismail *et al.*, submitted to Carbohydrate Polymers.
[2] C. Karunakaran *et al.*, PLOS ONE **10** (2015) e0122959.
[3] http://unicorn. mcmaster.ca/aXis2000.html
[4] D. Li *et al.*, Am. Miner. **70** (1994) 622.

BL4U

Chemical and Spatial Identification for Gas-Dependent Nanobubbles Sandwiched in Graphene Liquid Cells

C. H. Chuang[1], W. H. Hsu[2], I. S. Huang[2], W. F. Pong[1], T. Ohigashi[3] and N. Kosugi[3]
[1]*Department of Physics, Tamkang University, Tamsui 251, Taiwan*
[2]*Institude of Physics, Academia Sinica, Taipei 115, Taiwan*
[3]*UVSOR Synchrotron Facility, Institute for Molecular Science, Okazaki 444-8585, Japan*

Since 2004, graphene retains the crown among the most studied two-dimensional materials for numerous applications, not only due to the promising electric and thermal conductivity but also due to the true two-dimensionality of single layer graphene. The idea of replacing Si_3N_4 window by graphene in liquid cells is under development, which will provide in-situ conditions and real-time control [1]. X-ray source used in scanning transmission X-ray microscopy (STXM) can provide the X-ray absorption spectrum with the element-specific determination and chemical bonding information, even at the nanoscale resolution. Using the combined ability of X-ray spectral feature in STXM microscopes, in-situ detection is achieved in various investigation [2]. Although the use of graphene sheet as ultra-thin window has been proposed due to physical enhancement, it is rarely seen in the utilization in STXM owing to the limited knowledge in the solid-liquid interface and electrochemical ability. In the energy materials research, the catalytic activity on the external surface and active site is of prime importance which will provide space-resolved information.

In this work, we observed structure formed by gas molecules within the confinement of few-layers graphene sheets by STXM experiment which was carried out at the BL4U. The left inset in Fig. 1(a) shows the C 1*s* mapping image of graphene by STXM which revel an elliptical dark-shade region at the center, corresponding to gas-formed structure surrounded by multi-layer graphene. The transmission image through a variety of piece of graphene sheet demonstrates the variation in mapping intensity. The absorption intensity inside the elliptical shape at the center area is much higher than the signal of the graphene sheets, which is the characteristic of the cross-section absorption of gas region and was also identified as the gas-formed structure area by transmission electron microscopy (TEM) experiments prior to this experiment. Individual x-ray absorption spectrum (XAS) at the carbon near edge corresponding to the selected area are shown in Fig. 1(a). The C1*s* spectra collected from outside of the gas-formed structure exhibit a flat anisotropy of graphene layer, while it is strongly based on the incident polarization of X-ray beam and its directional dipole-transition selection rule. The inside area of elliptical gas-formed structure is divided into three areas and features owing to the spectral features around photon energy 284 ~ 287 eV. It is indicative of the interface bonding coordination and gas-filled contribution, and also the relative ratios of π^*/σ^* state at 285.5 and 291.7 eV are one of the spectral evidence as for the position dependence [3].

Figure 1(b) displays the N1*s* mapping image and relative XAS. At the corresponding area as Fig. 1(a), the graphene region outside the gas-formed structure has the low edge jump at the N K-edge absorption due to the unnoticed nitrogen content owing to the large-area signal integration. Relatively, the intensity of N *K*-edge absorption is verified for the higher absorption in the gas-formed region. The features at 398.9 and 400.5 eV are mostly assigned to pyridinic/pyrrolic N-related groups and $-C\equiv N$ triplet state [3]. Both the features reflect the evidence of nitrogen bonding configuration inside the structure, different from the outside surface absorption. Thus, our STXM result for graphene materials and its application show the interior phase of gas as for the combination and absorption. It provides valuable insights into the possible mechanism of gas absorption at the graphene interface as well as the observation of gas-condensed phase at solid-liquid interface [4].

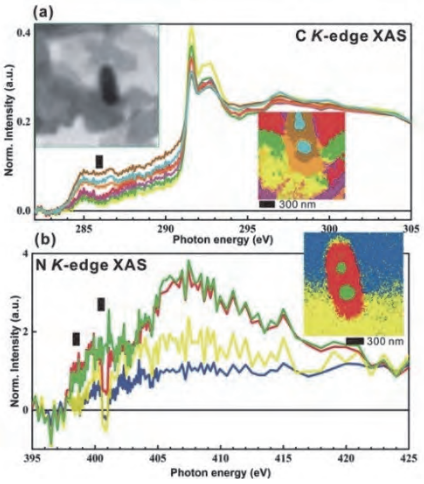

Fig. 1. (a) Individual XAS at carbon K-edge, selected from the STXM mapping image (inset). (b) XAS at N k-edge obtained from STXM mapping image (inset).

[1] S. Nemsak *et al.*, J. Am. Chem. Soc. **139** (2017) 18138.
[2] T. Ohigashi *et al.*, AIP Conference Proceedings **1741** (2016) 050002.
[3] C. H. Chuang *et al.*, Scientific Report **7** (2017) 42235.
[4] C.-K. Fang *et al.*, Scientific Reports **6** (2016) 24651.

BL4U

Effect of Defect on Perovskite Hydroxide for Oxygen Evolution Reaction

Y. R. Lu[1], C. H. Chuang[1], C. L. Dong[1], W. F. Pong[1], T. Ohigashi[2], N. Kosugi[2],
Y.-S. Liu[3] and J. Guo[3]
[1]Department of Physics, Tamkang University, Tamsui 251, Taiwan
[2]UVSOR Synchrotron Facility, Institute for Molecular Science, Okazaki 444-8585, Japan
[3]Advanced Light Source, Lawrence Berkeley National Laboratory, Berkeley, CA 94720

Perovskite-based materials have been largely investigated for using as promising electrocatalysts for oxygen evolution reaction. Control of oxygen vacancies can modulate the electronic structure of perovskite and is beneficial for enhancing OER activity [1]. To further promote the oxygen evolution reaction performance, metal cation vacancies are proposed in addition to oxygen vacancies [2]. However, it is challenging to create the cation vacancies in perovskites owing to the fact that the formation energy of metal cation vacancies are too high. Herein, SnCoFe perovskite hydroxide was prepared by a simple co-precipitation, and then treated with Ar plasma to obtain the defective SnCoFe-Ar. An advanced SnCoFe hydroxide for efficient oxygen evolution reaction is developed recently [3]. The electrochemical properties and the x-ray absorption spectroscopic studies have revealed the correlation between the defective structures and the catalytic activities. Yet, the details of these defective structures are not fully understood. In this study, the SnCoFe perovskite hydroxide and that treated with Ar have been investigated by scanning transmission X-ray microscopy (STXM) which provides regional atomic/electronic structure information.

Figures 1(a) and (b) present the Fe L-edge STXM images and its stack mappings of selected region of SnFeCo and SnFeCo-Ar perovskite hydroxides. The stack mappings display red, yellow, and green areas, corresponding to the different areas which are associated with various thickness and the different electronic structures are revealed for these two samples. The spectral variations between SnFeCo and SnFeCo-Ar suggest there are more defective site formed after Ar treatment, and the chemical states of Fe are quite different in the exterior and interior region in the sample. Similarity, Figs 1(c) and (d) show the Co L-edge STXM. Interestingly, the Co is distributed more homogeneously in SnFeCo-Ar than in the one without Ar treatment. This suggest the Ar treatment has greater effect on the Co site in SnFeCo.

Further O K-edge and Sn M-edge will be performed in order to reveal the correlation between the OER activity and the defective structures in these perovskite hydroxides.

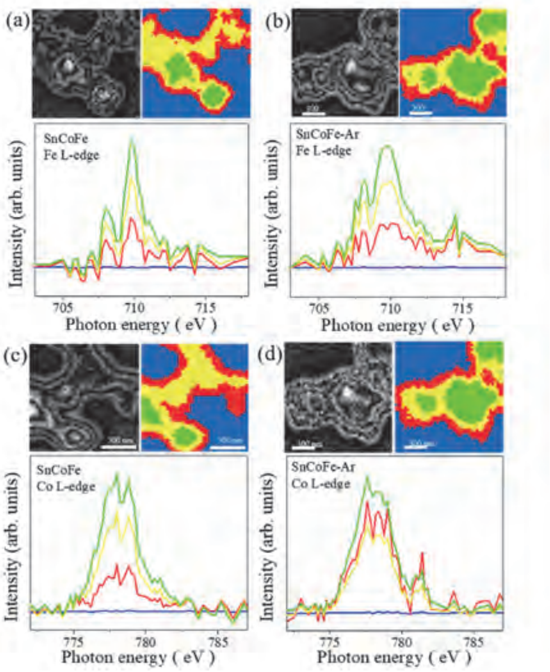

Fig. 1. Fe L-edge ((a) and (b)) and Co L-edge ((c) and (d)) scanning transmission X-ray microscopy image and its corresponding stack mappings of selected region of SnFeCo and SnFeCo-Ar.

[1] J. A. Koza *et al.*, Chem. Mater. **24** (2012) 3567.
[2] C. Yang *et al.*, J. Phys. Chem. Lett. **8** (2017) 3466.
[3] D. Chen *et al.*, Angew. Chem. Int. Ed. **57** (2018) 8691.

BL4U

Characterization of Two-phase Network Structure of Sulfur Cross-linked Isoprene Rubber

K. Miyaji[1], T. Nakajima[1], Y. Sakaki[1], J. Preeyanuch[2] and Y. Ikeda[3]
[1]*Graduate School of Science and Technology, Kyoto Institute of Technology, Kyoto 606-8585, Japan*
[2]*Research Strategy Promotion Center, Kyoto Institute of Technology, Kyoto 606-8585, Japan.*
[3]*Faculty of Molecular Chemistry and Engineering, Kyoto Institute of Technology, Kyoto 606-8585, Japan*

The cross-linking reaction to form a three-dimensional network structure in rubber is necessary to give a good rubber elasticity for rubber products. Among the conventional cross-linking reactions, a sulfur cross-linking (vulcanization) is the most important cross-linking reaction which has been widely used in rubber industries. However, the rubber network formations are generally very complicate. The controls of network structures are not easy because many cross-linking reactions proceed heterogeneously, depending on various factors such as cross-linking reagents, fillers, processing methods, and so on. Because the network structures of rubber materials significantly influence their mechanical properties, the evaluation of the rubber network structures is an important for development of rubber science and technology. In 2009, our research group found the two-phase network structure of sulfur cross-linked isoprene rubber composed of network domain and mesh network using small-angle neutron scattering. The network domains with high network-chain densities embedded in mesh network was proposed. [1] This specific morphology was found to be controlled by changing the amount of cross-linking reagents. There are several analytical methods to investigate the morphology of rubber vulcanizates. Scanning transmission X-ray microscopy (STXM) is one of methods which provides chemical mapping in nanometer scales. Also, both spatial and compositional chemical information are provided at the same time. In this study, STXM was used to confirm the two-phase network morphology of isoprene rubber vulcanizate in terms of the distribution of sulfur, and an existence of network domain in the isoprene rubber vulcanizates was confirmed.

The rubber compound was prepared by conventional mixing at room temperature on a two-roll mill with a water cooling system; isoprene rubber was mixed with zinc oxide, *N*-(1,3-benzothiazol-2-ylsulfanyl)cyclohexanamine (CBS), and sulfur. Rubber vulcanizate was prepared by conventional pressing method. This rubber vulcanizate was extracted by tetrahydrofuran (THF) to remove the un-reacted sulfur. The vulcanized rubber sheet after THF extraction was cut by an ultra-microtome to prepare a smooth and flat surface with a thickness of approximately 100 nm for STXM measurement.

Figure 1 shows the STXM image of the vulcanized isoprene rubber at 165.4 eV. The bright and dark regions indicate the strong and weak absorptions by sulfur, respectively. Thus, the brighter regions shown in Fig. 1 are possibly the clusters of sulfur in the vulcanized isoprene rubber. As predicted by the SANS results, the network domains were formed by the absorption of sulfur and the accelerator, CBS on the ZnO clusters, and followed by sulfur cross-linking on the surface of ZnO clusters [1].

This STXM image successfully confirmed the inhomogeneous two-phase network morphology in the vulcanized isoprene rubber from the view point of sulfur distribution. The localized sulfur cluster is one of the evidences for the network domain formation.

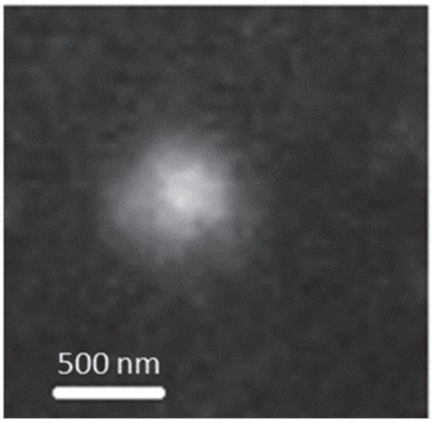

Fig. 1. STXM image of the vulcanized isoprene rubber at 164.5eV.

[1] Y. Ikeda *et. al.*, Macromolecules **42** (2009) 2741.

BL4B

Chemical State Investigation of Nitrogen in Nitrided Steels by Soft X-ray Absorption Spectroscopy

M. Sato and S-W. Young
Institute for Materials Reseach, Tohoku University, Sendai 980-8522 Japan

Machinery structural materials such as gears, shafts and molds are required to have high surface hardness and high toughness because of the severe friction and/or abrasion at the surface.

Nitriding is a surface hardening technique widely used industrially and flows nitrogen from the surface and combining with strong nitride forming elements (for example, Al, Cr, V, Ti, etc.) contained in steel to precipitate clusters and alloy nitrides at near the surface. Compared to other surface hardening methods such as carburizing and shot peening, the nitriding has advantages of less strain because it does not involve phase transformation and deformation during treatment [1, 2]. Therefore, the importance of nitriding process is increasing in recent high-precision materials. In the nitriding treatment, a sufficient amount of nitrogen flows in the vicinity of the surface to precipitate the alloy nitride at the initial stage of nitriding, whereas precipitation is delayed at the inside of the sample because it takes long time for the nitrogen diffusion. As a result, the concentration gradient of nitrogen is formed in a sample.

In this research, we aimed to investigate whether such gradient change of nitrogen can be captured by XAFS method. Since this measurement is our first beam time at BL4B, it is also an important object to acquire how to use the devices and to obtain the correct data.

A sample with a nitrogen concentration gradient from the surface to the inside was prepared by plasma nitriding treatment at 550 °C for 16 hours using the Fe-0.5V-1.5Al alloy. In addition, nitrogen martensite steel including 0.3, 0.5 and 2 mass% N prepared by nitriding and quenching (N-Q) treatment using the pure iron, and the γ'-Fe_4N and the BN powder were used as reference materials.

XAFS measurement was carried out at the beam line BL4B, and the N-K edge (380 ~ 450 eV) XANES spectra were collected by the total electron yield method, respectively. The measurement for the low concentration sample was performed a plurality of times, and the obtained spectrum was merged.

Figure 1 shows the N-K edge XANES spectra of nitrided Fe-0.5V-1.5Al samples at different depth. The shape and intensity of the obtained spectrum were different at the distance from the surface of the sample. In the case of nitriding, the reaction proceeds by diffusion of nitrogen from the surface to the inside of the sample, so the amount of nitrogen becomes thinner as it becomes inside of the sample. Obtained spectra showed such a concentration gradient of nitrogen well.

In addition, since the spectral shape is different between the sample surface and the inside, it is understood that the chemical state of nitrogen is different inside the sample. At the inside of the sample, VN clusters are precipitated mainly. On the other hand, at the sample surface, AlN and Fe_4N or $Fe_{16}N_2$ are precipitated in addition to VN clusters, and supersaturated nitrogen also exists. In the future, detailed analysis of the obtained spectrum will be performed by combining simulations.

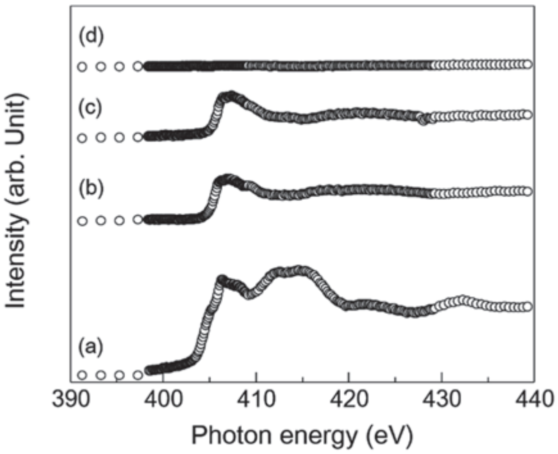

Fig. 1. N K-edge XANES spectra of nitride Fe-0.5V-1.5Al samples obtained at different depth. (a) 50 µm (b) 200 µm (c) 400 µm and (d) 600 µm, respectively.

[1] Tekkou Zairyou, The Japan Institute of Metals and Materials, 1985.
[2] K. Kawasaki, M. Okumiya and S. Uchida, NETSUSHORI **50** (2010) 305.

BL4B

Charge State Analysis of Fe Ions in Cr-doped $Y_3Fe_5O_{12}$

K. Shimazu[1] and T. Yamamoto[1,2,3]
[1]Faculty of Science and Engineering, Waseda University, Tokyo 169-8555, Japan
[2]Insitute of Condensed-Matter Science, Waseda University, Tokyo 169-8555, Japan
[3]Kagami Memorial Research Institute for Materials Science and Technology, Waseda University, Tokyo 169-0051, Japan

Thermochromism is a phenomenon to change the color due to a change in temperature. There are wide variety of organic materials, which show thermochromism. However, few inorganic ones show such thermochromism. Among such inorganic thermochromic materials, rare-earth (RE) iron garnet, $RE_3Fe_5O_{12}$, shows such color change [1]. Although it was reported that red-shift occurs by Cr-doping in one of the rare-earth iron garnet, $Y_3Fe_5O_{12}$ [2], the mechanism in such red-shift has not yet been clearly understood. In the current study, we focused upon the change in electronic structure of the Cr-doped $Y_3Fe_5O_{12}$ garnet. Especially, change in charge state of Fe ions as a function of doped Cr concentration was investigated by the Fe-L_3 X-ray absorption spectra (XAS) measurements in this report.

Cr-doped $Y_3Fe_5O_{12}$ garnet was synthesized with conventional solid state reaction method changing the concentration of doped Cr ions. Crystal structures of the synthesized powders were examined by the powder X-ray diffraction, which showed all the samples are single phased and no secondary phase could be observed. From the observed XRD patterns, we obtained the volumes of cells as a function of Cr concentration, which are shown in Fig. 1. Volumes decrease as increase of Cr concentration, which suggests Cr ions substitute at Fe site as trivalent ions. These results can be explained by the difference in ionic radii, i.e., ionic radius of Cr^{3+} ion is smaller than that of Fe^{3+} ion [3].

Fe-L_3 XAS spectra were observed at BL4B, UVSOR, in a total electron mode by collecting the drain current. Sample powders were settled on the carbon adhesive tape, which was put on the Cu plate. Incident beams were irradiated perpendicular onto the plate, which was monochromatized with a varied-space grating (800 l/mm). Observed Fe-L_3 XANES spectra are shown in Fig. 2. All the spectral profile of Fe-L_3 XAS of Cr-doped $Y_3Fe_5O_{12}$ garnet is independent from the concentration of doped Cr and shows similar profile as that of Fe_3O_4. From these results we can safely conclude that valence state of Fe ions do not change in all samples with different Cr concentration from the mixture of 2+ and 3+ as in Fe_3O_4. The red-shift is under investigation by the calculated electronic density of states within a density functional theory.

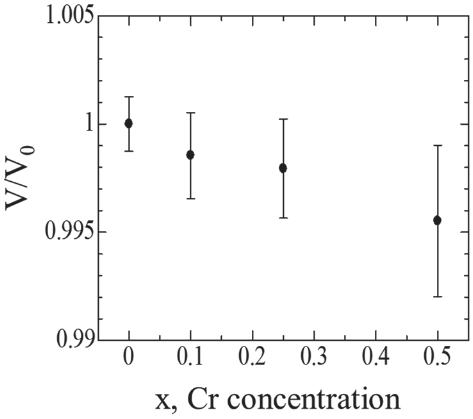

Fig. 1. Relative volume (V/V_0) of Cr-doped $Y_3Fe_5O_{12}$ ($Y_3Fe_{5-x}Cr_xO_{12}$) garnet as a function of Cr concentration.

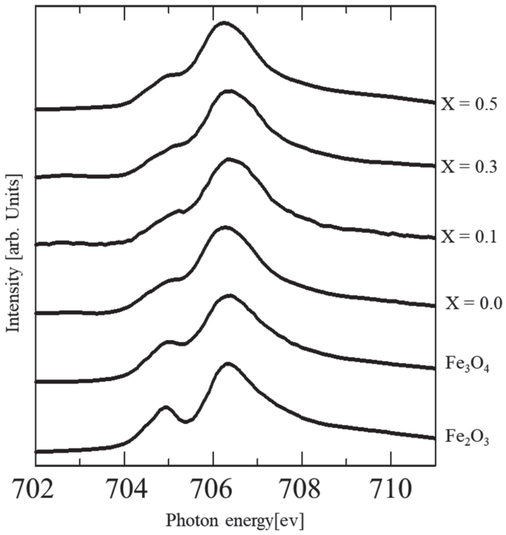

Fig. 2. Observed Fe-L_3 XANES spectra of Cr-doped $Y_3Fe_5O_{12}$ ($Y_3Fe_{5-x}Cr_xO_{12}$) with those of the standard iron oxides.

[1] S. C. Parida *et al*., J. Phase Equil. **24** (2012) 5.
[2] H. Lu *et al*., J. Mater. Chem. C**44** (2016) 15981.
[3] R. D. Shanon, Acta Cryst. A**32** (1976) 751.

BL4B

Applications of Soft X-ray Spectroscopy to the Analysis of Nitrogen Implanted TiO_2 Photocatalysts

T. Yoshida[1], M. Yamamoto[1], Y. Kato[2], A. Ozawa[2] and T. Tanabe[1]
[1]*Advanced Research Institute for Natural Science, Osaka City University, Osaka 558-8585, Japan*
[2]*Graduate School of Engineering, Osaka City University, Osaka 558-8585, Japan*

Photocatalytic reactions at the surface of titanium dioxide (TiO_2) under UV light irradiation have been attracting much attention in view of their practical applications to environmental cleaning such as self cleaning of tiles, glasses, and windows.[1] It has been reported that the doping of nitrogen into TiO_2 contributes to band gap narrowing to provide visible-light response.[2, 3] In the present study, nitrogen doped TiO_2 photocatalysts were prepared by nitrogen implantation method, and investigated the chemical states of the surface of the samples mainly by soft X-ray absorption and photoelectron spectroscopies.

Nitrogen ions were implanted into TiO_2 at 5 or 50 keV at room temperature. Photocatalytic activity of the N^+-implanted sample was evaluated by the decomposition reaction of methylene-blue solution under visible-light irradiation. The photocatalytic activity changed with the amount of implanted nitrogen, and the photocatalytic active and inactive N^+-implanted samples were obtained.

As shown in Fig. 1, O K-edge and Ti $L_{2,3}$-edge of XANES analysis exhibited the formation of Ti^{3+} species in both photocatalytic active and inactive samples (A-cat and I-cat). The Ti^{3+} species would be formed by the displacement effect of oxygen atomsduring the N^+ implantation. On the other hand, in N K-edge XANES spectra, a double-peak structure around 400 eV was observed for the photocatalytic active sample while the XANES spectrum of the photocatalytic inactive sample showed a distinct single peak around 401 eV. These results suggested two types of chemical states of nitrogen, i.e., the photocatalytic active N substituting the O sites and the inactive NO_2 species. In the valence band photoelectron spectrum of the photocatalytic active sample, the additional electronic states were observed just above the valence band edge of a TiO_2. The electronic state would be originated from the substituting nitrogen and be responsible for the band gap narrowing, i.e., visible light response of TiO_2 photocatalysts. On the other hand, the resonant photoemission spectra of the active sample under X-ray excitation around N K-edge were almost the same regardless of X-ray energy, while those of the inactive sample showed an additional sharp peak in valence band under the X-ray excitation around 401eV.

[1] A. Fujishima, X. Zhang and D. A. Tryk, Surf. Sci. Rep. **63** (2008) 515.
[2] R. Asahi, T. Morikawa, T. Ohwaki, K. Aoki and Y. Taga, Science **293** (2001) 269.
[3] R. Asahi and T. Morikawa, Chem. Phys. **339** (2007) 57.

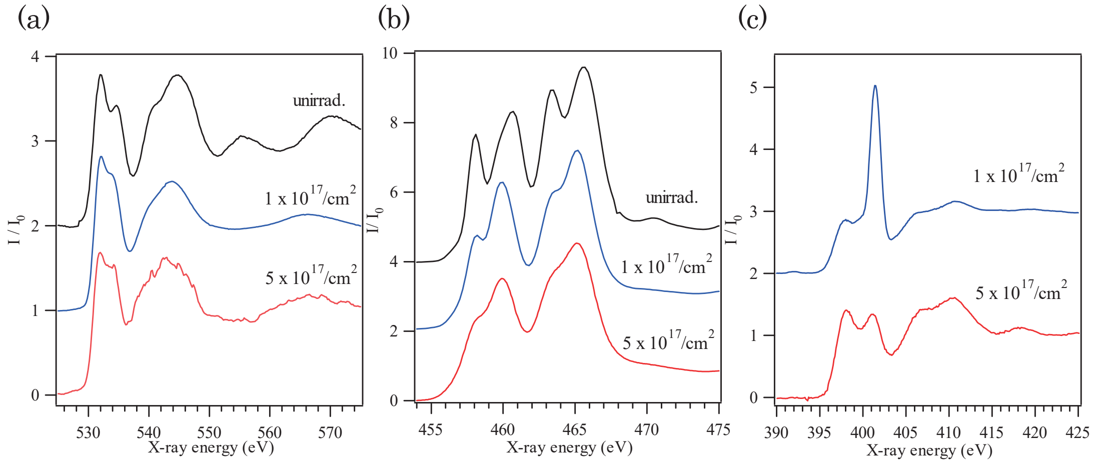

Fig. 1. (a) O K-edge XANES spectra of active sample (A-cat), inactive sample (I-cat) and a bare sample.
(b) Ti $L_{2,3}$-edge XANES spectra of active sample (A-cat), inactive sample (I-cat) and a bare sample.
(c) N K-edge XANES spectra of active sample (A-cat) and inactive sample (I-cat).
.

BL4B

N *K*-edge XAS Spectroscopy on 3*d* Transition Metal Doped AlN Films

N. Tatemizo and S. Imada
Faculty of Electrical Engineering and Electronics, Kyoto Institute of Technology, Kyoto, 606-8585, Japan

For the last two decades, wide-band gap semiconductors heavily doped with 3*d* transition metals (3*d*-TM) have been extensively investigated in order to realize devices with new functionality [1, 2]. To confer photoconversion of sun light as an intermediate band (IB) material [1], we have been exploring the possibility of heavy 3*d*-TM doping to AlN, which is in the family of III-nitrides [3-5]. For IB material, Fe is thought not to be effective because an Fe ion in an Al site of AlN have 5 3*d* electrons, that is, half-filled electronic structure. However, from the view point of chemical trend study of 3*d*-TM in AlN, Fe is an interesting dopant; the additional band mainly consisting of 3*d* states of Fe are formed very near to the valence band (VB) of AlN according to our theoretical band structure calculation, while those of Ti, V and Cr are formed in the middle of the band gap [6]. To investigate the band structures of the Fe-doped AlN (AlFeN), we synthesized AlFeN with various Fe concentration between 0-30% [7] and carried out N *K*-edge XAS measurements.

The films were deposited on SiO_2 glass substrates by RF sputtering from an AlN target with Fe metal chips on it. Results of XRD and TEM showed that the films have wurtzite structures [7]. N *K*-edge XAS measurements for the films in fluorescence-detection mode at room temperature. The electric field vectors of the X-rays were parallel to the film plane.

Figure 1 shows the N *K*-edge XAS spectra of AlFeN (7.8%) and Ti-doped AlN (AlTiN, Ti: 8.3%) films [3]. The energies of the 3 main peaks indicated black allows A, B, and C for the both films coincided with those of un-doped AlN [3]. Regarding the relative intensities of the peaks, there is a difference at the peak C. This is thought to be due to the deference in the orientation axis of the films; the AlTiN film has a *c*-axis orientation [3], while the AlFeN film has an *a*-axis orientation [7]. In both spectra, pre-edge peaks were clearly observed. Reflecting the large number of un-occupied *d*-states (9 or 10 states [3]) hybridized with N *p*-states just below the bottom of the conduction band, AlTiN film had a large pre-edge peak near the main peak. On the contrary, that of AlFeN was small and far from the main peak A. According to the result of Fe *K*-edge XANES analyses (not showing here), Fe ions have an oxidation state of 3+ ($3d^5$). It is reasonable that the spectrum of AlFeN had smaller pre-edge peak than that of AlTiN. As intensities of pre-edge peaks reflect not only un-occupation of 3*d* states but also symmetry around N, father study on the symmetries around N (Fe/Ti) should be nessesary.

The difference of the peak energies of the pre-edge peak and the main peak A is about 5 eV in the spectrum of AlFeN. This indicates that the un-occupied states were formed near the VB of AlN. This is consistent with our calculation of the band structure of AlFeN.

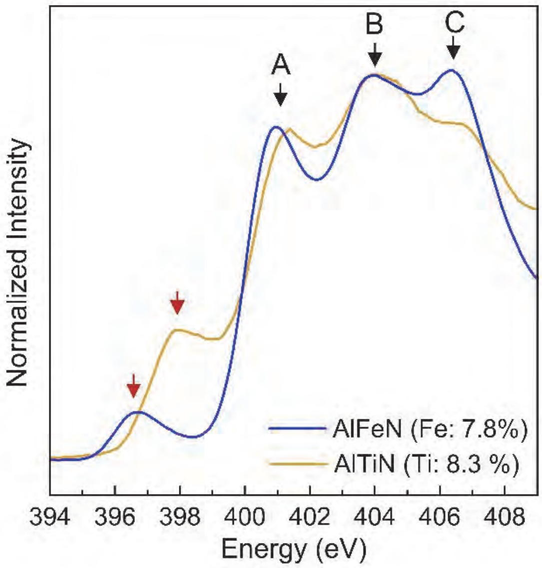

Fig. 1. N *K*-edge XAS of AlTiN (Ti: 8.3%) and AlFeN (Fe: 7.8%) films deposited on SiO_2 glass substrates.

[1] A. Luque *et al.*, Phys. Rev. Lett. **78** (1997) 5014.
[2] T. Dietl *et al.*, Science **287** (2000) 1019.
[3] N. Tatemizo *et al.*, J. Mater. Chem. A **5** (2017) 20824.
[4] N. Tatemizo *et al.*, J. Appl. Phys. **123** (2018) 161546.
[5] N. Tatemizo *et al.*, J. Phys.: Condens Matter **29** (2017) 085502.
[6] N. Tatemizo *et al.*, Materials Science Forum **924** (2018) 322.
[7] N. Tatemizo *et al.*, AIP advances **8** (2018) 115117.

BL4B

Local Structure Investigation of Alloy Nitrides Precipitated by Interface Precipitation during Ferrite Transformation

M. Sato and T. Murata
[1]*Institute for Materials Reseach, Tohoku University, Sendai 980-8522, Japan*

The pro-eutectoid ferrite formed from austenite is the most frequently appearing morphology in steel. In general, it is known that grain boundary allotriomorph ferrite are formed when the degree of supercooling from the Ae3 line is low, and the widmanstatten ferrite is formed as the degree of supercooling increases [1, 2]. In addition, in carbon steel, when the strong carbide-forming elements such as Ti, Nb, V, Cr and Mo are added, the interface precipitation occurs and alloy carbides are periodically generated on the γ / α interface during ferrite transformation.

Although there are many reports on the ferrite transformation behavior in carbon steel, there are very few reports on nitrogen steel. Under such circumstances, we have found that the interface precipitation of CrN occurs in the ferrite transformation of Fe-1Cr-0.3N austenite.

In this study, the change in chemical states of Cr and N during the ferrite transformation with interface precipitation in Fe-1Cr-0.3N austenite.

Fe-1mass%Cr alloy were used as starting materials. They were homogenized at 1523 K for 24h and furnace-cooled until room temperature. The Fe-1Cr-0.3N alloy were prepared by nitriding and quenching (N-Q) process using NH_3/H_2 mixed gas at 1273 K for 1 h. The obtained alloys were isothermally treated at 973 K for several time of periods and then quenched into iced brine. The N K-edge and Cr L-edge XANES spectra were corrected by fluorescence method using silicon drift detector (SDD) at BL4B in UVSOR, respectively. Obtained data were analyzed using Athena software.

Calculation of XANES spectrum was performed by FDMNES software and the crystal structural data was corrected from NIMS web site [3].

Figure 1 shows Cr L-edge XANES spectra of samples. In the L3 edge peak, intensity around 588 eV increased with increasing holding time due to the increasing the volume fraction of CrN precipitate.

Figure 2 shows N K-edge XANES spectrum of sample isothermally treated at 750 °C for 10 min. and calculated XANES spectrum of Fe_4N and CrN. It is thought that the obtained spectra are consisted from the combination of Fe_4N and CrN. Further detailed analysis will be performed using this kind of calculations.

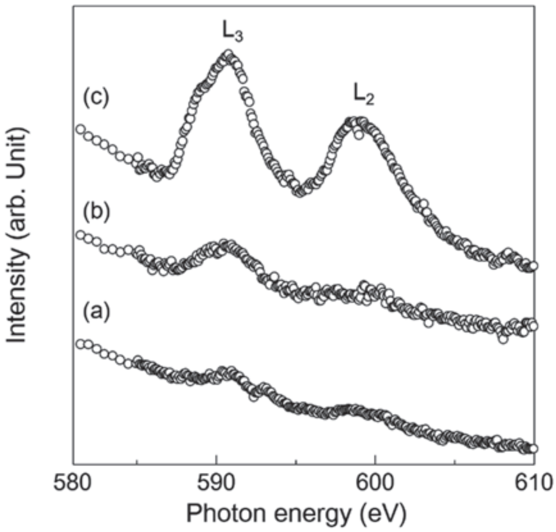

Fig. 1. Cr L-edge XANES spectra of samples (a) As quenched, (b) heat treated at 750 °C for 10 min. and (c) heat treated at 750 °C for 1 h.

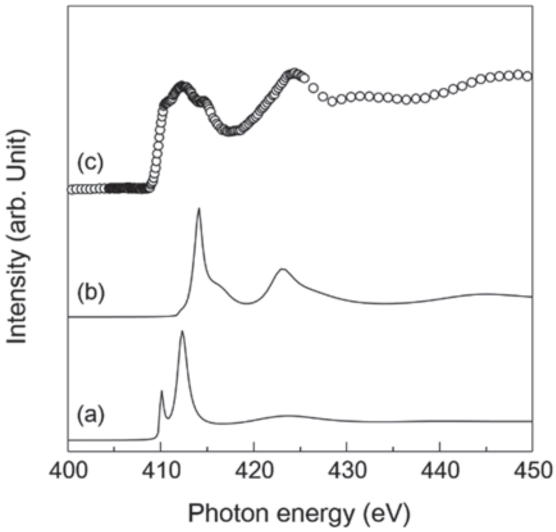

Fig. 2. Calculated and measured N K-edge XANES spectra. (a) Fe_4N (calc.), (b) CrN (calc.) and (c) heat treated at 750 °C for 10 min.

[1] Dube’ C. A., H. I. Aaronson and R. F. Mehl, Re’v.met. **55** (1958) 201.
[2] H. B. Aaron and H. I. Aaronson: Metall. Trans. **2** (1971) 23.
[3] https://crystdb.nims.go.jp/

BL5U

ARPES Study of Iron-chalcogenide High-T_c Superconductors

K. Nakayama[1], G. N. Phan[1], H. Oinuma[1], D. Takane[1], K. Sugawara[1,2], T. Takahashi[1,2,3],
F. Nabeshima[4], T. Ishikawa[4], T. Shikama[4], A. Maeda[4] and T. Sato[1,3]
[1]*Department of Physics, Tohoku University, Sendai 980-8578, Japan*
[2]*Center for Spintronics Research Network, Tohoku University, Sendai 980-8577, Japan*
[3]*WPI Research Center, Advanced Institute for Materials Research, Tohoku University, Sendai 980-8577, Japan*
[4]*Department of Basic Science, the University of Tokyo, Tokyo 153-8902, Japan*

Iron chalcogenides Fe*Ch* (*Ch*: S, Se, Te) have long been attracting considerable attention as the structurally simplest iron-based superconductors. These materials show rich physical properties such as superconductivity, antiferromagnetism, structural transition, and electronic nematicity. Intriguingly, these physical properties exhibit gigantic pressure effects, as exemplified by a marked increase in a superconducting transition temperature (T_c) from 8 K to 37 K in pressurized FeSe [1]. Understanding the origin of such pressure-induced T_c enhancement would provide a key to resolving the high-T_c mechanism in iron-based superconductors.

Recent successful fabrication of $FeSe_{1-x}Te_x$ thin films allows us to control the lattice parameters by tuning the lattice mismatch with substrate. Such strain engineering has great capability for manipulating various physical properties. For example, the application of compressive strain enhances the T_c value up to 12 K in FeSe on CaF_2 [2, 3] and further up to 23 K in $FeSe_{0.8}Te_{0.2}$ on CaF_2 [4]. In addition, strain-induced drastic changes in the structural, magnetic, and nematic properties have been discovered in $FeSe_{1-x}Te_x$ [5]. These findings have provided a rare opportunity for investigating the interplay between the physical properties and the lattice parameters at ambient pressure.

In this study, we have performed high-resolution angle-resolved photoemission spectroscopy (ARPES) of compressive-strained and strain-free $FeSe_{1-x}Te_x$ thin films at BL5U, and determined their band structure in the three-dimensional momentum space. Our systematic ARPES measurements revealed the strain-induced evolution of Fermi surface and electronic nematicity as well as their relationship with T_c variation.

High-quality compressive-strained $FeSe_{1-x}Te_x$ thin films with the thicknesses of approximately 300 monolayers were grown on CaF_2 substrate by pulsed laser deposition. Figure 1 shows the representative ARPES results in the normal state of $FeSe_{0.8}Te_{0.2}$ (T_c = 23 K) measured with circularly-polarized 40-eV photons. We observed several dispersive bands near the Fermi level (E_F), which mainly originate from Fe 3*d* orbitals. Fermi surfaces consist of hole-like and electron-like small pockets at the Brillouin-zone center (Γ point) and corner (M point), respectively (see Fig. 1). Similar size of these Fermi surfaces supports the semimetallic nature of $FeSe_{0.8}Te_{0.2}$. We have also performed ARPES measurements on several different samples such as strain free and different compositions, and found strain- and Te-substitution-induced changes in the semimetallic band overlap and the nematicity. Our observations provide important insights into the interplay between T_c enhancement and lattice parameters.

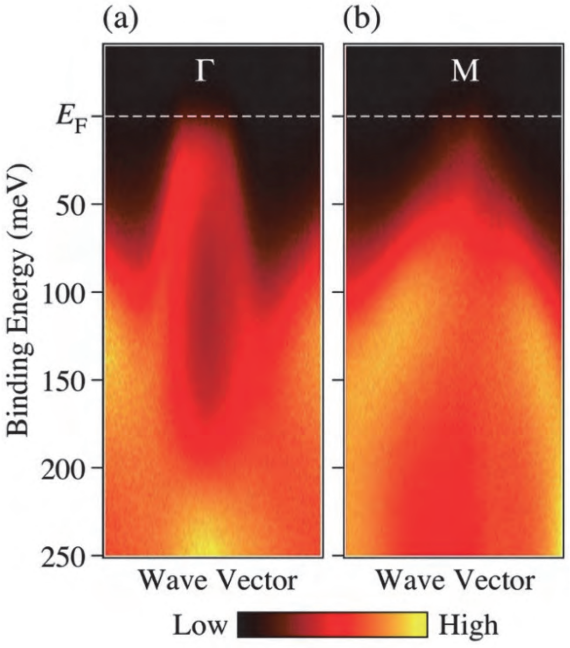

Fig. 1. (a) and (b) ARPES intensity plot as a function of binding energy and wave vector measured around the Brillouin-zone center and corner, respectively, on $FeSe_{0.8}Te_{0.2}$ (T_c = 23 K) at T = 30 K. The data were obtained with circularly-polarized 40-eV photons.

[1] S. Medbedev *et al.*, Nature Mater. **8** (2009) 630.
[2] F. Nabeshima *et al.*, Appl. Phys. Lett. **103** (2013) 172602.
[3] G. N. Phan *et al.*, Phys. Rev. B **95** (2017) 224507.
[4] Y. Imai *et al.*, Proc. Natl. Acad. Sci. USA **112** (2015) 1937.
[5] Y. Imai *et al.*, Sci Rep. **7** (2017) 46653.

BL5U

Observation of Fermi-arc Surface States in CoSi

D. Takane[1], Z. Wang[2], S. Souma[3,4], K. Nakayama[1], T. Nakamura[1], H. Oinuma[1], K. Hori[1],
K. Sugawara[1,3], T. Takahashi[1,3,4], Y. Ando[2] and T. Sato[1,3]
[1]*Department of Physics, Tohoku University, Sendai 980-8578, Japan*
[2]*Physics Institute II, University of Cologne, 50937 Köln, Germany*
[3]*Center for Spintronics Research Network, Tohoku University, Sendai 980-8577, Japan*
[4]*WPI Research Center, Advanced Institute for Materials Research, Tohoku University, Sendai 980-8577, Japan*

The search for new fermionic particles, which has long been an important research target in elementary-particle physics, is now becoming an exciting challenge in condensed-matter physics to realize exotic fermions, as highlighted by the discovery of two-dimensional (2D) Dirac fermions in graphene and helical Dirac fermions at the surface of three-dimensional (3D) topological insulators. The recent discovery of 3D Dirac semimetals and Weyl semimetals hosting massless Dirac-Weyl fermions further enriches the category of exotic fermions. While all these fermions could manifest themselves in elementary-particle physics, recent theories have predicted new types of massless fermions in condensed-matter systems that have no counterparts in elementary particles. These fermions appear in the crystals with specific space groups, such as CoSi, as exemplified by the spin-1 chiral fermion and the double Weyl fermion showing multifold band degeneracies at the band-crossing point (node) protected by the crystal symmetry [1-3] [Fig. 1(a)]. While a well-known spin-1/2 Weyl fermion shows a Weyl-cone energy band dispersion with twofold degeneracy at the node that carries the topological charge (Chern number) C of ±1, these novel fermions carry topological charge of ±2, and hence produce multiple (double) Fermi-arc surface states.

In this study, we performed angle-resolved photoemission spectroscopy (ARPES) of CoSi at BL5U. By utilizing energy-tunable photons from synchrotron radiation, we found first experimental evidence for unconventional Fermi-arc surface states that strongly support the presence of spin-1 chiral fermion and double Weyl fermion in the bulk [4].

High-quality single crystals of CoSi were grown by a chemical vapor transport method. To search for the predicted Fermi-arc surface states, we selected $hv = 67$ eV, which corresponds to $k_z \sim 0.75\pi$ at $k_x \sim 0$ to avoid a possible complication from the bulk bands. As shown in the upper left panel of Fig. 1(b), the ARPES intensity at the Fermi level (E_F) is elongated toward two of four adjacent $\bar{M}$ points, resulting in a C_2-symmetric "Z"-shaped intensity pattern. This feature is commonly observed at other hv's [Fig. 1(b)] despite a sizable change in the k_z value [0.3- 0.95π]. We found that the energy dispersion of the E_F-crossing band that produces the Z-shaped Fermi contour seems to be unchanged against a variation of hv These results strongly suggest the surface origin of the Fermi contour in Fig. 1(b). This Fermi contour is attributed to the predicted Fermi-arc surface states, since the calculated surface states are C_2 symmetric and connect with the bulk FSs at the $\bar{\Gamma}$ and $\bar{M}$ points, consistent with the present ARPES results. The present study strongly supports the existence of chiral topological fermions beyond Dirac and Weyl fermions in condensed-matter systems.

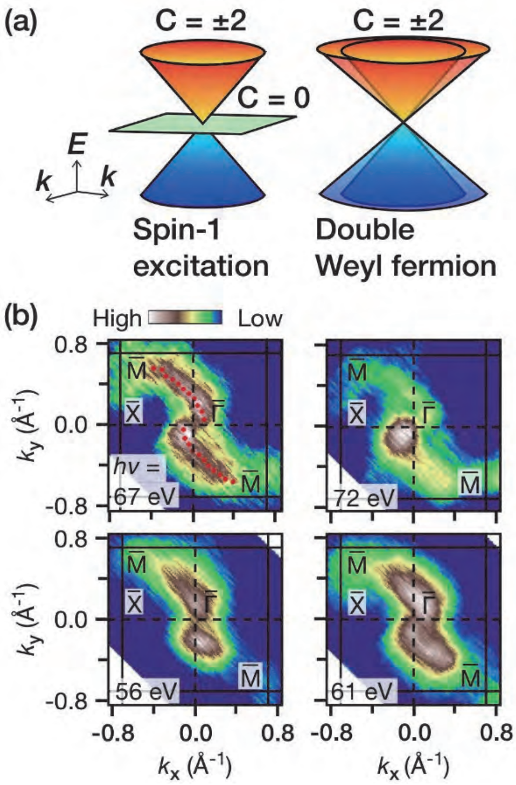

Fig. 1. (a) Spin-1 chiral fermion (left), and double Weyl fermion (right). (b) Fermi-surface mapping of CoSi at hv= 67 eV which indicates the existence of Fermi-arc surface states.

[1] B. Bradlyn *et al*., Science **353** (2016) aaf5037.
[2] G. Chang *et al*., Phys. Rev. Lett. **119** (2017) 206401.
[3] P. Tang *et al*., Phys. Rev. Lett. **119** (2017) 206402.
[4] D. Takane *et al*., Phys. Rev. Lett. **122** (2019) 076402.

BL5U

Investigating Electronic Structures of the Strained Transition Metal Dichalcogenide Monolayers

D. J. Oh[1,2], B. Kim[1,2], K. Tanaka[3], S. R. Park[4] and C. Kim[1,2]
[1]*Department of Physics and Astronomy, Seoul National University (SNU), Seou 08826l,Republic of Korea*
[2]*Center for Correlated Electron Systems, Institute for Basic Science (IBS), Seoul 08826, Republic of Korea*
[3]*UVSOR Synchrotron Facility, Institute for Molecular Science, Okazaki 444-8585, Japan*
[4]*Department of physics, Incheon National University, Incheon 406-772, Korea*

Transition metal dichalcogenides (TMDs) monolayer (ML) such as MoS_2 and $NbSe_2$ have recently drawn a lot of attentions because of their novel properties distinguished from their bulk formed materials [1, 2]. It is desired to manipulate the electronic structures and materials properties of TMDs ML by applying external field or strain. Uniaxial strained MoS_2 ML was recently realized by a special method using a flexible substrate and exhibit a interesting property [3]. The electronic structure of monolayer MoS_2 can be modified by uniaxial strain. When the current was applied to the sample, strained monolayer MoS_2 can has valley polarization. In addition, the direction of the valley polarization can be controlled by the direction of the current [3].

We bought the $MoSe_2$ single crystal from the HQ graphene. We exfoliated the thick $MoSe_2$ flakes from single crystal on the viscoelastic substrate [4]. Then we applied the uniaxial strain using a mechanical translation stage [3]. Finally, we transferred a $MoSe_2$ flake onto the degeneratly doped Si substrate. Samples were annealed at 700K for 2h in UHV to cleaning the surface before ARPES measurements. ARPES spectra were acquired by hemispherical photoelectron analyzer (MBS A-1) equipped with deflectors that enable momentum space mapping. The base pressure is better than 5×10^{-11} torr. We used linearly polarized light with 80eV photon energy.

We have tried to measure the electronic structure of strained $MoSe_2$ by angle resolved photoemission in UVSOR BL5U. Figure 1(a) is the constant energy cut obtained at -2.4 eV binding energy. There are two hole pockets at Γ and K-point. In Fig. 1(b), there are band splitting induced by spin-orbit coupling and it was coincident with previous work [5]. Due to the small spin-orbit coupling in $MoSe_2$, it is hard to measure the size of splitting. And we couldn't measure any modified electronic structure induced by uniaxial strain. We assume that the applied uniaxial strain is too small to modify the electronic structure. Or the applied uniaxial strain was released during the annealing process. Furthermore, we have check the charging effect. We measure the energy distribution curve (EDC) with two different entrance slit size. In Fig. 2, measured EDC is shifted to higher binding energy when we use larger entrance slit. It is general tendency when there is a charging effect. It seems to be came from poor electrical contact between Si substrate and $MoSe_2$ flake or the presence of SiO_2 layer on the Si substrate.

Based on these results, we were able to identify the problems to be solved. We will try to make better electrical contact or use another conducting substrate. And we will try to apply uniaxial strain using another method which can maintain the uniaxial strain during ARPES measurement.

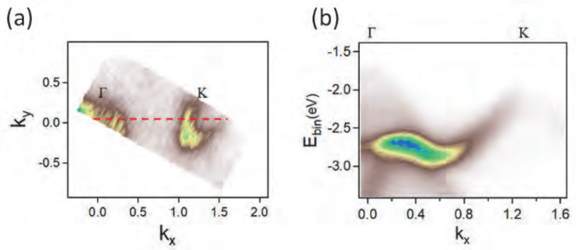

Fig. 1. (a) Constant energy cut obtained at the -2.4 eV binding energy (b) Measured dispersion along the red dashed line in Fig. 1 (a).

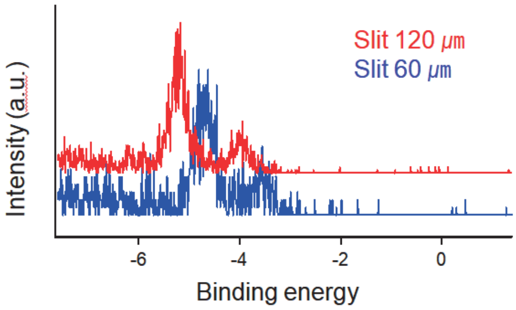

Fig. 2. Measured energy distributrion curves using two different slit size.

[1] D. Xiao *et al.,* Phys. Rev. Lett **108** (2012) 0196820.
[2] M. Ugeda *et al.,* Nature Physics **12** (2016) 92.
[3] J. Lee *et al.,* Nat. Materials **16** (2017) 887.
[4] A. Castellanos-Gomez *et al.,* 2D Mater. **1** (2014) 011002.
[5] B. S. Kim *et al.,* Sci. Rep. **6** (2016) 36389.

BL5U

Angle-Resolved Photoemission Spectroscopy Study of Fermi Surface and Superconducting Gap in $NdFeAs_{0.4}P_{0.6}(O,F)$

Z. H. Tin[1], T. Adachi[1], A.Takemori[1], S. Ideta[2,3] K. Tanaka[2,3] S. Miyasaka[1] and S. Tajima[1]
[1]*Department of Physics, Graduate School of Science, Osaka University, Toyonaka 560-0043, Japan*
[2]*UVSOR Synchrotron Facility, Institute for Molecular Science, Okazaki 444-8585, Japan*
[3]*School of Physical Sciences, The Graduate University for Advanced Studies (SOKENDAI), Okazaki 444-8585, Japan*

The discovery of IBSs has bestowed us an alternative direction to investigate the origin of superconductivity. Amongst the various type of families in Fe-based superconductors, 1111-system such as NdFeAs(O,F) achieves the highest T_c, which is 55K. In spite of highest T_c, 1111-system is not well-researched. The reasons behind are the difficulty of synthesizing single crystal and no cleaved surface with electrical neutrality. In our previous study, we are able to observe the evolution of Fermi surfaces and T_c accordance to isovalent doping of As site to P. [1] In addition, we had measured the superconducting gap of NdFeAs(O,F) by using ARPES method. In this report, we show the ARPES result of $NdFeAs_{0.4}P_{0.6}(O,F)$.

The single crystals of $NdFeAs_{0.4}P_{0.6}(O,F)$ were grown by self-flux method under high pressure using a cubic anvil press machine. [1, 2] T_c of the single crystal was about 11 K. The ARPES data were measured at BL5U of UVSOR facility.

The in-plane mapping of Fermi surfaces (FSs) in *P* and *S*-polarized photon configurations at 60eV were shown in Fig. 1. In these mappings, three hole FSs and two electron FSs can be clearly seen in Γ(0,0) and M(1,-1) points, respectively.

The k_z dependence of all FSs were measured by changing the energy of the incident photon and the results were shown in Fig. 2. All the FSs showed less dispersive feature along the k_z direction. The largest hole FS (arrow mark) remains around zone center even by 60% P-doping. This largest FS is treated as surface state from polar-cleaved surface of the 1111-type superconductors. Γ points determined to be around 64 eV with inner potential of 18 eV.

The superconducting gap measurement was carried out on the FSs around the Γ and M points in *P*-polarized photon configuration. Figure 3 shows the symmetrized energy-distribution curves (EDCs) at the various k point on the inner and outer hole FSs around the Γ point, and on the inner electron FS around M point. In the symmetrized EDCs at 5 K, the coherence peaks or the shoulder like structures can be observed around 10 meV, suggesting the superconducting gap ~ 10 meV. However, these peaks or the shoulder like structure do not diminish at 19 K. This behavior suggests that the peak and the shoulder like features are due to pseudogap, which was often observed in the Fe-based superconductors.

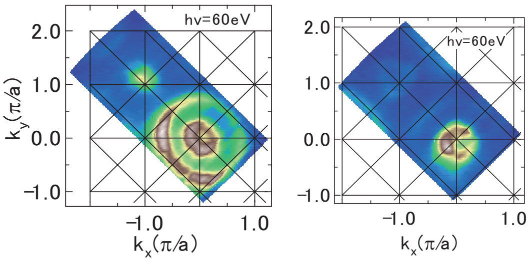

Fig. 1. FS mapping of $NdFeAs_{0.4}P_{0.6}(O,F)$ in *P* and *S*-polarized configurations (left and right panels) at 60eV.

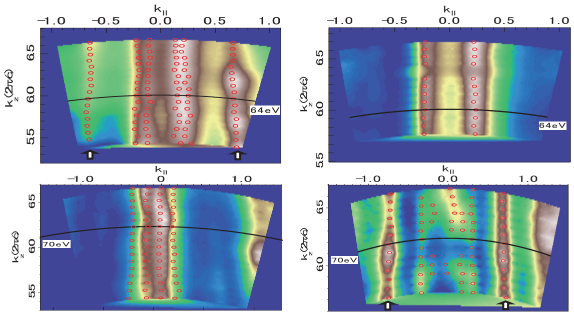

Fig. 2. k_z dependence of FSs of $NdFeAs_{0.4}P_{0.6}(O,F)$ in *P* and *S*-polarized configuration (left and right panels). Top and bottom panels show the results of hole and electron FSs, respectively.

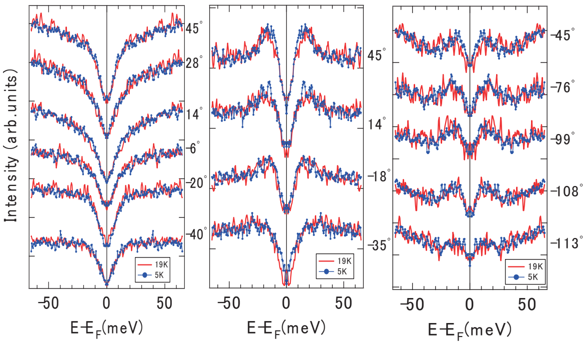

Fig. 3. Symmetrized EDC of inner (left), outer (middle) hole bands and inner electron band (right) at 5 K (blue) and 19 K (red).

[1] A. Takemori *et al.*, Phys. Rev. B **98** (2018) 100501(R).
[2] A. Takemori *et al.*, JPS Conf. Proc. **1** (2014) 012111.

BL5U, BL7U

Study on Interaction between Charge Density Wave Collective Modes and Electrons

Y. Lee, J. Hyun, C.-Y. Lim, G. Lee, S. Kim and Y. Kim
Korea Advanced Institute of Science and Technology (KAIST), Daejeon, 34141, Republic of Korea

Among atomic-layer materials, transition-metal dichalcogenides (TMDs) have been an attractive system to research due to their various physical properties such as superconductivity, charge-density wave (CDW), magnetic ordering, etc. Amongst various properties, competition between CDW phase and superconductivity provides an important playground to study the possible connection between CDW fluctuation and superconductivity. The suitable system for such study is 2H-TaSe$_2$. It shows superconducting transition $T_c \sim 0.15$ K. Also, there exists two CDW transitions: from normal phase to incommensurate CDW phase at 122 K and from incommensurate CDW phase to commensurate CDW phase at 90 K [1].

In our previous work and other early studies, kink near Fermi level is observed along M-K high symmetry direction in 2H-TaSe$_2$ [2, 3] which shows clear temperature dependence across the CDW transition. It is not expected behavior of ordinary kink produced through electron-phonon interaction. Instead, such temperature dependence implies a possible role of CDW fluctuation on the observed renormalization. If we can clearly demonstrate that the kink develops below CDW transition temperature apart from the band folding and disappears after CDW relaxation, we can conclude that the coupling between collective excitation mode of CDW and electron is responsible for the kink. It will be the first step towards the understanding on the relationship between CDW and superconductivity.

In this study, we have performed high-resolution angle-resolved photoemission spectroscopy (ARPES) on 2H-TaSe$_2$ single crystals grown by chemical vapor transport (CVT) method [4]. ARPES experiments were conducted on Beamline 5U and 7U at UVSOR, using linearly horizontal polarized photon of $hv = 50$ eV. Total energy resolution was set to 20 meV. Samples were cleaved *in situ* in the condition of pressure lower than 1×10^{-8} Pa at temperature 10 K. In order to observe temperature evolution of kink, we measured the electronic band structure at 10 K, 70 K, 110 K, 150 K respectively.

Figure 1(a) shows the band dispersion of 2H-TaSe$_2$ along M-K direction taken at 10 K. Dispersion also M-K is free from band folding due to symmetry lowering. We observed the kink at binding energy around 10 meV near M point. Figure 1(b) shows the kink (upper) and corresponding peak positions of momentum distribution curve (MDC) fitting at four different temperatures (lower). We observed that kink disappears above 70K. Therefore, the present result clearly suggests that the kink is weakened as CDW phase transition occurs at 90 K, and thus it is originated from electron-CDW coupling.

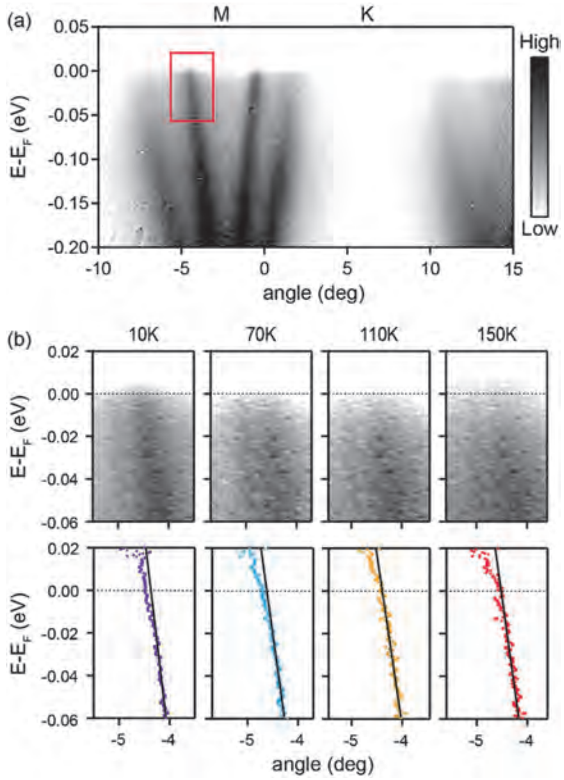

Fig. 1. (a) Band dispersion of 2H-TaSe$_2$ along M-K direction of BZ taken at 10 K. Kink structure is shown in the red box. (b) Temperature evolution of kink structure and corresponding peak positions of MDC fitting of 2H-TaSe$_2$ (in the red box of (a)).

[1] D. E. Moncton *et al.*, Phys. Rev. B **16** (1977) 801.
[2] T. Valla *et al.*, Phys. Rev. Lett. **85** (2000) 4759.
[3] K. Rossnagel *et al.*, Phys. Rev. B **72** (2005) 121103(R).
[4] L. H. Brixner *et al.*, J. Inorg. Nucl. Chem. **24** (1962) 257.

BL5U

Polarization-dependent Angle-resolved Photoemission Study of MAX Phase compound Ti_2SnC

T. Ito[1,2], M. Ikemoto[2], D. Pinek[3], M. Nakatake[4], S. Ideta[5,6], K. Tanaka[5,6] and T. Ouisse[3]
[1]*Nagoya University Synchrotron radiation Research center (NUSR), Nagoya University, Nagoya 464-8603, Japan*
[2]*Graduate School of Engineering, Nagoya University, Nagoya 464-8603, Japan*
[3]*Grenoble Alpes, CNRS, Grenoble INP, LMGP, F-38000 Grenoble, France*
[4]*Aichi Synchrotron Research Center, Seto 489-0965, Japan*
[5]*UVSOR Synchrotron Facility, Institute for Molecular Science, Okazaki 444-8585, Japan*
[6]*The Graduate University for Advanced Studies, Okazaki 444-8585, Japan*

MAX phase compounds, i.e., $M_{n+1}AX_n$ where M is a transition metal, A belongs to groups 13-16 and X is the C or N element, have recently been attracted much attention due to their possible application for new class of two-dimensional systems called MXenes by removing A atoms [1]. On the other hand, the bulk electronic structure of MAX phase has been studied mostly by calculations, mainly because of lack of well-established single crystalline samples. In this study, we have performed angle-resolved photoemission spectroscopy (ARPES) on MAX phase compound Ti_2SnC [2] to directly investigate the electronic structure of this system.

ARPES measurements were performed at the UVSOR-III BL5U. Data were acquired at T = 25 K with hν = 71.5 eV which enables us to trace around the ΓKM plane with inner potential of V_0=10.7 eV estimated from the photon energy dependent measurement (not shown). With using linear horizontally (LH), vertically (LV) and circularly right (CR), left (CL) polarized photons, we have obtained the orbital and orbital-angular-momentum (OAM) dependent ARPES images. It should be noted that each ARPES images were obtained without changing the photon incident angle relative to the sample surface by utilizing two-dimensional mapping lens mode of MBS A-1 analyzer.

Figure 1 shows the obtained Fermi surface (FS) image on the ΓKM plane (a) compared with the FS topologies calculated by DFT method (b, c). The band structure along the ΓM and ΓK line is shown in Fig. 2 (a) together with the DFT calculation [2]. Six-folded symmetry of hole-pockets α and β has clearly been observed in consistent with the DFT calculations. In addition, three-fold symmetry around the M point of the small FS γ formed by the electron and hole dispersive feature crossing below the Fermi level along the ΓK line has also been elucidated in Fig.1 (a). Furthermore, we have found that the γ branch has been formed by the Dirac-cone-like dispersive feature along k_y axis (Figs. 2 (b), (c)). More interestingly, the γ branch shows opposite OAM sign without changing orbital symmetry with respect to the ΓM line. The results indicate the change of chirality of OAM between the two γ branches in Fig. 2 (c). To elucidate the relation between the observed anomalies and the spin-orbit coupling effect, further studies are intended.

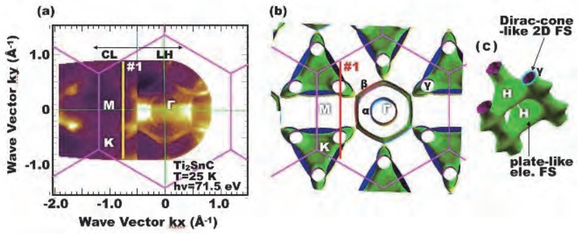

Fig. 1. Fermi surface (FS) image on ΓKM plane of Ti_2SnC (a). (b,c) FS calculated by DFT shown as projection along the [001] axis (b) and enlarged FS around the KH axis (c).

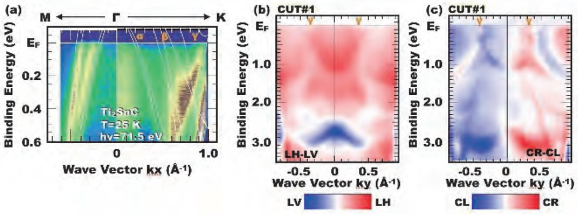

Fig. 2. (a) Band structure along the ΓM and ΓK line of Ti_2SnC obtained by LH polarized photons. Solid lines are DFT calculation. (b, c) orbital (b) and OAM (c) dependent ARPES image of Ti_2SnC along the cut#1 (k_x = −0.7 $Å^{-1}$) in Fig. 1., which is obtained by subtracting the ARPES results of linearly (LH−LV) and circularly (CR−CL) polarized photons, respectively.

[1] M. Basoum, MAX phases (Wiley, Weinheim 2013).
[2] J. Y. Wu, Y. C. Zhou, J. Y. Wang, Mat. Sci. Eng. A **422** (2006) 266.

BL5B

Study on Optical Properties of Metallic Sodium by Vacuum Ultra Violet in UVSOR

M. Kawaguchi [1], J. Saito[1], H. Daido[2] and T. Suemoto[3]

[1]Sodium Technology Development Group, Japan Atomic Energy Agency, Tsuruga 919-1279, Japan
[2]Institute of Laser Engineering, Osaka University, Suita 565-0871, Japan
[3]Toyota Physical and Chemical Research Institute, Nagakute 480-1192, Japan

Metallic sodium (Na) is well-known as a typical alkali metal and very reactive material with oxygen and/or moisture. The physical properties of Na have been researched experimentally and theoretically for a long time [1, 2]. Recently, the paper entitled on "Demonstration of partially transparent thick metallic sodium in the vacuum ultraviolet spectral range [3]" was published by one of the authors (H. D.), and it demonstrated vacuum ultraviolet light (Wave length: 115-180 nm) penetrates in several millimeters of Na with high transmittance for the first time. To elucidate theoretically this mysterious and novel phenomenon, the aim of this research is to obtain the accurate spectrum using BL5B in UVSOR.

Figure 1 shows the outline of the Na sample which was fabricated in glove box of argon gas atmosphere (O_2 concentration: less than 1.0 ppm, Dew point: less than -76 °C) in Sodium Engineering Research Facility (SERF) [4] in Japan Atomic Energy Agency where the R&D programs on the advanced sodium handling technology have been conducted. The Na sample which consisted of the inner and safety cells was designed to improve the safety for the chemical reactivity and to prevent from oxidizing Na surface. The inner and safety cells functioned correctly during transportation from SERF to UVSOR, and Na sample maintained metallic luster. The gas conditions in the both cells were inert argon gas. The ER grade of Na (Na: 99.98%, Ca and K: less than 10 ppm) which was provided from Metaux speciaux was filled between MgF_2 windows in the inner cells by immersion in the liquid Na for high quality. Figure 2 shows the Na sample set up in the chamber of BL5B in UVSOR. The chamber was vacuumed by turbo-molecular pumps during measuring the transmittance.

Now, we started the measurement of the transmittance for the four Na samples using 100-200 nm in wave length: (1) clean MgF_2 windows, (2) MgF_2 windows after immersion in liquid Na, (3) MgF_2 windows + Na (thickness: 0.2 mmt) and (4) MgF_2 windows + Na (thickness: 5 mmt). From the difference of each spectrum, we recognized possibility to occur the intransparent layer for vacuum ultraviolet light on the MgF_2 windows. In the near future, we will improve the Na sample to solve the problems and conduct the measurement again.

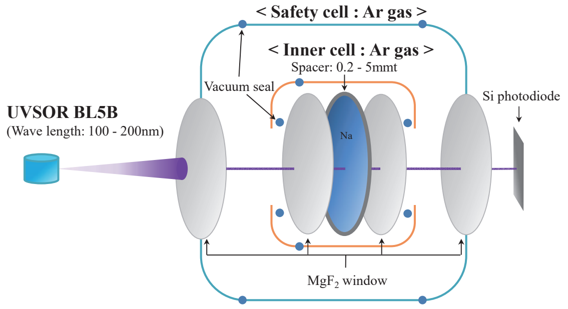

Fig. 1. Outline of the inner and safety cells to prevent oxidizing sodium surface.

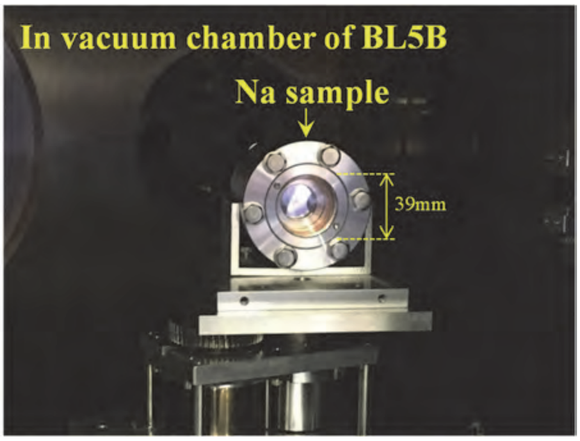

Fig. 2. Na sample (inner and safety cells) set up in the vacuum chamber of BL5B in UVSOR.

[1] J. C. Sutherland *et al.*, Optical properties of sodium in the vacuum ultraviolet (ORNL-TM-1776, Oak Ridge National Laboratory, 1967).
[2] R. W. Wood, Phys. Rev. **44** (1933) 353.
[3] H. Daido *et al.*, Optics express **21** (2013) 28182.
[4] https://www.jaea.go.jp/04/turuga/center/fpc/index.htm.

BL6U

Orbital Mapping of One-dimensionally Ordered Picene Film on Ag(110)

Y. Yamada [1], M. Iwasawa[1], N. Sumi[1], M. Meissner[2,3], T. Yamaguchi[3], S. Kera[2,3] and F. Matsui[2]
[1]*Faculty of Pure and Applied Sciences, University of Tsukuba, Tsukuba 305-8573, Japan*
[2]*UVSOR Synchrotron Facility, Institute for Molecular Science, Okazaki 444-8585, Japan*
[3]*School of Physical Sciences, The Graduate University for Advanced Studies, Okazaki 444-8585, Japan*

For an establishment of the state-of-art orbital mapping and orbital tomography, a well-defined molecular layer is surely required for a model system. Especially, the molecular layer with single-domain structure is preferred for the detailed analysis of the angular distribution of the photoelectrons. However, such a film of the small organic semiconductor molecules has been rare, because they usually forms rotational domains even on the single crystalline substrate.

We have recently shown that, by using small organic semiconductor molecules with strong intermolecular interaction such as picene, nicely ordered molecular films can be realized [1, 2]. We have further demonstrated that, using anisotropic surface of Ag(110), a nearly single-domain film of picene can be fabricated [3]. Here, we tried to measure angular dependence of the photoelectron intensity of the single-domain, multilayer film of picene on Ag(110).

The single-domain film of picene were formed by supplying approximately 10 nm of picene on the clean on Ag(110). The thickness of the film was monitored with the quartz microbalance and the film structure were examined in situ by scanning tunneling microscopy (STM) and low-energy electron diffraction (LEED). Photoemission experiments were done at BL6U of UVSOR, equipped with A1 analyzer (MB Scientific) which enables the mechanical deflector scan in the direction perpendicular to the analyzer slit. The intensity mapping was measured with increasing acceptance angle of photoelectrons, by applying potential of 400eV to the mesh electrode in front of the sample. Sample temperature was 15 K.

Figure 1 (a) shows the STM image of the multilayer picene film on Ag(110). It is seen that the multilayer film film consists of one-dimensional molecular rows only along [1 -10] direction of the substrate. It is found that the molecular long axis of picene in the 1D row structure is also along [1-10] direction, from the detailed STM image of the row, shown in Fig.1 (b). Therefore, it is considered that the picene film on the Ag(110) surface is suitable for orbital mapping because of the fact that the molecular axis is aligned in one direction. However, we also have to note that the detailed molecular arrangement in the present structure have yet been fully clarified.

Figure 2(a) shows the UPS spectrum of the multilayer picene film on Ag(110). It is seen that HOMO, HOMO-1 and HOMO-2 are close to each other and difficult to distinguish in the sspectrum, consistent to the previous reports. However, in the photoelectron intensity mapping shown in Fig. 2(b), HOMO and HOMO-1 can be well separated; HOMO maxima comes in the direction perpendicular to the molecular axis, while that of HOMO-1 comes direction along the molecular axis. This behavior is consistent with the simple simulation of the photoelectron distribution, by means of FFT of the molecular orbitals as shown in the inset, suggesting that the film is indeed consist of the single domain of picene and that the system is suitable for further detailed measurements and analysis.

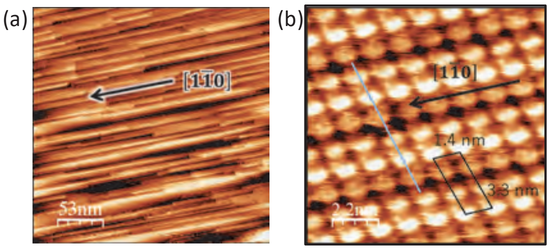

Fig. 1. (a) STM image of picene multilayer film on Ag(110), 200 nm x 200 nm, and (b) a detailed scan.

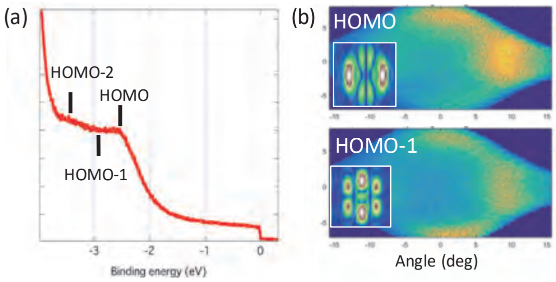

Fig. 2. (a) UPS spectrum of the picene multilayer film on Ag(110) (b) Intensity mapping of HOMO and HOMO-1. FFT of the molecular orbitals are displayed in the inset.

[1] Y. Hasegawa, Y. Yamada, T. Hosokai, Y. Wakayama, K. Rasika, M. Yano and M. Sasaki, J. Phys. Chem. C **120** (2016) 21536.

[2]C. Zhang, H. Tsuboi, Y. Hasegawa, M. Iwasawa, M. Sasaki, Y. Wakayama, H. Ishii and Y. Yamada, ACS Omega, (in press).

[3] 長谷川友里，山田洋一，佐々木正洋，表面と真空，2018 年 61 巻 6 号 p. 366-371.

BL6B

Analogy of Trapped Electron Centers in Ce:GGG and Ce:LuGG Crystals

T. Yagihashi[1], M. Kitaura[1], K. Kamada[2], S. Kurosawa[2], S. Watanabe[3], A. Ohnishi[1] and K. Hara[4]
[1]*Faculty of Science, Yamagata University, Yamagata 990-8560, Japan*
[2]*New Industry Creation Hatchery Center, Tohoku University, Sendau 980-0845, Japan*
[3]*Graduate School of Engineering, Nagoya University, Nagoya 464-8603, Japan*
[4]*Research Institute of Electronics, Shizuoka University, Hamamatsu 432-8011, Japan*

The nature of shallow electron traps in Ce:$Gd_3Al_{5-x}Ga_xO_{12}$ crystals has been studied so far. Grigorjeva *et al*. have performed luminescence spectroscopy, and tentatively attributed the origin of shallow traps to Ga^{2+} ions perturbed by the nearest neighboring Ce^{3+} ions [1]. We have carried out infrared absorption spectroscopy, and found two types of shallow electron traps [2]. The one is the antisite Gd^{2+} ion adjacent to oxygen vacancies, which is formed in the range of $x < 3.5$. The other is of an unknown origin, which is formed in the range of $x > 3.5$. The existence of two types of electron traps is likely, because the main component of the conduction band minimum (CBM) is varied from the Gd^{3+} 5d state to the Ga^{3+} 3s state with increasing x [3]. The Ga^{3+} 3s character in the CBM is common among $REGa_5O_{12}$ (RE=Y, Gd, and Lu). Therefore, it is expect that the electron trap in Ce:GGG is of the same origin as that in Ce:LuGG.

In the present study, we have measured infrared absorption spectra of undoped GGG, Ce:GGG, and Ce:LuGG crystals under irradiation and unirradiation with UV-light. The crystals of Ce:GGG and Ce:LuGG were grown from high-temperature melt by the micro pulling down method. The concentration of cerium ions was set 0.5 mol%. Experiment was performed at the beamline BL6B. The photon energy of the UV-light was 3.31 eV.

Figure 1 shows UV-induced infrared absorption spectra of (a) Ce:GGG and (b) Ce:LuGG crystals, measured at 12 K. The data were obtained by subtracting unirradated spectra from irradiated specta. In Fig. 1(a), a mid-infrared (MIR) band appears in the region below 4000 cm^{-1}. This band was enhanced by high-temperature annealing under hydrogen atmosphere. In undoped GGG, the MIR band disappeared completely, in contrast with undoped GAGG. These facts suggest that Ce^{3+} ions play an important role on the occurrence of the MIR band. In Fig. 1(b), one can see the MIR band below 4000 cm^{-1}, almost the same as that in Fig. 1(a). From this result, it is evident that electron traps in Ce:GGG and Ce:LuGG are associated with Ga^{3+} ions, but not with Gd^{3+} and Lu^{3+} ions.

As mentioned above, the CBM is mainly of Ga^{3+} 3s state. Generally, the electronic structure of electron traps reflects the CBM character. On this basis, Ga^{2+} ions are the most plausible candidate for electron traps in Ce:GGG and Ce:LuGG crystals. As suggested by Grigorjeva *et al*., the formation of such electron traps may require the perturbation by Ce^{3+} ions in the vicinity of them. This is supported by missing of the MIR band in undoped GGG. The enhancement of the MIR band by high-temperature annealing under hydrogen atmosphere is also explained by the increase in the concentration of Ce^{3+} ions. In order to clarify the origin of shallow electron traps responsible for teh MIR band, further data by spectroscopy experiment and theoretical calculations are needed.

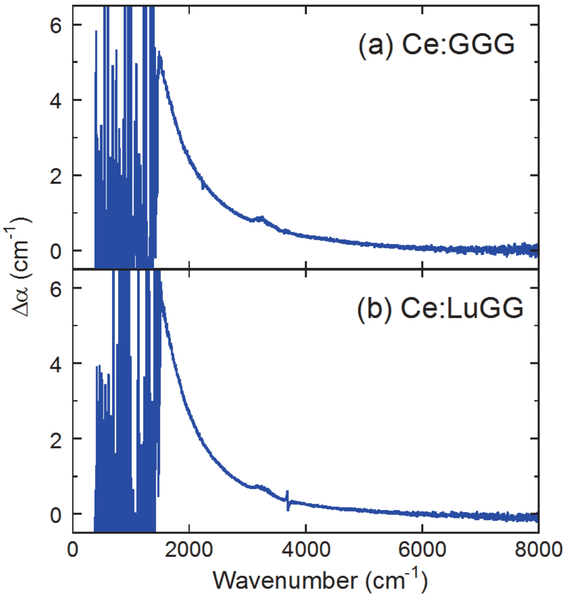

Fig. 1. UV-induced infrared absorption spectra of (a) Ce:GGG and (b) Ce:LuGG crystals measured at 12K.

[1] L. Grigorjeva *et al*., Opt. Mater. **75** (2018) 331.
[2] M. Kitaura *et al*., Appl. Phys. Lett. **113** (2018) 041906.
[3] P. Dorenbos, J. Lumin. **134** (2013) 310.

BL6B

Far-Infrared Reflective Analysis for Unipolar Fatigued Piezoelectric Ceramics

H. Nishiyama, D. Xie, R. Hasegawa, S. Maeda, Y. Ito, R. Kimata, N. Nagamatsu,
H. Hashimoto and K. Kakimoto
Graduate School of Engineering, Nagoya Institute of Technology, Nagoya 466-8555, Japan

Piezoceramics is widely used in the industry to convert electric energy to mechanical energy. As generally accepted, piezoelectric effect is caused by lattice expansion and domain orientation. The piezoelectric property deteriorates through repeated use, and some researchers attribute this cyclic fatigue to pinning of the domain structure. However, there have been no investigation for the change of the lattice vibration. Although far-infrared reflective (FIR) analysis reveals the lattice vibration and many researchers investigated for single crystal, nobody reports for ceramics due to its complexity of vibration-mode assignment. We have measured FIR spectra for lead-free piezoceramics including alkali niobate perovskite. In this study, we next investigated for $BaTiO_3$ which has already reported in single crystal [1].

$BaTiO_3$ ceramics was prepared by conventional solid state sintering. For comparing as-sintered and fatigued samples, unipolar cyclic E-field of 100 Hz with a maximum field of 3 kV/mm was applied up to 10^5 cycles. FIR measurement was conducted by a FT-IR spectrometer (Bruker, VERTEX 70v). A beam splitter and a detector used in this measurement were a Mylar 6 μm and a Si bolometer, respectively. Note that aperture diameter was 6 mm and then these were hundred thousands of grains in the spotted area.

Figure 1 shows lattice vibration modes of $BaTiO_3$ ceramics. From the FIR spectra shown in Figs. 1a and d, imaginary part of permittivity (Figs. 1b and e) was calculated with Drude-Lorentz model [2]. Infrared-active vibration modes of tetragonal perovskite are explained as $4E + 3A_1$, but we cannot fit with seven vibration modes for ceramics well because of not only the ratio of the polarization on its surface but also the distribution of the domain width, which can make a deviation of the locations due to internal stress caused by surrounding domain structure. This is why we used plenty number (23 waves) of Lorentz functions for fitting. Imaginary part of permittivity calculated with Drude-Lorentz model was fitted again with Voigt functions to separate overlapping of each peaks (Figs. 1c and f). According to the fitting result for crystal [1], these three peaks were identified *Last*, *Slater*, and *Axe* modes, respectively. Moreover, *Slater* mode in 10^5 cycles shifted higher by 32.2 cm^{-1} comparing to the as-sintered one. Here, *Slater* mode locates 34 cm^{-1} in a-axis and 280 cm^{-1} in c-axis oriented single crystal [1]. Considering a polarization ratio of as-sintered sample should be 2/3 for a-axis and 1/3 for c-axis due to its randomness, the amount of c-axis oriented domain should be increased. In other words, 10^5 cycles applied $BaTiO_3$ ceramics became more like c-axis oriented single crystal. In these ways, the change of lattice vibration for unipolar fatigued piezoceramics can be evaluated with FIR analysis.

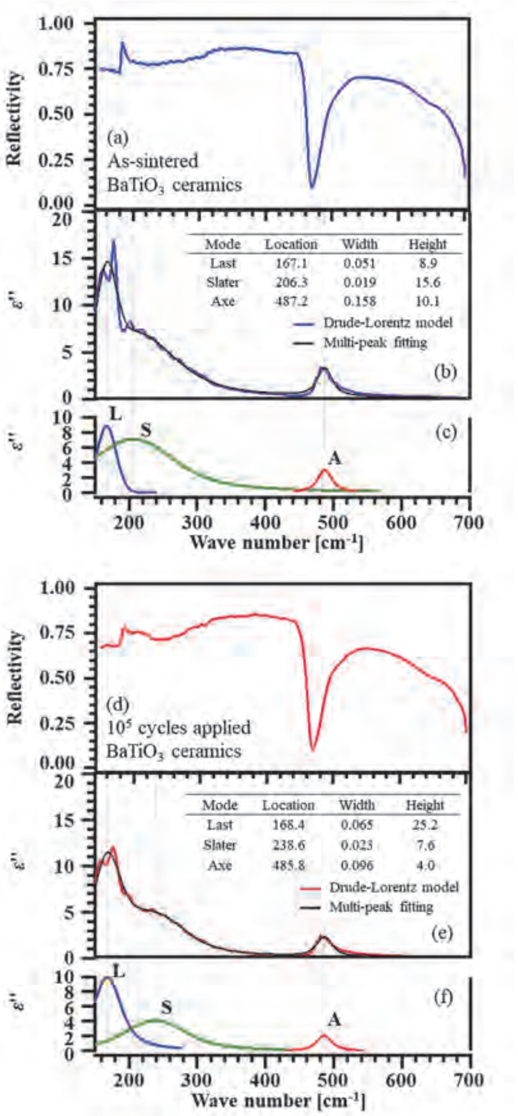

Fig. 1. Lattice vibration modes calculated from FIR spectra of $BaTiO_3$ ceramics.

[1] T. Hoshina *et al.*, Jpn. J. Appl. Phys. **53** (2014) 09PD03.

[2] H. Nishiyama *et al.*, UVSOR Activity Report 2016 **44** (2017) 84.

BL6B

Material Control by High Intensity THz Wave and Physical Property Evaluation by Infrared Spectroscopy

A. Irizawa
The Institute of Science and Industrial Research, Osaka University, Ibaraki 567-0047, Japan

Optical study is one of the most powerful techniques for investigating electronic states on solids. We can obtain direct of information about the electronic states, a band structure, a symmetry of crystal structure, and a dielectric response of materials. In view of experimental affinity, the optical study is extremely compatible with extreme conditions such as low temperature, high magnetic field, and high pressure, excited state by pumping light, and their combinations. The observation of electronic states can be concluded with only optical operations in contrast with e.g. photoemission spectroscopy. Additionally small sample area and/or convoluted mixed-phase have need of microscopic technique, in such view optical study including infrared spectroscopy is one of the best choice for determining electronic states of materials. Beamline 6B in UVSOR is adjusted for the investigations for optical study in a low-energy region of infrared, i.e. FIR and MIR. In this report, we have performed the optical transmittance measurements in the longest wavelength region. The introduced dry-air system is investigated by check the absorption lines of gas components in the air.

The experiments are performed by using Michelson-type interferometer in MIR region with infrared microscope. Before this experiment, this system was operated in the air without closed atmospheric condition. Otherwise we can get the best condition by using N_2 gas flow with rather quantity, one compressed gas cylinder for 2 days. This time, active-dry air system has been installed for this beamline and the performance was checked by IR spectroscopy. Figure 1 shows the spectra of black-body light source with the atmospheric conditions of open in the air, flowing dried air, and flowing N_2 gas from compressed cylinder with a fine resolution of Δ=1 cm^{-1}. Between 1000 and 2000 cm^{-1}, 3000 and 4000 cm^{-1}, and 5000 and 6000 cm^{-1}, there shows clustered fine absorption lines of the vapor in the air. The atmospheric condition of humidity was around 15 % in the beamline which was not wet condition, but the MIR light was strongly absorbed by vapor in these regions. In case of dried air flow and N_2 gas flow are better than this, except for the absorption line of CO_2 around 2300 cm^{-1}, the obtained light source spectra are applicable for estimating the ratio of spectra, i.e. absorptance, transmittance, and reflectance. This improvement must be the advantage for microscopic spectroscopy under extreme conditions including the experiments using organic materials that have absorption lines in an infrared region.

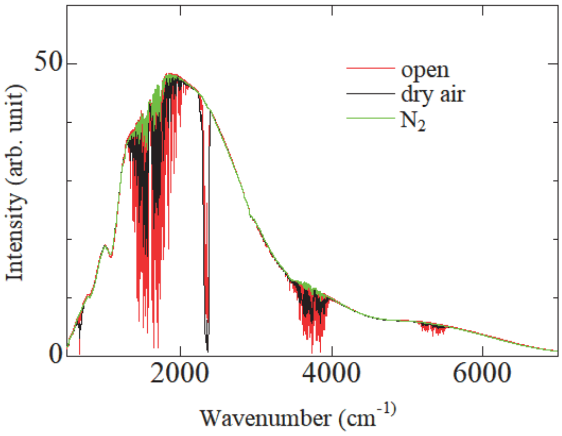

Fig. 1. Spectra of light source with different atmospheric conditions.

BL7U

High-resolution ARPES Study of Nodal Fermion Materials

T. Sato[1,2], Z. Wang[3], K. Nakayama[1], S. Souma[2,4], D. Takane[1], Y. Nakata[1], K. Hori[1],
H. Oinuma[1], T. Takahashi[1,2,4] and Y. Ando[2]
[1]*Department of Physics, Tohoku University, Sendai 980-8578, Japan*
[2]*Physics Institute II, University of Cologne, 50937 Köln, Germany*
[3]*Center for Spintronics Research Network, Tohoku University, Sendai 980-8577, Japan*
[4]*WPI Research Center, Advanced Institute for Materials Research, Tohoku University, Sendai 980-8577, Japan*

The search for new types of topological materials hosting nodal fermions is one of the emergent topics in condensed-matter physics. One of the effective strategies to search for nodal fermions is to utilize the point-group symmetries of crystal, i.e., mirror reflection, rotation, and inversion symmetries in addition to time-reversal symmetry, as highlighted by the discovery of topological crystalline insulators hosting the surface nodal fermions protected by mirror reflection symmetry. Recent theoretical studies also predicted that nonsymmorphic space-group symmetry combining point-group symmetry and the fractional translation further enriches the category of nodal fermions. This is demonstrated by the prediction/observation of nodal loops protected by the glide mirror (mirror reflection plus translational) symmetry [1-3], as well as the Weyl nodes in trigonal Te and the nodal lines in ZrSiS, both of which are protected by the screw (rotation plus translational) symmetry [2, 4, 5].

Recently, it was theoretically proposed that the layered ternary telluride Ta_3SiTe_6 hosts nodal fermions protected by nonsymmorphic glide mirror symmetry [6]. This material crystallizes in the orthorhombic structure with the space group No. 62 (*Pnma*). As shown in Fig. 1(a), the basic structural unit of Ta_3SiTe_6 is a Te trigonal prismatic slab with Ta atoms located around the center of this prism. Each unit cell contains two such slabs which are overlaid with each other by the inversion operation. First-principles band-structure calculations [6] show that, when the spin-orbit coupling (SOC) is neglected, Ta_3SiTe_6 displays a fourfold-degenerate nodal line on the SR line in the bulk Brillouin zone [see Fig. 1(b)] due to the protection by glide mirror symmetry. It is also suggested that when the SOC is included, the fourfold degeneracy is slightly lifted and as a result hourglasslike dispersions appear. To examine such intriguing predictions, it is highly desirable to experimentally establish the electronic band structure of Ta_3SiTe_6.

In this study, we performed low-energy high-resolution ARPES measurements of Ta_3SiTe_6 at BL7U, and found a signature of Dirac-like band dispersion protected by the glide mirror symmetry.

Figure 1(c) shows a representative ARPES intensity in the valence-band region of Ta_3SiTe_6 measured at T = 40 K with $h\nu$ = 26 eV photons. We find several highly dispersive bands within 1 eV of the Fermi level. These bands mainly originate from the Ta 5*d* orbitals hybridized with the Te 4*p* orbitals. We have also performed detailed three-dimensional *k*-space mapping by tuning photon energy and observed the band degeneracy that which supports the existence of nodal fermions predicted by the calculation.

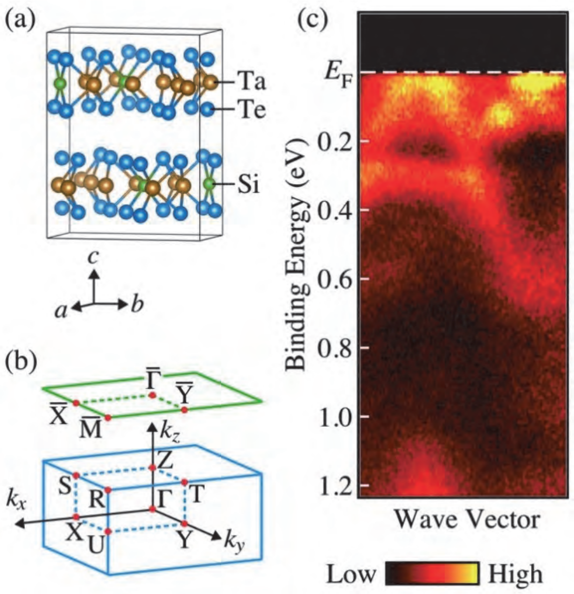

Fig. 1. (a) Crystal structure of Ta_3SiTe_6. (b) Bulk orthorhombic BZ (blue) and corresponding surface BZ projected onto the (001) plane (green). (c) ARPES intensity as a function of binding energy and wave vector measured at T = 40 K with linearly polarized 26-eV photons.

[1] Q. Xu *et al.*, Phys. Rev. B **92** (2015) 205310.
[2] L. M. Schoop *et al.*, Nat. Commun. **7** (2016) 11696.
[3] D. Takane *et al.*, Phys. Rev. B **94** (2016) 121108(R).
[4] C. Chen *et al.*, Phys. Rev. B **95** (2017) 125126.
[5] K. Nakayama *et al.*, Phys. Rev. B **95** (2017) 125204.
[6] S. Li *et al.*, Phys. Rev. B **97** (2018) 045131.

BL7U

Electronic State of the Two-dimensional Transition Metal Chalcogenide Ferromagnets Studied by ARPES

M. Suzuki[1], B. Gao[2], K. Koshiishi[1], C. Lin[1], Y. X. Wan[1], M. Kobayashi[3,4], S. Ideta[5], K. Tanaka[5], S.-W. Cheong[2] and A. Fujimori[1]
[1]Department of Physics, The University of Tokyo, Tokyo 113-0033, Japan
[2]Rutgers Center for Emergent Materials and Department of Physics and Astronomy, Rutgers University, Piscataway, New Jersey 08854, USA
[3]Center for Spintronics Research Network, The University of Tokyo, Tokyo 113-0033, Japan
[4]Department of Electrical Engineering and Information Systems, The University of Tokyo, Tokyo 113-8656, Japan
[5]UVSOR Synchrotron Facility, Institute for Molecular Science, Okazaki 444-8585, Japan

Since the discovery of graphene, there has been tremendous interest in the development of new two-dimensional (2D) materials and their functionalities [1]. The materials have layered crystal structures and the layers are bonded to each other through van der Waals (vdW) forces. In addition to graphene and transition-metal dichalcogenides, vdW ferromagnets have recently attracted much attention as candidate materials for new types of spintronic devices.

$Cr_2Ge_2Te_6$ (CGT) and $Cr_2Si_2Te_6$ (CST) are representative vdW ferromagnets, and along with other vdW ferromagnets, e.g., CrI_3, their electronic and magnetic properties have been studied theoretically and experimentally [2, 3]. The magnetism of CGT nanosheets shows soft behaviors and is well described by the 2D Heisenberg model [4].

To unveil the origin of the ferromagnetism in 2D materials, understanding the physical properties from the electronic structure points of view is important. For both fundamental understanding and potential applications of 2D vdW ferromagnets, the knowledge of the electronic structure of CGT related to the ferromagnetism is indispensable. Therefore, we have conducted angle-resolved photoemission spectroscopy (ARPES) in order to clarify the electronic structure of CGT and CST.

Figures 1(a) and 1(b) show ARPES spectra of CGT obtained by using p- and s-polarizations. The center of the cuts corresponds to the Γ point. One can see that a hole-like band centered at Γ is located at ~0.2 eV below the Fermi level and the valence-band maximum does not reach the Fermi level, indicating a semiconducting property, consistent with the electric transport properties [2, 5]. In addition, a similar hole band exists at ~0.5 eV below the upper hole band. Photoemission spectra of CGT are shown in Fig. 1(c). Difference between s- and p-polarizations has been clearly observed. Especially, the position of the main peak around 2 eV is shifted between the two polarizations. Since Cr 3d electrons are supposed to form partial density of states (PDOS) around the binding energy of ~2 eV, according to first-principle calculation, we consider that the PDOSs of different Cr 3d orbitals have been observed.

On the other hand, for CST, we could not observe any differences as shown in Fig. 1(d). Moreover, its spectral line shape is completely different from that of CGT. However, it is not natural that electronic states of the Cr 3d electrons is dramatically changed by only substituting Si for Ge. Therefore, we consider that the results for CST maybe due to extrinsic effects.

In order to reveal the origin of the ferromagnetism in these materials, further studies are required.

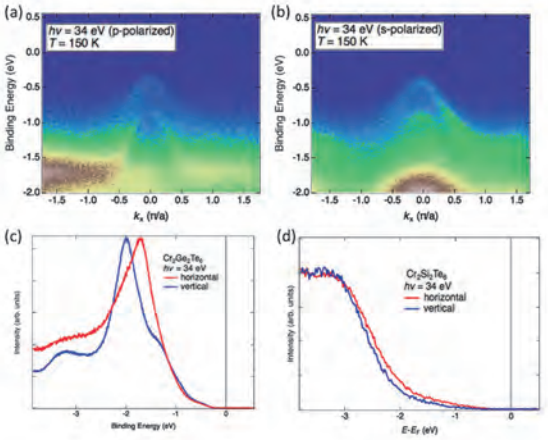

Fig. 1. ARPES spectra of .van der Waals ferromagnets. (a), (b) Energy-momentum plots of $Cr_2Ge_2Te_6$ using p- and s-polarizations. (c) Comparison of the valence-band photoemission spectra of $Cr_2Ge_2Te_6$ between p- and s-polarizations. (d) Photoemission spectra of the valence band of $Cr_2Si_2Te_6$.

[1] K. S. Novoselov *et al*., Science **306** (2004) 666.
[2] X. Zhang *et al*., Jpn. J. Appl. Phys. **55** (2016) 033001.
[3] G. T. Lin *et al*., Phys. Rev. B. **95** (2017) 245212.
[4] C. Gong *et al*., Nature **546** (2017) 265.
[5] H. Ji *et al*., J. Appl. Phys. **114** (2013) 114907.

BL7U

Angle-resolved Photoemission Study of Ullmannite NiSbS with the Cubic Chiral Crystal Structure

T. Ito[1,2], T. Hosoya[2], M. Nakatake[3], S. Ideta[4,5], K. Tanaka[4,5], M. Kakihana[6], D. Aoki[7], A. Nakamura[7], T. Takeuchi[8], H. Harima[9], M. Hedo[10], T. Nakama[10] and Y. Onuki[10]
[1]*Nagoya University Synchrotron radiation Research center (NUSR), Nagoya University, Nagoya 464-8603, Japan*
[2]*Graduate School of Engineering, Nagoya University, Nagoya 464-8603, Japan*
[3]*Aichi Synchrotron Research Center, Seto 489-0965, Japan*
[4]*UVSOR Synchrotron Facility, Institute for Molecular Science, Okazaki 444-8585, Japan*
[5]*The Graduate University for Advanced Studies, Okazaki 444-8585, Japan*
[6]*Graduate School of Engineering and Science, University of the Ryukyus, Okinawa 903-0213, Japan*
[7]*Institute for Materials Research, Tohoku University, Ibaraki 311-1313, Japan*
[8]*Low Temperature Center, Osaka University, Osaka 560-0043, Japan*
[9]*Graduate School of Science, Kobe University, Kobe 657-8501, Japan*
[10]*Faculty of Science, University of the Ryukyus, Okinawa 903-0213, Japan*

Non-centrosymmetric compounds have attracted much attention due to their interesting phenomena relating with inversion symmetry breaking. The ullmannite type NiSbS with the non-centrosymmetric cubic chiral structure has recently been suggested to be a possible candidate of Wely semimetal [1]. Indeed, split Fermi surface topologies reflecting the cubic chiral crystal structure and the spin-orbit interactions have been reported [2]. In this study, we have performed angle-resolved photoemission spectroscopy (ARPES) on NiSbS to directly investigate the electronic band structure of this system.

ARPES measurements were performed at the UVSOR-III BL7U. Data were acquired at $T = 25$ K with $h\nu = 32$ eV which enables us to trace around the XMR plane with inner potential of V_0=24.7 eV estimated from the photon energy dependent measurement (not shown). Clean surfaces were obtained by *in situ* cleaving on (001) plane.

Figure 1(a) shows the obtained Fermi surface (FS) image on the XMR plane compared with the reported FS topologies [2]. The band structure along the XM line is shown in Fig. 2 together with the band calculation [2]. From the present ARPES study, it has been found that the electronic structure of NiSbS seems to be well reproduced by the calculation along the XMR plane. For example, an electron pocket around the X point which touches the Fermi level and then disperse to 0.5 eV around the R point has clearly been observed in Fig. 2. On the other hand, we found non-negligible contributions of the ΓXM plane and the surface states. The bands due to electron (hole) -like FS branch α (ε) appear and merge with the bands along the XR line. This might originate from a large k_z-broadening effect [3]. In addition, narrow dispersion around 0.5 eV should be assigned as surface states. The results suggest the applicability of ARPES to pursue the Weyl points and node features originating in the chiral crystal structure with great care about bulk sensitivity as well as spin (orbital) –polarizations at the electronic structure.

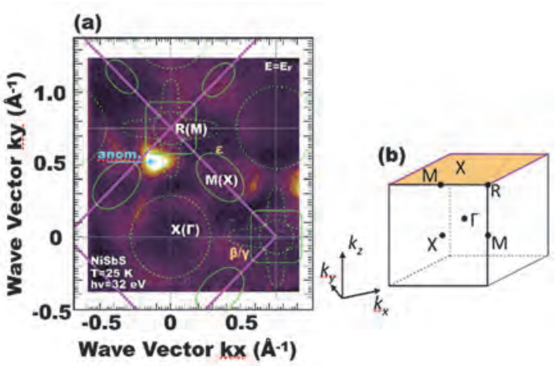

Fig. 1. (a) Fermi surface (FS) image on the XMR plane of NiSbS. Solid and dashed green lines are FS topologies on the XMR and ΓXM plane reported in ref. [2], respectively. (b) Cubic Brillouin zone shown with the momentum axis.

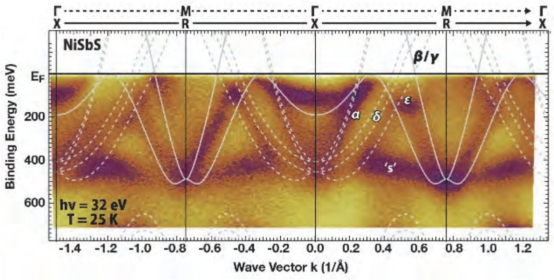

Fig. 2. Band structure image along the XM line of NiSbS. Solid and dashed lines are band calculation along the XR and ΓM lines, respectively [2].

[1] A. Furusaki, Sci. Bulletin **62** (2017) 788.
[2] M. Kakihana *et al*., J. Phys. Soc. Jpn. **84** (2015) 084711.
[3] T. Mitsuhashi *et al*., Phys. Rev. B **94** (2016) 125148.

BL7U, BL5U

Direct Observation of the Energy Gap Generation of Ruthenium mono-arsenide RuAs

Y. Nakajima[1], T. Nakamura[1], Y. Ohtsubo[2,1], H. Kotegawa[3], H. Sugawara[3], H. Tou[3]
and S. Kimura[1,2]
[1]*Department of Physics, Osaka University, Toyonaka 560-0043, Japan*
[2]*Graduate School of Frontier Biosciences, Osaka University, Suita 565-0871, Japan*
[3]*Department of Physics, Kobe University, Kobe 657-8501, Japan*

Ruthenium mono-pnictides Ru*Pn* (*Pn* = P, As, Sb) have been recently noted in the relation to iron pnictide superconductors. Actually, Rh-doped RuP and non-doped RuSb become superconductor at low temperatures [1]. Other interesting properties are the charge-density wave in RuP [2] and the metal-to-insulator transition (MIT) in RuAs [1]. These phenomena are believed to be related to the origin of the superconductivity, but it is under debate at present [3].

RuAs, which is one of the Ru*Pn* family, is being well investigated. The MIT originates from the formation of a superlattice of 3×3×3 of the original unit cell [4]. However, the origin of the superlattice formation has not been clarified yet. One possibility is the electronic instability, and the other the lattice distortion owing to the zigzag-chain of Ru site. To clarify the origin of MIT, we are investigating the electronic and the phonon structure as a function of temperature.

According to the electronic band calculations, the density of states (DOS) within the energy of about 0.2 eV from the Fermi level (E_F) decreases in the low-temperature insulating (LT) phase from the high-temperature metallic (HT) phase as shown in Fig. 1, even though the finite DOS at E_F still remains in the LT phase, i.e., no energy gap is expected. However, the optical conductivity spectra as well as the electrical resistivity have suggested that a clear energy gap appears in the LT phase [5]. Then, we have performed the temperature-dependent angle-integrated photoelectron spectroscopy (AIPES) of RuAs to investigate whether the energy gap can be realized at low temperatures or not.

Figure 2 shows the temperature-dependent AIPES spectra divided by the Fermi-Dirac distribution functions for each temperature, which can be compared with DOS. The intensity at E_F at 280 K (in the HT phase) is almost flat suggesting the constant DOS near E_F, but it slightly decreases with decreasing temperature to 13 K in the LT phase. The energy at which the divergence starts with decreasing temperature is about 0.15 eV, which corresponds to the energy where DOS changes from the HT phase to the LT phase. Therefore, the change of electronic structure was clearly observed in the AIPES spectra.

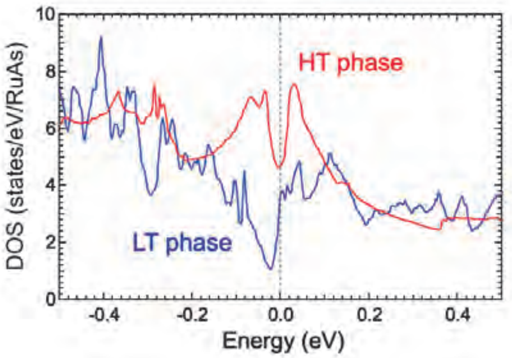

Fig. 1. Density of states (DOS) of RuAs as high-temperature (HT) and low-temperature (LT) phases. The zero energy was set as the Fermi level (E_F). The intensity in the energy region within 0.15 eV below and above E_F decreases from the HT phase to the LT phase, but finite DOS remains even at the LT phase.

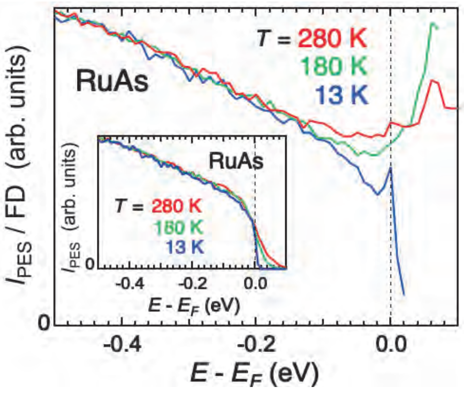

Fig. 2.
Temperature-dependent angle-integrated photoelectron spectra of RuAs divided by the Fermi-Dirac distribution functions (FDs) for each temperature convoluted with a Gaussian function of σ of 10 meV. The excitation photon energy was 20 eV. (Inset) Same as the main figure but without the division of FDs.

[1] D. Hirai *et al.*, Phys. Rev. B **85** (2012) 140509(R).
[2] R. Y. Chen *et al.*, Phys. Rev. B **91** (2015) 125101.
[3] Y. Kuwata *et al.*, J. Phys. Soc. Jpn. **87** (2018) 073703.
[4] H. Kotegawa *et al.*, Phys. Rev. Mater. **2** (2018) 055001.
[5] Y. Nakajima *et al.*, UVSOR Activity Report 2017 **45** (2018) 84.

BL7U

Measurement for the Dispersion of the Excited States in NbSe$_2$ by Using the Photon-Energy-Dependent ARPES

S. Tanaka[1] and K. Ueno[2]

[1]*The Institute of Industrial and Scientific Research, Osaka University, Ibaraki 567-0046, Japan*
[2]*Department of Chemistry, Graduate School of Science and Engineering Saitama University, Saitama 338-8570, Japan*

The electronic-excitation dynamics of the material is a key issue for understanding and developing the functional optical device. Transition-metal-dichalcogenides (TMDC) attracts interests of many researchers because of its unique 2D character. Here, we report the photon-energy dependent angle-resolved photoelectron spectroscopy (ARPES) of NbSe$_2$(2H), which is one of the most studied TMDC, and examine the band-dispersion of the excited state.

All the experiments were carried out at BL7U of the UVSOR-III. The NbSe$_2$ sample was cleaved in UHV and the photon-energy-dependent ARPES was measured at 10K. The photon intensity was calibrated by the use of the photodiode.

Figure 1 show the two-dimensional photoelectron intensity map of the normal emission as functions of the binding energy and photon energy. Peaks at the binding energy around -1eV clearly show enhancements in intensity at the photon energy of about 9.6eV. This can be attributed to the resonant enhancement when the photon energy matches the energy-difference between the initial (occupied) and final (empty) bands of the photoexcitation. Therefore, the energy position of the excited (empty) bands can be deduced from the photon-energy-dependent measurement since the initial (occupied) band can be determined from the ordinal (non-resonant) ARPES measurement. The Fig. 2(a) shows the ARPES spectrum along the Γ-K line taken at hν=11.4eV. We focus the two bands indicated as “upper” and “lower” bands in the figure, and measured their intensity as a function of the photon energy. Then the energy is converted as $E_f(k)=h\nu+E_B(k)$, where $E_f(k)$ denotes the final-state-energy at a specific electron momentum of k, $h\nu$ the photon energy and $E_B(k)$ the binding energy in the negative scale at k, which can be derived from the dispersion curves [solid lines in Fig.2 (a)]. The results are shown for several momenta in Figs 2(b) and (c) for upper and lower bands, respectively. The intensity distributions can be well represented by the Lorentzian curves whose peak positions change with the electron momenta. These peak positions should indicates the position of the excited (empty) bands into which the photo-excitation occurs from the upper and lower bands in Fig. 2(a). Figures 2(d, e) show intensity maps of the photoelectron peaks as functions of the final state energy with respect the Fermi level and the electron momentum. The peak positions obtained in Figs. 2(b, c) are shown as solid lines, and these are dispersions of the excited bands of NbSe$_2$.

These experimental results are well explained by the comparison to the 1st principles band calculation including the analysis of the photoexcitation selection rules based on the band symmetry.

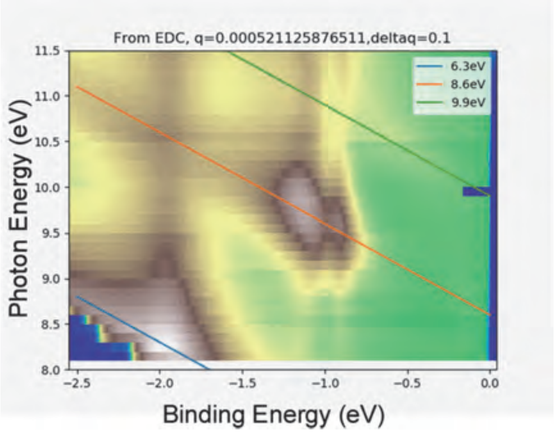

Fig. 1. Photoelectron intensity map of NbSe$_2$ as functions of photon energy (vertical axis) and binding energy (horizontal axis). Lines indicate the position of the same final state energies.

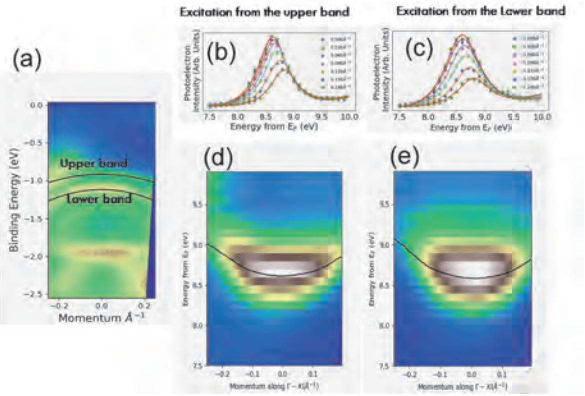

Fig. 2. (a) APRES map of the NbSe$_2$ at hν=11.4eV; (b, c) the intensity of the bands indicated in Fig. 2(a) as as a function of the photon energy after the energy conversion; (d, e) the dispersion of the excited state obtained from (b, c).

BL7U

Temperature Dependence of the Kondo Resonance Peak in Photoemission Spectra of Rare-earth Compound $YbMgCu_4$

K. Morikawa[1], H. Shiono[1], H. Sato[2], S. Ideta[3], K. Tanaka[3], T. Zhuang[4],
K. T. Matsumoto[4], K. Hiraoka[4] and H. Anzai[1]
[1]*Graduate School of Engineering, Osaka Prefecture University, Sakai 599-8531, Japan*
[2]*Hiroshima Synchrotron Radiation Center, Hiroshima University, Higashi-Hiroshima 739-0046, Japan*
[3]*UVSOR Synchrotron Facility, Institute for Molecular Science, Okazaki 444-8585, Japan*
[4]*Graduate School of Science and Engineering, Ehime University, Matsuyama 790-8577, Japan*

In rare-earth compounds, the interaction between itinerant conduction and localized-4*f* electrons (*c*-*f* hybridization) leads to a renormalized quasiparticle. Such a heavy-fermion behavior is characterized by a resonance peak appearing at the energy scales of the Kondo temperature T_K in electronic excitation spectra. For Yb compounds, the spin-orbit split Yb^{2+} $4f_{7/2}$ state is interpreted as the Kondo resonance peak [1]. The Yb^{2+} $4f_{7/2}$ state near the Fermi level (E_F) will provides important clues to the possible mechanism of the heavy-fermion states.

$YbMgCu_4$ with C15b-type structure is known as a heavy fermion compound with the electronic specific heat coefficient $\gamma \sim 62$ mJ/K^{2}mol [2]. The Kondo temperature is estimated to be $T_K \sim 855$ K from the magnetic susceptibility measurements [2]. Previous photoemission spectroscopy measurements presented a broad Yb^{2+} $4f_{7/2}$ peak at ~240 meV, which deviate considerably from the value of Kondo temperature [3]. To detect the heavy-fermion states in $YbMgCu_4$, it is essential to identify the Yb 4*f* state near E_F.

Here, we report on a study of the Kondo resonance peak in photoemission spectra of $YbMgCu_4$. The experiments were performed at BL7U of UVSOR. The energy resolution was 16 meV. The samples were cleaved *in situ* and maintained under ultrahigh vacuum (8×10^{-9} Pa) during the measurements.

Figure 1(a) shows the valence-band spectra at $T = 8$ K. The spin-orbit splitting of the Yb^{2+} $4f_{7/2}$ and Yb^{2+} $4f_{5/2}$ states are observed at $|\omega| \sim 0.07$ eV and 1.36 eV, respectively [3, 4]. The observability of the $4f_{7/2}$ state near E_F is substantially improved by slightly increasing the photon energy from those used in previous studies, $h\nu \sim 21$ eV [3].

Figure 1(b) shows the temperature dependence of the photoemission spectra near E_F. We found that a sharp peak of the $4f_{7/2}$ state survives at even higher temperature, $T \sim 190$ K, and the peak energy remains unchanged. We determined the peak energies and plotted them as a function of temperature in Fig. 1(c). The peak energy slightly decreases with decreasing temperature from $T = 187$ K to 122 K, and then tends to saturate at low temperatures. The peak energies extrapolated to zero temperature is estimated to be ~ 69 meV. This value corresponds to $T_K \sim 805$ K, which is approximately consistent with T_K reported from the magnetic susceptibility measurements [2]. Therefore, the observed $4f_{7/2}$ peak can be assigned to the Kondo resonance peak in $YbMgCu_4$. This consistency implies that the observed $4f_{7/2}$ state in this study is indeed responsible for the heavy-fermion behavior of $YbMgCu_4$.

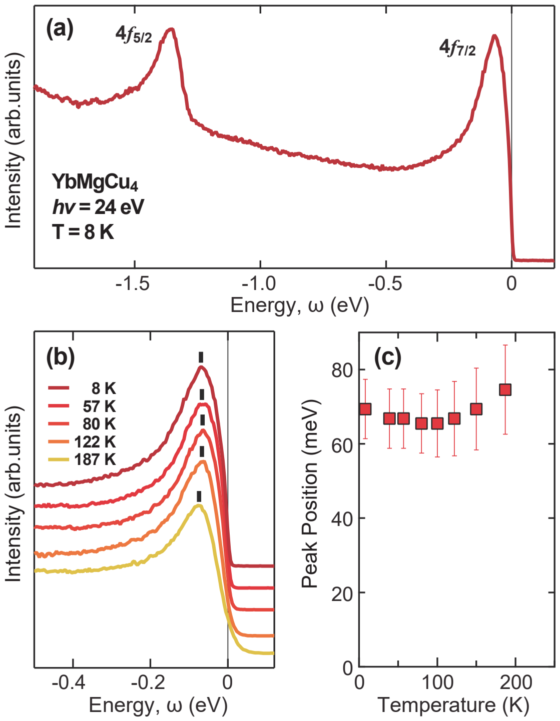

Fig. 1. (a) Valence-band spectra of $YbMgCu_4$ taken with photon energy $h\nu = 24$ eV at $T = 8$ K. (b) Temperature dependence of the valence-band spectra near E_F. Vertical bars indicate the peak positions. (c) Energy shift of the Yb^{2+} $4f_{7/2}$ peak in panel (b). The error bars of energies derived from the uncertainty of the peak positions.

[1] R. I. R. Blyth *et al.*, Phys. Rev. B **48** (1993) 9497.
[2] J. L. Sarrao *et al.*, Phys. Rev. B **59** (1999) 6857.
[3] H. Sato *et al.*, J. Synchrotron Rad. **9** (2002) 229.
[4] F. Reinert *et al.*, Phys. Rev. B **58** (1998) 12808.

BL7U

ARPES Study of Novel Topological Material Candidates

H. Oinuma[1], S. Souma[2,3], D. Takane[1], T. Nakamura[1], K. Hori[1], R. Tsubono[1], K. Nakayama[1],
K. Sugawara[1,2], T. Takahashi[1,2,3], A. Ochiai[1] and T. Sato[1,2]
[1]*Department of Physics, Tohoku University, Sendai 980-8578, Japan*
[2]*Center for Spintronics Research Network, Tohoku University, Sendai 980-8577, Japan*
[3]*WPI Research Center, Advanced Institute for Materials Research, Tohoku University, Sendai 980-8577, Japan*

Topological insulators (TIs) are a novel quantum state of matter where gapless edge or surface states (SSs) appear within a bulk-band gap inverted by strong spin-orbit coupling. The SSs of three-dimensional (3D) TIs are characterized by the linearly dispersive Dirac-cone band that can be viewed as a sea of Dirac fermions whose massless nature is guaranteed by the time-reversal symmetry. The search for new topological materials is currently a hot topic in condensed-matter physics.

Recently, it was predicted from the first-principles band-structure calculations [1] that lanthanum (La) monopnictide with rock-salt structure LaX (X = N, P, As, Sb, and Bi) becomes either topological Dirac semimetal (for X = N) or 3D TI (for X = P, As, Sb, and Bi) with Dirac fermions at the surface, due to the band inversion at the X point of bulk fcc Brillouin zone (BZ) [see Fig. 1(a)]. While rare-earth monopnictide RX (R: rare earth) was intensively studied in 1980-90's in relation to heavy-fermion physics, this theoretical proposal [1] renewed the interest for RX in topological aspects and triggered intensive transport, spectroscopic, and theoretical studies. The occurrence of magnetic order in some RX compounds, e.g., cerium (Ce) monopnictides CeX, also provides a rare opportunity to investigate the interplay between topological properties and magnetism, which has largely been left unexplored because of the absence of suitable material platform. Therefore, experimental elucidation of the topological properties in RX compounds is highly desired.

In this study, we performed high-resolution angle-resolved photoemission spectroscopy (ARPES) of RX family. By utilizing low photon energy and energy-tunable characteristics of BL7U, we determined the bulk and surface band structures and investigated topological properties.

Figures 1(b) and 1(c) show the ARPES spectra measured along a cut crossing the $\bar{\Gamma}$ point of the surface BZ and the corresponding intensity plot, respectively, obtained in the paramagnetic state of CeBi. We find that at least three hole-like bands cross the Fermi level (E_F) near the $\bar{\Gamma}$ point. Two of them show parabolic dispersions and attributed to the topmost bulk valence bands with the Bi 6p orbital character, consistent with our recent soft-x-ray ARPES measurements on RX family [5]. The rest hole-like band that shows a linear dispersion is assigned as the topological Dirac-cone SSs with the Dirac point in the close vicinity of E_F. By performing high-resolution measurements at low temperatures, we searched for magnetism-induced changes in the topological SSs, and also investigated the topological property of other RX compounds.

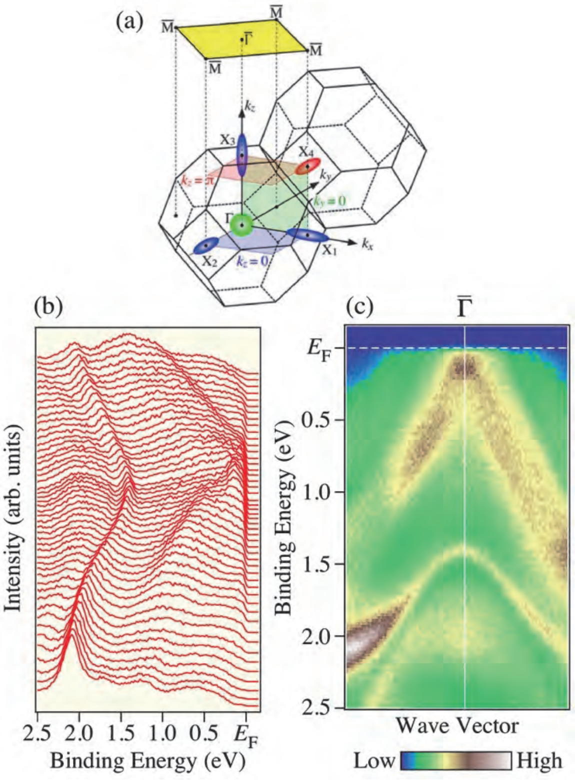

Fig. 1. (a) Bulk and surface BZs with the schematic bulk Fermi surfaces at the Γ point (green) and the X point (red and blue). (b) ARPES spectra measured along a momentum cut crossing the $\bar{\Gamma}$ point of the surface BZ with $h\nu$ = 22 eV. (c) ARPES intensity plot of (b) as a function of binding energy and wave vector.

[1] M. Z. Hasan and C. L. Kane, Rev. Mod. Phys. **82** (2010) 3045.
[2] X.-L. Qi and S.-C. Zhang, Rev. Mod. Phys. **83** (2011) 1057.
[3] Y. Ando, J. Phys. Soc. Jpn. **82** (2013) 102001.
[4] M. Zeng *et al.*, arXiv:1504.03492.
[5] H. Oinuma *et al.*, Phys. Rev. B **96** (2017) 041120(R).

BL7U

Electronic Structure of Underdoped Triple-layer Cuprate $Bi_2Sr_2Ca_2Cu_3O_{10+\delta}$

S. Ideta[1,2], S. Adachi[3], N. Sasaki[3], S. Yamaguchi[3], T. Watanabe[3] and K. Tanaka[1,2]
[1]*National Institutes of Natural Science, Institute for Molecular Science, Okazaki, 444-8585, Japan*
[2]*The Graduate University for Advanced Studies (SOKENDAI), Okazaki, 444-8585, Japan*
[3]*Graduate School of Science and Technology, Hirosaki University, Hirosaki 036-8561, Japan*

To understand the mechanism of high-T_c superconductivity in cuprates is one of the crucial issues and the energy gap seen in the superconducting (SC) and normal states is believed to be an important piece of evidence for the non-BCS behavior of the SC transition for the underdoped regime in the high-T_c cuprate superconductors. Two different representative energy gaps are present in the SC and normal states, namely, the SC gap and pseudogap in cuprate superconductors [1-3]. Origin of the pseudogap has been considered that it is related to the superconductivity or a phenomenon distinct from superconductivity, and sheds light on its nature to elucidate the mechanism of high-T_c superconductivity.

Triple-layer Bi-based cuprate superconductor, $Bi_2Sr_2Ca_2Cu_3O_{10+\delta}$ (Bi2223), which shows the highest T_c (110 K) among the Bi-based cuprates, has two inequivalent CuO_2 planes with different hole carrier [4-6]. In this study, we have investigated the energy gap anisotropy and we found an as-yet-unknown energy gap with a node which is neither the general pseudogap nor the nodeless energy gap in underdoped regime. We observed two bands corresponding to the outer and inner CuO_2 planes and the hole carrier deduced from the IP and OP FSs suggests that IP is almost zero carrier and OP is underdoped.

High-quality single crystals of underdoped $Bi_2Sr_2Ca_2Cu_3O_{10+\delta}$ (UD Bi2223, T_c = 80 K) were grown by the TSFZ method. Underdoped Bi2223 samples were successfully obtained in the two-step annealing in order to control their doping levels [7]. ARPES experiments were carried out at BL7U of UVSOR-III Synchrotron. Clean sample surfaces were obtained for the ARPES measurements by cleaving single crystals *in-situ* in an ultrahigh vacuum better than 6×10^{-9} Pa. The measurements were performed at 12 K and 95 K.

Figure 1(a) shows the ARPES spectra of UD Bi2223. ARPES intensity mapping integrated within ±5 meV centered at E_F is shown taken at $h\nu = 18$ eV. Two Fermi surfaces (FSs) are designated as the inner (IP) and outer (OP) CuO_2 planes reported as previous ARPES studies [4, 5]. The FS momentum (k_F) positions for IP (blue dots) and OP (red dots) have been determined by the peak position of momentum- distribution curves in the normal state as shown in Fig. 1(b). The hole carrier for IP and OP deduced from the FS area are 0-2% and 8-10%, respectively, and hence, surprisingly the inner CuO_2 plane is almost non-doping. To see the momentum dependence of the pseudogap and the SC gap, the energy gap is estimated from the peak position of the energy-distribution curves and plotted as functions of a simple d-wave order parameter $|\cos(k_xa) - \cos(k_ya)|/2$ [Figs. 1(c) and 1(d)]. As clearly seen in Fig. 1(c), the energy gap for IP is relatively temperature-independent across T_c and the FS only remains near node above T_c as well as that in the SC state. On the other hand, in Fig. 1(d), the energy gaps for OP show a d-wave-like evolution at 12 K and close the gap and have a Fermi arc around the nodal region at 95 K. To evaluate the validity of the present finding, it is highly desired to demonstrate a further systematic experimental study in the near future.

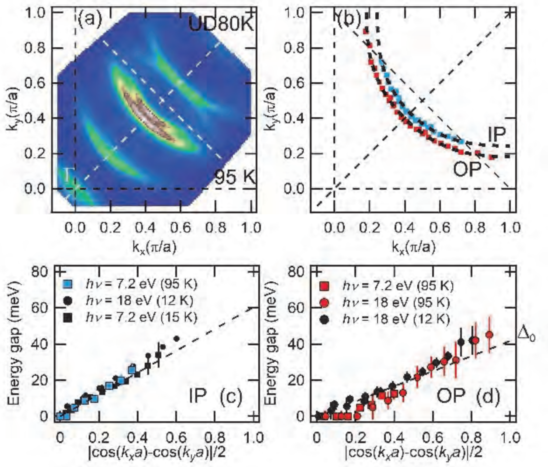

Fig. 1. Electronic structure of underdoped Bi2223. (a) ARPES intensity plots taken at T = 95 K. (b) Fermi momentum plots on the outer (OP) and inner (IP) Fermi surfaces. (c), (d) Temperature dependence of the energy gap for OP and IP plotted as functions of the d-wave order parameter.

[1] D. S. Marshall *et al.*, Phys. Rev. B **76** (1996) 4841.
[2] A. G. Loeser *et al*, Science **273** (1996) 325.
[3] H. Ding *et al.*, Nature (London) **382** (1996) 51.
[4] S. Ideta *et al.*, Phys. Rev. Lett. **104** (2010) 227001.
[5] S. Ideta *et al.*, Phys. Rev. B **85** (2012) 104515.
[6] S. Ideta *et al.*, Physica C **470** (2010) S14.
[7] S. Adachi *et al.*, Physics Procedia **65** (2015) 53.

BL7B

Photoluminescence and Scintillation of $Rb_{1-x}Cs_xCaCl_3$

K. Takahashi[1], M. Koshimizu[1], Y. Fujimoto[1], T. Yanagida[2] and K. Asai[1]
[1]*Department of Applied Chemistry, Graduate School of Engineering, Tohoku University, Sendai 980-8579, Japan*
[2]*Division of Materials Science, Nara Institute of Science and Technology, Ikoma 630-0192, Japan*

Auger-free luminescence (AFL) is caused by the radiative transition of an valence electron to a core hole state. The transition is competitive with the Auger process, which is a much faster process, efficient AFL cannot be observed in many compounds. In other words, efficient AFL has been observed in limited compounds such as alkaline- or alkaline-earth fluorides or CsCl-based compounds.

AFL has been applied to fast scintillators owing to its fast decay. A representative one is BaF_2; however, CsCl-based compounds have an advantage of long emission wavelength appropriate for detection with a photomultiplier tube. Thus far, we have developed fast scintillators based on ternary CsCl-based compounds [1, 2]. In this study, we developed fast scintillators based on quaternary compounds, $Rb_{1-x}Cs_xCaCl_3$.

The crystals of $Rb_{1-x}Cs_xCaCl_3$ was grown in a simple solidification method after heating the mixed raw powders at 400 K to remove the adsorbed water.

Figure 1 shows the X-ray-induced radioluminescence spectra. A prominent band is observed at approximately 450 nm. The excitation spectra for this band exhibited a peak within the band-gap energy of the crystals. Therefore, the band at 450 nm is attributed to the transition at localized levels within the band-gap. Figure 2 shows the X-ray-induced radioluminescence spectra in the UV region. Several emission bands were observed at 250 and 300–400 nm. We obtained the excitation spectra of these bands in the VUV region to discuss the origin of the emission bands. The excitation spectra exhibited a step-like structure at approximately 84 nm, which corresponds to the energy difference between the outermost core level and the bottom of the conduction band. On the basis of this result, the emission bands are attributed to AFL.

Figure 3 shows the pulse-height spectra of the scintillation detectors equipped with the $Rb_{1-x}Cs_xCaCl_3$ crystals for 662-keV gamma-rays from ^{137}Cs. Note that the coarse gain (CG) of the main amplifier was different for the $Rb_{1-x}Cs_xCaCl_3$ crystals and GSO as a reference. Based on the comparison of the full-energy peak channel, the light yields of $Rb_{1-x}Cs_xCaCl_3$ crystals were estimated to be 520–1200 photons/MeV.

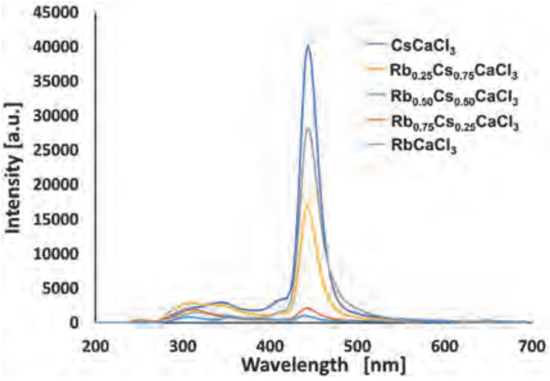

Fig. 1. X-ray-induced radioluminescence spectra of $Rb_{1-x}Cs_xCaCl_3$ crystals.

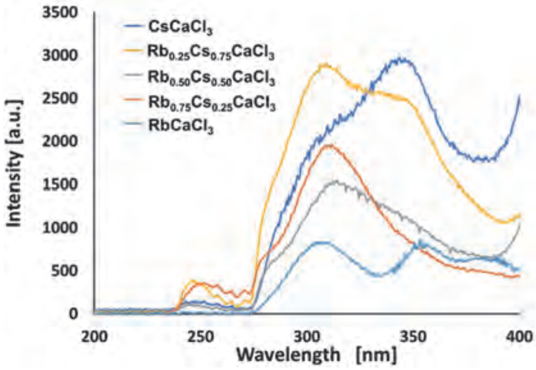

Fig. 2. X-ray-induced radioluminescence spectra of $Rb_{1-x}Cs_xCaCl_3$ crystals in the UV region.

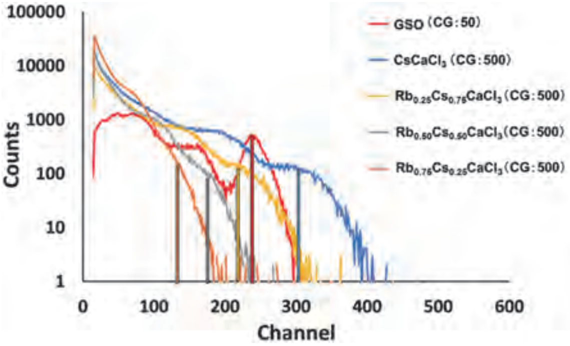

Fig. 3. Pulse-height spectra of the scintillation detectors equipped with the $Rb_{1-x}Cs_xCaCl_3$ crystals for 662-keV gamma-rays from ^{137}Cs.

[1] N. Yahaba, M. Koshimizu, Y. Sun, T. Yanagida, Y. Fujimoto, R. Haruki, F. Nishikido, S. Kishimoto and K. Asai, Appl. Phys. Express **7** (2014) 062602.
[2] M. Koshimizu, N. Yahaba, R. Haruki, F. Nishikido, S. Kishimoto and K. Asai, Opt. Mater. **36** (2014) 1930.

BL7B

Impurity Luminescences of Bulk and Thin Film AlN

W. Kamihigoshi[1], Y. Maegawa[1], K. Fukui [1], K. Yamamoto[2], N. Tatemizo[3] and S. Imada[3]
[1]*Department of Electrical and Electronics Engineering, University of Fukui, Fukui 910-8507, Japan*
[2]*Far-infrared region Development Research Center, University of Fukui, Fukui 910-8507, Japan*
[3]*Faculty of Electrical Engineering and Electronics, Kyoto Institute of Technology, Kyoto 606-8585, Japan*

Since AlN has a wide energy band gap of about 6 eV at room temperature, many unintentionally impurity absorption bands are possible in the bandgap. The information in these bands is important for both electrical and optical applications of AlN. Photoluminescence measurement is useful for the study of impurity bands, as the absorption process of these bands often causes a luminescence process. In this report, we focused on the blue - ultraviolet absorption band that makes AlN yellow and the combined excitation emission spectra (CEES) of both bulk crystal and sputtered AlN(film) were measured.

A 0.5 mm thick *c*-plane AlN bulk crystalline substrate (AlN(bulk)) studied in this report was grown in PVT (physical vapor transport) method by CrystaAl-N GmbH. AlN substrate is transparent with yellow dots and has characteristic impurity absorption band of ~10^{+2} cm^{-1} from 4.2 eV to 5.2 eV region. The *c*-plane AlN thin film (AlN thin film) was deposited by RF (radio frequency) sputtering on SiO2 glass, and shows slightly pale yellow color. Film thickness is about 1 μm and there is an absorption band of ~10^{+4} cm^{-1} at around same energy region [1]. The CEES measurements were carried out at 10 K, in the order of 10^{-6} Pa, and from 2.2 eV to 10.0 eV.

Figure 1 shows the CEES of AlN(bulk) (left) and AlN(film) (right). Each contour plot is normalized at the maximum intensity. Both AlN(bulk) and AlN(film) have similar emission spectra with two peaks at 2.8 eV and around 3.9 eV. However, excitation spectra of the two peaks are different for AlN(bulk) and AlN(film). The CEES of AlN(bulk) is very similar to the results for the AlN(bulk) substrates previously reported by Alden *et al*. [2]. Figure 2 shows the emission spectrum of AlN(bulk) at an excitation energy 4.5 eV. The 3.9 eV emission peak is represented by a single Gaussian fit (UV band), while the 2.8 eV peak is represented by two Gaussian fit (B_H and B_L bands). Figure 3 shows integrated excitation spectra of UV, B_H and B_L bands. The UV band and the B_H bands have the same excitation process which is excited only between 4.2 eV and 5.2 eV, but the excitation process of the B_L band is different and excited up to band gap energy of AlN. On the other hand, both the 2.8 eV and the 3.9 eV peaks of AlN(film) are represented by a single Gaussian fit, and their bandwidth reflecting crystal quality is wider than that of AlN(bulk). Figure 1 suggests that the 2.8 eV peak of AlN(film) is consists only of the B_H band, since the 2.8 eV excitation spectrum is similar to that of the 3.9 eV peak. Figure 1 also suggests both the UV band and the B_H bands are excited above the band gap energy and the excitation spectra of these two bands are similar to the absorption spectrum of AlN. As described above, the absorption coefficient of AlN(film) from 4.2 eV to 5.2 eV is 100 times higher than that of AlN(bulk). This means that in the case of AlN(film), the band-edge tail is able to overlap with this 4.2-5.2 eV absorption band, and the interband transition transfers its energy to both the UV band and the B_H band emissions.

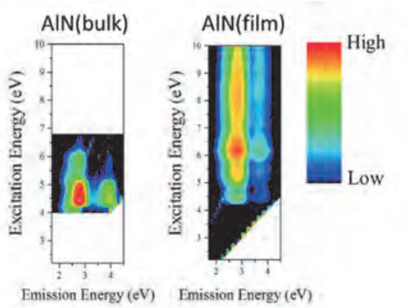

Fig. 1. CEES contour plots of AlN(bulk) and AlN(film).

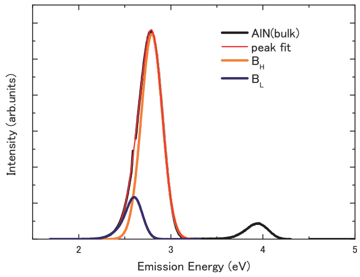

Fig. 2. Emission spectra of AlN(bulk).

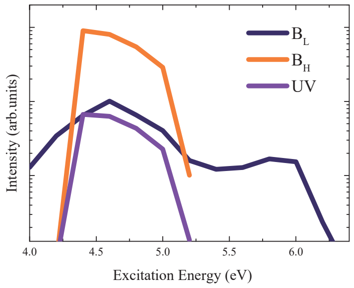

Fig. 3. Excitation spectra of AlN(bulk).

[1] N. Tatemizo *et al*., J. Mater. Chem. A **5** (2017) 20824.
[2] D. Alden *et al.* Phys. Rev. Applied **9** (2018) 054036.

BL7B

Observation of Mott Gap in Pyrochlore Ruthenates $R_2Ru_2O_7$

R. Kaneko[1], M. Masuko[1], R. Yamada[1], J. Fujioka[2], K. Ueda[1] and Y. Tokura[1]
[1]*Department of Applied Physics, University of Tokyo, Tokyo 113-8656, Japan*
[2]*Graduate School of Pure and Applied Sciences, University of Tsukuba, Tsukuba 305-8577, Japan*

The electronic correlation plays a crucial role on their electronic property in transition metal oxides. A typical example is the Mott transition. Coulomb interaction localizes electrons at each atomic site in a Mott insulator. The effective control of the electron correlation, i.e. bandwidth control, gives rise to a number of exotic phenomena in the vicinity of Mott transitions [1].

The pyrochlore ruthenate $R_2Ru_2O_7$ (RRO, R=Pr, Nd, … Lu) is an insulator which undergoes an antiferromagnetic transition at a low temperature, reminiscent of Mott systems. The effective electronic correlation varies as a change of R ionic radius through the modulation of Ru-O bond angles which is related to the electron hopping integral (the larger R gives the smaller U_{eff}). Actually, a specific heat measurement reveals that the Neel temperature T_N, which is roughly proportional to $1/U_{\mathrm{eff}}$ in a simple localized-electron picture, increases with an increase of the ion radius of R^{3+}[2].

What is missing so far is the insight into the electronic band structure. In this experiment, we have aimed to measure optical reflectivity to obtain the optical conductivity which encompasses an important information about the electronic state including the magnitude of the charge gap, interband electronic excitations, and so on.

The optical conductivity can be obtained by Kramers-Kronig (KK) transformation of reflectivity in the whole energy range. Therefore, we measured the reflectivity in a range from 0.01 eV to 5 eV at our laboratory, and from 2 eV to 40 eV at UVSOR. This measurement enables us to discuss the charge dynamics in the energy region of interest. We employed a high-pressure technique for growth of samples which is hard and dense enough to be well polished for the optical measurement.

Figure 1 shows the optical reflectivity for R=Pr, Nd, Sm, and Y compounds. By the KK transformation of the reflectivity, the optical conductivity is obtained as shown in Fig. 2. A charge gap is clearly observed for all samples. We defined the gap size as a value at the crossing point between an energy axis and the extrapolated line from the low-energy slope of each spectrum (dashed lines). The estimated gap size is plotted as a function of the ionic radius of R^{3+} in Fig. 3. The gap size Δ becomes larger as the ionic radius of R^{3+} decreases, which is consistent with the existing theory. It indicates that the electronic states in the 4d electron system, which is characterized by a weak electron correlation and large spin-orbit coupling compared to those in 3d systems, are mainly governed by the electronic correlation.

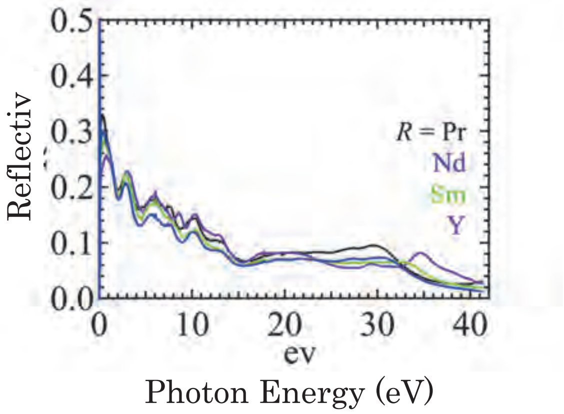

Fig. 1. Optical reflectivity of $R_2Ru_2O_7$ (R=Pr, Nd, Sm, Y) at the room temperature.

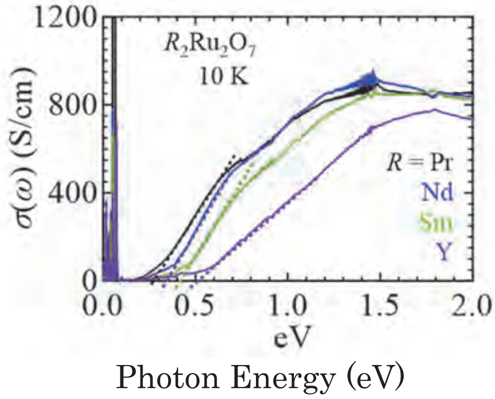

Fig. 2. Optical conductivity of $R_2Ru_2O_7$ (R=Pr, Nd, Sm, Y) at 10 K.

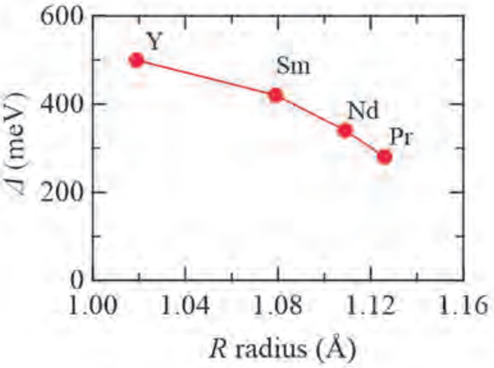

Fig. 3. The magnitude of the charge gap as a function of R ionic radius.

[1] M. Imada, A. Fujimori and Y. Tokura, Rev. Mod. Phys. **70** (1998) 1039.
[2] M. Ito *et al*., J. Phys. Chem. Solids **62** (2001) 337.

BL7B

Evaluation of Electrical Property of CaF$_2$-metal Interface and Development of Vacuum Ultraviolet Detector

S. Kato, J. Otani, K. Suzuki and S. Ono
Nagoya Institute of Technology, Nagoya 466-8555, Japan

Vacuum ultraviolet light sources are applied in various fields such as surface modification of materials and cleaning of semiconductor substrates. For monitoring such a light source, a detector for stably monitoring vacuum ultraviolet light is required. Therefore, we have focused on the fluoride material which is a wide gap material and has high durability against vacuum ultraviolet light irradiation [1-4]. Using such fluoride material made it possible to develop filterless and durable photodetectors. In this study, we aimed to develop a detector capable of operating at zero bias by selectively bringing the fluoride compound CaF$_2$ single crystal into contact with metal.

To fabricate the device, a thin film of Au and Al was deposited on both surfaces of a CaF$_2$ single crystal plate by vacuum deposition method. In order to allow the Au electrode to function as a transparent electrode, the Au electrode was deposited with a thickness allowing vacuum ultraviolet light to pass through (Fig. 1).

In order to investigate a performance of the fabricated device as photodetector, we measured the current value when the device was irradiated with ultraviolet light (photocurrent) and not irradiated (dark current). It was confirmed that the dark current value was about 0.18 pA, the photocurrent value was about 602 pA, and the current value increased more than 3 digits by light irradiation at an applied bias of 100 V. Even at zero bias, the current value increased more than 3 digits by light irradiation. Furthermore, it was confirmed the rectifying property depending on bias direction as shown in Fig. 2.

We measured spectral sensitivity characteristics of the device at zero bias and transmittance of CaF$_2$ single crystal as shown in Fig. 3. It was confirmed that the wavelength response region of the detector is less than 120 nm and coincide with the transmission end of the CaF$_2$ single crystal.

In summary, we achieved filterless VUV detector meeting practical performance by applying CaF$_2$ single crystal and metal interface.

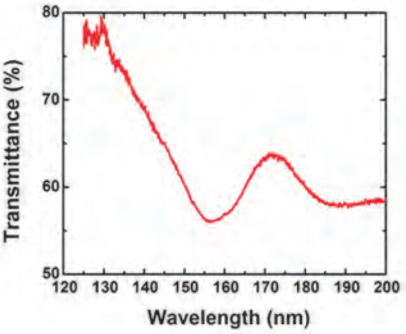

Fig. 1. Transmission spectra of Au electrode.

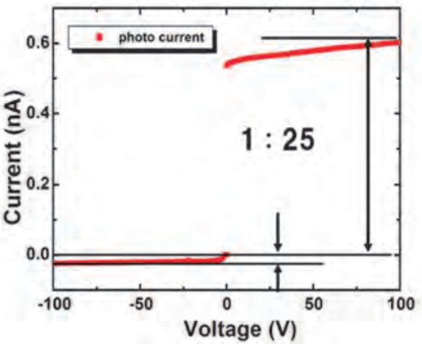

Fig. 2. The rectifying property depending on bias direction.

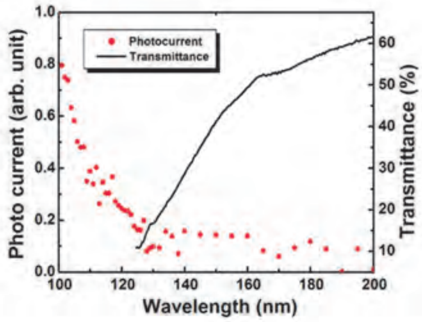

Fig.3. Transmission spectrum and spectral response of the detector.

[1] M. Ieda, T. Ishimaru, S. Ono, N. Kawaguchi, K. Fukuda, T. Suyama, Y. Yokota, T. Yanagida and A. Yoshikawa, Jpn. J. Appl. Phys. **51** (2012) 062202.
[2] T. Ishimaru, M. Ieda, S. Ono, Y. Yokota, T. Yanagida and A. Yoshikawa, Thin Solid Films **534** (2013) 12.
[3] M. Yanagihara, H. Ishikawa, S. Ono and H. Ohtake, Testing and Measurement: Techniques and Applications (2015) 151.
[4] K. Suzuki, M. C. Raduban, M. Kase and S. Ono, Optical Materials **88** (2019) 576.

BL7B

Optical Study of FeSe Thin Films on $LaAlO_3$ Substrate

M. Nakajima[1], K. Yanase[1], M. Kawai[2], T. Ishikawa[2], N. Shikama[2], F. Nabeshima[2],
A. Maeda[2] and S. Tajima[1]
[1]*Department of Physics, Osaka University, Osaka 560-0043, Japan*
[2]*Department of Basic Science, University of Tokyo, Tokyo 153-8902, Japan*

In iron-based superconductors, the electronic structure is strongly affected by in-plane strain. In particular, the band structure of FeSe thin films differs from that of bulk FeSe due to the epitaxial strain [1]. The correlation between a superconducting transition temperature (T_c) and the magnitude of strain indicates that the band-structure modification definitely altered physical properties [2], but how the electronic state changes with application of strain is still unclear. In this study, we performed optical spectroscopy on thin films of FeSe on $LaAlO_3$ substrates with a tensile strain and investigated the effect of in-plane strain.

Thin films of FeSe with the thickness of 150 nm were fabricated on $LaAlO_3$ by the pulsed-laser deposition method [2]. Optical reflectivity measurement was carried out on the FeSe film and the bare $LaAlO_3$ substrate for the energy range of 0.05–2 eV using the Fourier-transform infrared spectrometer (Bruker Vertex 80v). High-energy reflectivity measurement of $LaAlO_3$ for 2–40 eV at room temperature was performed at BL7B of the UVSOR synchrotron facility. Dielectric function of $LaAlO_3$ was derived via the Kramers-Kronig transformation, and the thin-film reflectivity spectrum was fitted using a number of Lorentz oscillators, which gives the dielectric function of FeSe [3].

Figure 1(a) shows the reflectivity spectrum of $LaAlO_3$ for a wide range of energy up to 40 eV. Three optical phonon modes dominate the low-energy region below 0.1 eV, whereas several peaks associated with interband transitions are present in the high-energy region above 6eV. In Fig. 1(b), we plot the dielectric function of $LaAlO_3$ derived from the reflectivity data. The phonon modes are observed at 22.6, 53.0, and 80.8 meV.

The reflectivity spectrum of the FeSe film on $LaAlO_3$ at room temperature is shown in Fig. 2(a). Due to multiple reflections within the film, the phonon modes of substrate $LaAlO_3$ makes an impact on the reflectivity spectrum, giving rise to three peaks at corresponding energies. Using the dielectric function of $LaAlO_3$, we can remove the substrate contribution and extract the optical conductivity spectrum of FeSe. The result is shown in Fig. 2(b). The peak at 29.6 meV corresponds to an optical phonon mode of FeSe. Compared with the spectrum of FeSe with a compressive strain [3], the low-energy spectral weight is smaller in the present case. The smaller carrier density is likely related to the suppression of T_c.

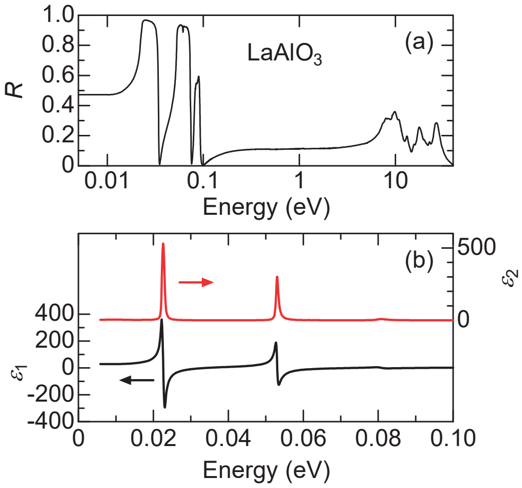

Fig. 1. (a) Reflectivity spectrum of $LaAlO_3$ at room temperature up to 40 eV. (b) Real and imaginary parts of dielectric function of $LaAlO_3$ below 0.1 eV.

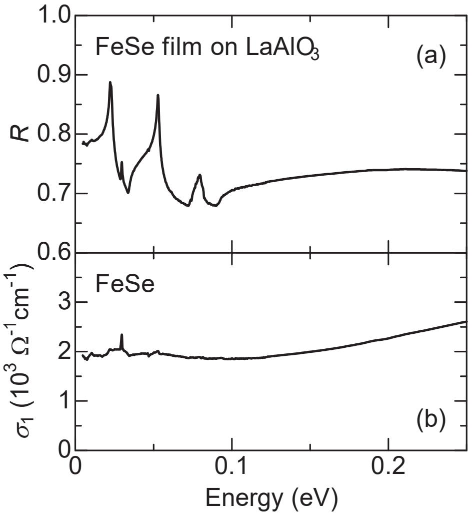

Fig. 2. (a) Reflectivity spectrum of the FeSe thin film on the $LaAlO_3$ substrate at room temperature. (b) Optical conductivity spectrum of FeSe.

[1] G. N. Phan *et al.*, Phys. Rev. B **95** (2017) 224507.
[2] F. Nabeshima *et al.*, Jpn. J. Appl. Phys. **57** (2018) 120314.
[3] M. Nakajima *et al.*, Phys. Rev. B **95** (2017) 184502.

BL7B

Optical Investigations of Pr/Ce-doped APLF Glasses as Potential Neutron Scintillators

T. Shimizu, Y. Minami, M. J. F. Empizo, K. Kawano, K. Kuroda, K. Yamanoi,
N. Sarukura and T. Murata
Institute of Laser Engineering, Osaka University, Suita 565-0871, Japan

Recently, neutron detection is required in inertial confinement fusion research and infrastructure inspection. The ratio of primary neutron and scattered neutron corresponds to the density and radius parameter of fusion plasma. Additionally, neutron detection is considered as one of the nondestructive methods for inspecting the form of infrastructure. Scintillator materials which are able to detect and discriminate neutrons should then be developed to be able to satisfy the technological demand.

Previously, the optical properties of praseodymium (Pr^{3+})-doped and cerium (Ce^{3+})-doped APLF [20Al(PO3)3-80LiF] glasses was studied as fast response scintillators for neutron detection [1]. The optical properties were characterized using photoluminescence and photoluminescence excitation of the Pr^{3+}- and Ce^{3+}-doped APLF glass samples for doping concentrations ranging from 0.1 to 3.0 mol%. The APLF glass doped with Pr^{3+} revealed rich emission bands under 180, 217, and 430-440 nm excitations. The broad emission from 228 to 371 nm for both excitations were assigned to the interconfigurational 4f5d and intraconfigurational 4f transitions of Pr^{3+} ions. The intensity of the emission peaks was observed to increase as a result of increasing Pr^{3+} concentration. In contrast, the APLF glass doped with Ce^{3+} exhibited intense emission at 340 nm under 240 to 400 nm excitation which originated from the 4f5d transition of Ce^{3+} ions. There was no fluorescence from 4f transitions, but the strong emission peak at 340 nm was shifted to shorter wavelengths with decreasing Ce^{3+} concentration. The decay times of APLF80+Pr^{3+} under 217 nm excitation were constant at different temperatures from 0 K to 300 K and became faster with increased doping concentration from 19 ns (0.5% Pr^{3+}) to 16 ns (3.0% Pr^{3+}). The decay times of APLF80+Ce^{3+} glasses were the same in the range from 38 to 41 ns with neutron excitation from a 252Cf source regardless of Ce concentration. These results highlight that the scintillation decay times from both Pr^{3+}- and Ce^{3+}-doped APLF glasses are significantly faster than conventional glass scintillators and therefore an advantage for fast-response scintillator applications. Investigation is underway to improve the scintillation decay times and conversion efficiencies by co-doping APLF glass with Pr^{3+} and Ce^{3+}.

Now, we have developed co-dope APLF glass with Pr and Ce for improvement of decay times and conversion efficiencies. In this study, we investigated the optical properties of Pr/Ce-doped APLF glasses with different concentrations using the spectroscopy beamline (BL7B) of the Institute of Molecular Science UVSOR Synchrotron Facility. Figure 2 shows the PL spectra of the Pr/Ce-doped APLF glasses. This results are presently under analysis.

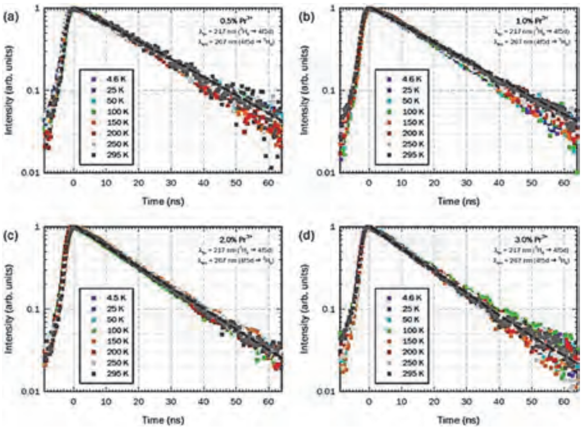

Fig. 1. Decay profiles of the (4f5d → 3H6) emissions of (a) , (b) , (c) , and (d) Pr^{3+}-doped APLF glasses at different temperatures under excitation into the 4f5d level [1]

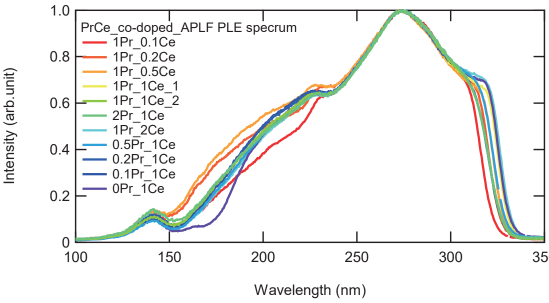

Fig. 2. PLE spectrum of Pr^{3+} and Ce^{3+} co-doped APLF glass by using UVSOR.

[1] M. J. F.Empizo *et al*., J. Lumin. **193** (2018) 13.

UVSOR User 3